

NAVAL POSTGRADUATE SCHOOL  
Monterey, California



DISSERTATION

INCORPORATION OF SWEEP IN A  
TRANSONIC FAN DESIGN USING A 3D  
BLADE-ROW GEOMETRY PACKAGE  
INTENDED FOR  
AERO-STRUCTURAL-MANUFACTURING  
OPTIMIZATION

by

Hazem Fahmy Abdelhamid

September 1997

Advisor:

Raymond P. Shreeve

Thesis  
A16325

Approved for public release; Distribution is unlimited.

DUDLEY KNOX LIBRARY  
NAVAL POSTGRADUATE SCHOOL  
MONTEREY CA 93943-5101

REPORT DOCUMENTATION PAGE			Form Approved OMB No. 0704-0188	
Public reporting burden for this collection of information is estimated to average 1 hour per response, including the time for reviewing instruction, searching existing data sources, gathering and maintaining the data needed, and completing and reviewing the collection of information. Send comments regarding this burden estimate or any other aspect of this collection of information, including suggestions for reducing this burden, to Washington Headquarters Services, Directorate for Information Operations and Reports, 1215 Jefferson Davis Highway, Suite 1204, Arlington, Va 22202-4302, and to the Office of Management and Budget, Paperwork Reduction Project (0704-0188) Washington DC 20503.				
1. AGENCY USE ONLY (Leave blank)		2. REPORT DATE September, 1997		3. REPORT TYPE AND DATES COVERED Ph.D. Thesis
4. TITLE AND SUBTITLE INCORPORATION OF SWEEP IN A TRANSONIC FAN DESIGN USING A 3D BLADE-ROW GEOMETRY PACKAGE INTENDED FOR AERO-STRUCTURAL-MANUFACTURING OPTIMIZATION			5. FUNDING NUMBERS	
6. AUTHORS Abdelhamid, Hazem				
7. PERFORMING ORGANIZATION NAME(S) AND ADDRESS(ES) Naval Postgraduate School Monterey CA 93943-5000			8. PERFORMING ORGANIZATION REPORT NUMBER	
9. SPONSORING/MONITORING AGENCY NAME(S) AND ADDRESS(ES)			10. SPONSORING/MONITORING AGENCY REPORT NUMBER	
11. SUPPLEMENTARY NOTES The views expressed in this thesis are those of the author and do not reflect the official policy or position of the Department of Defense or the U.S. Government.				
12a. DISTRIBUTION/AVAILABILITY STATEMENT Approved for public release; distribution is unlimited.			12b. DISTRIBUTION CODE	
13. ABSTRACT(maximum 200 words)  A new 3D blade row geometry package was developed and implemented. In the new representation the blade is described by six Bezier surfaces two of which represent the pressure and suction surfaces with sixteen points each. The leading and trailing edges are each represented by two Bezier surfaces. Only one extra parameter is required (in addition to the pressure and suction surfaces parameters) to define each of the leading and trailing edge surfaces. Blade geometry manipulation in this format is easily implemented. A change to one surface location affects the surrounding area inversely proportional to the distance from the moved point, creating a smooth variation in geometry, free of waviness. The geometry generated is easy to handle with CAD/CAM programs without any conversion or approximation. The representation was applied to an existing transonic fan geometry to investigate effects of sweep. Results were obtained for the effect of forward and backward sweep on the aerodynamic performance, and the associated effect on centrifugal stress levels was obtained. The investigation demonstrated the suitability of the package to be incorporated into a multi-disciplinary design optimization process.				
14. SUBJECT TERMS Transonic Fan Design, Fan Blade Geometry, Bezier Surfaces			15. NUMBER OF PAGES 131	
			16. PRICE CODE	
17. SECURITY CLASSIFICATION OF REPORT Unclassified	18. SECURITY CLASSIFICATION OF THIS PAGE Unclassified	19. SECURITY CLASSIFICATION OF ABSTRACT Unclassified	20. LIMITATION OF ABSTRACT UL	



**Approved for public release; distribution is unlimited**

**INCORPORATION OF SWEEP IN A TRANSONIC FAN DESIGN USING A 3D  
BLADE-ROW GEOMETRY PACKAGE INTENDED FOR AERO-STRUCTURAL-  
MANUFACTURING OPTIMIZATION**

Hazem Fahmy Abdelhamid  
Major, Egyptian Air Force  
B.S., Military Technical College, Egypt, 1985  
M.S., Military Technical College, Egypt, 1991

Submitted in partial fulfillment of the  
requirements for the degree of

**DOCTOR OF PHILOSOPHY IN AERONAUTICAL ENGINEERING**

from the

**NAVAL POSTGRADUATE SCHOOL  
September 1997**

1997.09

1997.09

ABDELHAMID, H.

10313  
A/6325

E.2

## ABSTRACT

A new 3D blade row geometry package was developed and implemented. In the new representation the blade is described by six Bezier surfaces two of which represent the pressure and suction surfaces with sixteen points each. The leading and trailing edges are each represented by two Bezier surfaces. Only one extra parameter is required (in addition to the pressure and suction surfaces parameters) to define each of the leading and trailing edge surfaces. Blade geometry manipulation in this format is easily implemented. A change to one surface location affects the surrounding area inversely proportional to the distance from the moved point, creating a smooth variation in geometry, free of waviness. The geometry generated is easy to handle with CAD/CAM programs without any conversion or approximation. The representation was applied to an existing transonic fan geometry to investigate effects of sweep. Results were obtained for the effect of forward and backward sweep on the aerodynamic performance, and the associated effect on centrifugal stress levels was obtained. The investigation demonstrated the suitability of the package to be incorporated into a multi-disciplinary design optimization process.





# TABLE OF CONTENTS

I.	INTRODUCTION . . . . .	1
II.	PROBLEM REVIEW . . . . .	3
A.	DESIGN METHODS . . . . .	4
1.	Quasi Three Dimensional Method . . . . .	4
2.	Three Dimensional Method . . . . .	6
B.	SWEEP ATTEMPTS . . . . .	8
1.	NASA QF-12 . . . . .	10
2.	Neubert et al. . . . .	10
3.	Puterbaugh et al. . . . .	12
4.	Wadia et al. . . . .	12
C.	LIMITATION IN CURRENT DESIGN SYSTEM . . . . .	13
D.	WHAT NEEDS TO BE DONE . . . . .	14
III.	GEOMETRY REPRESENTATION . . . . .	17
A.	CHOICE OF GEOMETRY REPRESENTATION . . . . .	17
1.	Different Geometrical Representations . . . . .	17
2.	Advantages and Disadvantages . . . . .	20
3.	Selected Representation . . . . .	20
B.	BEZIER CURVES . . . . .	20
1.	Mathematical Representation . . . . .	20
2.	Cross Plots . . . . .	22
3.	Effect of Moving Control Points . . . . .	22
4.	Properties of Bezier Curves . . . . .	23
5.	Differentiation . . . . .	25
6.	Continuity Between Curves . . . . .	25
7.	Difference Between <i>C&amp;G</i> . . . . .	25
8.	Subdivision . . . . .	26

C.	BEZIER SURFACES . . . . .	28
1.	Mathematical Representation . . . . .	28
2.	Effect of Moving Control Points . . . . .	29
3.	Continuity Between Surfaces . . . . .	29
D.	PARAMETERIZATION . . . . .	29
IV.	INITIAL GEOMETRY PACKAGE . . . . .	33
A.	APPROXIMATING BLADE GEOMETRY . . . . .	34
B.	ADDING LEADING AND TRAILING EDGE SURFACES . . .	37
C.	EXAMPLES OF GEOMETRY MANIPULATION . . . . .	38
1.	General (Point) Manipulation . . . . .	38
2.	Programmed (Shape) Manipulation . . . . .	39
D.	PROGRAM LANGUAGE AND STRUCTURE . . . . .	41
1.	'point' . . . . .	43
2.	'vector' . . . . .	44
3.	'matrix' . . . . .	45
4.	'surface' . . . . .	45
5.	'bsurface' . . . . .	45
6.	'blade' . . . . .	46
V.	APPLICATION TO THE INCORPORATION OF SWEEP . .	47
A.	SOFTWARE TOOLS . . . . .	47
1.	TCGRID . . . . .	47
2.	RVC3D . . . . .	48
3.	FAST . . . . .	48
4.	IDEAS . . . . .	48
B.	REFERENCE AND SWEPT GEOMETRIES . . . . .	49
C.	RESULTS OF FLOW ANALYSIS . . . . .	57
1.	Overall Performance . . . . .	57
2.	Exit Flow Field (Peripherally-Averaged) . . . . .	57

3.	Blade Passage Flow Field . . . . .	65
D.	RESULTS OF STRESS ANALYSIS . . . . .	82
VI.	DISCUSSION . . . . .	87
VII.	CONCLUSIONS AND RECOMMENDATIONS . . . . .	89
A.	CONCLUSIONS . . . . .	89
B.	RECOMMENDATIONS . . . . .	89
APPENDIX A. SANGER ROTOR GEOMETRY IN MERIDL3 FOR-		
	MAT . . . . .	91
APPENDIX B. GENERATING IGES FILES . . . . .		97
1.	IGES FILE STRUCTURE . . . . .	97
a.	Start Section . . . . .	97
b.	Global Section . . . . .	97
c.	Directory Section . . . . .	97
d.	Parameter Data Section . . . . .	98
e.	Terminate Section . . . . .	98
2.	GEOMETRY IN IGES FORMAT . . . . .	98
APPENDIX C. RESULTS OF FLOW ANALYSIS WITH DIFFER-		
	ENT GRIDS . . . . .	99
LIST OF REFERENCES . . . . .		107
INITIAL DISTRIBUTION LIST . . . . .		109



# LIST OF FIGURES

1.	Intersecting $S_1S_2$ Surfaces in a Blade Row . . . . .	5
2.	Streamline Curvature Computing Stations and Stream Surface . . . . .	7
3.	Passage Shock-Wave Configuration for Estimating Shock-Loss Levels .	9
4.	Flow at Inlet of Cascade of Airfoils Operated with Supersonic Relative Inlet Mach Number . . . . .	9
5.	Three Dimensional Shock Surface Between Two Blades . . . . .	10
6.	Swept Fan Design Procedure. . . . .	11
7.	Hermite Representation . . . . .	18
8.	Bezier Curve Representation . . . . .	19
9.	B-Spline Representation . . . . .	19
10.	Cross Plot . . . . .	23
11.	Control Point Movement Along The Tangent Direction . . . . .	24
12.	Convex Hull Property . . . . .	24
13.	Two Bezier Curves with First-Derivative Continuity . . . . .	26
14.	Condition for Second-Derivative Continuity for Bezier Curves . . . . .	26
15.	Bezier Curve Subdivision . . . . .	27
16.	Bezier Surface with its Control Net . . . . .	28
17.	Effect of Surface Control Point Movement . . . . .	29
18.	Tangency Condition for Surfaces . . . . .	30
19.	Error Vector $D_i$ for Parametrized Data . . . . .	31
20.	Blade Surface Numbering . . . . .	34
21.	Control Point Numbering . . . . .	35
22.	Double Circular Arc Blade Section [Bezier Approximation] . . . . .	37
23.	Transonic Fan Blade Section [Bezier Approximation] . . . . .	37
24.	The Effect of Moving Control Point 11 in the Tangential Direction .05 Radians . . . . .	39

25.	Blade Lean Created by Moving the Top Row of Control Points (0.05 Radians in Each Direction). . . . .	40
26.	Blade Lean Created by Moving the Top Two Rows of Control Points (0.05 Radians in Each Direction). . . . .	41
27.	Forward and Aft Sweep (10% of Chord) Using Sweep_1. . . . .	42
28.	Forward and Aft Sweep (10% of Chord Using Sweep_2. . . . .	43
29.	Sweep with Both Forward and Aft-Sweep of 10% of Chord . . . . .	44
30.	Grid for Sanger Blade Row . . . . .	52
31.	Grid for Fitted (Base) Blade Row . . . . .	52
32.	Grid for Data Set 1. . . . .	54
33.	Grid for Date Set 2. . . . .	54
34.	Swept Forward +10% Using Sweep_1 . . . . .	55
35.	Swept Back -10% Using Sweep_1 . . . . .	55
36.	Swept Forward +10% Using Sweep_2 . . . . .	56
37.	Swept Back -10% Using Sweep_2 . . . . .	56
38.	Grid for Data Set 3. . . . .	58
39.	Convergence History for Data Set 3. . . . .	58
40.	Radial Distribution of the Circumferentially Energy-Averaged Efficiency. . . . .	60
41.	Radial Distribution of the Circumferentially Energy-Averaged Total-to-Reference Pressure. . . . .	60
42.	Radial Distribution of the Circumferentially Energy-Averaged Static-to-Reference Pressure. . . . .	61
43.	Radial Distribution of the Circumferentially Energy-Averaged Total-to-Reference Temperature. . . . .	61
44.	Radial Distribution of the Circumferentially Energy-Averaged Static-to-Reference Temperature. . . . .	62
45.	Radial Distribution of the Mach Number. . . . .	62
46.	Radial Distribution of the Flow Angle ( $\phi$ ) in the Meridional Plane. . . . .	63



47.	Radial Distribution of the Total Velocity to Reference Sonic Velocity. . . . .	63
48.	Radial Distribution of the Swirl Angle ( $\alpha$ ). . . . .	64
49.	Mach Number in the Blade Passage of the Sanger Rotor at 10% Span. . . . .	66
50.	Mach Number in the Blade Passage of the Sanger Rotor at 25% Span. . . . .	66
51.	Mach Number in the Blade Passage of the Sanger Rotor at 50% Span. . . . .	67
52.	Mach Number in the Blade Passage of the Sanger Rotor at 75% Span. . . . .	67
53.	Mach Number in the Blade Passage of the Sanger Rotor at 90% Span. . . . .	68
54.	Mach Number in the Blade Passage of the Sanger Rotor in the Case Wall Boundary Layer. . . . .	68
55.	Mach Number in the Blade Passage of the Sanger Rotor (Lower Blade) and Base Rotor (Upper Blade) at 10% Span. . . . .	69
56.	Mach Number in the Blade Passage of the Sanger Rotor (Lower Blade) and Base Rotor (Upper Blade) at 25% Span. . . . .	69
57.	Mach Number in the Blade Passage of the Sanger Rotor (Lower Blade) and Base Rotor (Upper Blade) at 50% Span. . . . .	70
58.	Mach Number in the Blade Passage of the Sanger Rotor (Lower Blade) and Base Rotor (Upper Blade) at 75% Span. . . . .	70
59.	Mach Number in the Blade Passage of the Sanger Rotor (Lower Blade) and Base Rotor (Upper Blade) at 90% Span. . . . .	71
60.	Mach Number in the Blade Passage of the Sanger Rotor (Lower Blade) and Base Rotor (Upper Blade) in the Case Wall Boundary Layer. . . . .	71
61.	Mach Number in the Blade Passage of the Base Rotor (Lower Blade) and Swept-Forward Rotor (Upper Blade) at 10% Span. . . . .	73
62.	Mach Number in the Blade Passage of the Base Rotor (Lower Blade) and Swept-Forward Rotor (Upper Blade) at 25% Span. . . . .	73
63.	Mach Number in the Blade Passage of the Base Rotor (Lower Blade) and Swept-Forward Rotor (Upper Blade) at 50% Span. . . . .	74

64.	Mach Number in the Blade Passage of the Base Rotor (Lower Blade) and Swept-Forward Rotor (Upper Blade) at 75% Span. . . . .	74
65.	Mach Number in the Blade Passage of the Base Rotor (Lower Blade) and Swept-Forward Rotor (Upper Blade) at 90% Span. . . . .	75
66.	Mach Number in the Blade Passage of the Base Rotor (Lower Blade) and Swept-Forward Rotor (Upper Blade) in the Case Wall Boundary Layer. . . . .	75
67.	Mach Number in the Blade Passage of the Base Rotor (Lower Blade) and Swept-Back Rotor (Upper Blade) at 10% Span. . . . .	76
68.	Mach Number in the Blade Passage of the Base Rotor (Lower Blade) and Swept-Back Rotor (Upper Blade) at 25% Span. . . . .	76
69.	Mach Number in the Blade Passage of the Base Rotor (Lower Blade) and Swept-Back Rotor (Upper Blade) at 50% Span. . . . .	77
70.	Mach Number in the Blade Passage of the Base Rotor (Lower Blade) and Swept-Back Rotor (Upper Blade) at 75% Span. . . . .	77
71.	Mach Number in the Blade Passage of the Base Rotor (Lower Blade) and Swept-Back Rotor (Upper Blade) at 90% Span. . . . .	78
72.	Mach Number in the Blade Passage of the Base Rotor (Lower Blade) and Swept-Back Rotor (Upper Blade) in the Case Wall Boundary Layer. . . . .	78
73.	Pressure on the Suction Surface of the Swept-Back Rotor Blade. . . . .	79
74.	Velocity Vector Near Suction Surface ( $3^{rd}$ Grid Point) of the Swept- Back Rotor Blade. . . . .	79
75.	Pressure on the Suction Surface of the Base Rotor Blade. . . . .	80
76.	Velocity Vector Near Suction Surface ( $3^{rd}$ Grid Point) of the Base Rotor Blade. . . . .	80
77.	Pressure on the Suction Surface of the Swept-Forward Rotor Blade. . . . .	81
78.	Velocity Vector Near Suction Surface ( $3^{rd}$ Grid Point) of the Swept- Forward Blade. . . . .	81



79.	Stress Levels for the Base Rotor. . . . .	83
80.	Stress Levels for the Swept-Backward Rotor. . . . .	84
81.	Stress Levels for the Swept-Forward Rotor. . . . .	85
82.	Radial Distribution of the Circumferentially Energy-Averaged Efficiency. . . . .	99
83.	Radial Distribution of the Circumferentially Energy-Averaged Total-to-Reference Pressure. . . . .	100
84.	Radial Distribution of the Circumferentially Energy-Averaged Static-to-Reference Pressure. . . . .	100
85.	Radial Distribution of the Circumferentially Energy-Averaged Total-to-Reference Temperature. . . . .	101
86.	Radial Distribution of the Circumferentially Energy-Averaged Static-to-Reference Temperature. . . . .	101
87.	Radial Distribution of the Mach Number. . . . .	102
88.	Radial Distribution of the Flow Angle ( $\phi$ ) in the Meridional Plane. . . . .	102
89.	Radial Distribution of the Total Velocity to Reference Sonic Velocity. . . . .	103
90.	Radial Distribution of the Swirl Angle ( $\alpha$ ). . . . .	103
91.	Mach Number in the Blade Passage of the Sanger Rotor (Lower Blade) and Base Rotor (Upper Blade) at 10% Span. . . . .	104
92.	Mach Number in the Blade Passage of the Sanger Rotor (Lower Blade) and Base Rotor (Upper Blade) at 50% Span. . . . .	104
93.	Mach Number in the Blade Passage of the Sanger Rotor (Lower Blade) and Base Rotor (Upper Blade) at 75% Span. . . . .	105
94.	Mach Number in the Blade Passage of the Sanger Rotor (Lower Blade) and Base Rotor (Upper Blade) in the Case Wall Boundary Layer. . . . .	106



# LIST OF TABLES

I.	Comparison of Properties of Different Forms of Parametric Cubic Curves.	21
II.	Different Parameterization (t = parameter, e = error; subscripts a,s,c are arclength, square root and cubic root). . . . .	36
III.	Rotor Design Parameters. . . . .	49
IV.	Bezier Representation of Sanger Rotor [Base Geometry]. . . . .	51
V.	Overall Performance Results. . . . .	59



# ACKNOWLEDGMENTS

All thanks and gratitude to ALLAH the most generous and merciful, to whom I owe every thing in my life. Everything he gave me was perfect, from a very understanding supervisor who knew when and how to help and when to encourage me when it was needed the most, to a supportive committee that helped to the last minute even when they were not required to. Everything was great as were all those whom I dealt with in the Aero department, the Scientific Visualization Lab and NPS. Everyone was very supportive and always took an extra step to bring me back on track. My parents have a great role in where I am now; they have never spared any effort to make sure that I have the best education and skills possible. My sister and brother were also very helpful and encouraging; they have always had faith in me and that pushed me even further to not fail them. Adding to all that my wife MAHA who had to take care of our two sons and me and to make sure that I have the best environment for success at the time she needed me the most. She had to do all that in a society that she is unfamiliar with and away from all those she used to be with without any anticipation of recognition. Also, I was lucky to have the best friends one can ever have. All those had set the stage for me to get to where I am with the least effort. For all that which was given to me, thank you. It could not have been better.



# I. INTRODUCTION

One of the most challenging components to design in an aircraft engine is the fan, or the compressor. The compression system has to supply the engine with the required mass flow rate, pressure ratio and stall margin with the least possible losses, weight and frontal area.

To satisfy the compressor design requirements, engineers have developed complex design systems and analysis tools. However, with the conventional design methods being pushed to the limit, researchers have started to investigate new concepts that were not easy to investigate in the absence of the current computational tools several years ago.

One of the concepts receiving considerable attention currently is sweep. It was introduced into transonic fan design to reduce the shock loss. Several early sweep attempts were reported, which had little success. More recent attempts have shown promise. However, the problem is not fully understood, and a clear isolation of sweep effects is not yet available.

Viewing sweep as a promising concept, an attempt was made here to investigate the incorporation of sweep into the design process. The current design system was reviewed first to determine the best way to approach the problem. From that review it was concluded that the current design system is not suitable for the problem at hand specifically in the way that the geometry is handled. The geometry used in current design systems is a 2D representation of blade sections that can be moved circumferentially or axially in the structural design phase. This would be unacceptable when designing with sweep. Moving the blade sections circumferentially after deciding on a sweep schedule will alter the flow significantly. The transonic flow through a blade row with sweep is essentially three dimensional. This led to the conclusion that a 3D blade geometry representation is badly needed if a rational 3D blade design procedure is to be developed successfully.

Bezier surface representation was found to be suitable for blade representation. Having few control parameters and offering flexible manipulation, it was viewed as a good choice for 3D blade geometry representation, one that might lead to 3D blade design optimization. The other significant advantage of the Bezier representation, besides being compact, is that it is read easily by CAD/CAM programs with no approximation.

The representation was packaged in a form suitable for turbomachinery blading and compatible with the existing design system. A test case was applied to prove the concept and determine the suitability of the package to the design problem. The representation was found to be very flexible and capable of rational geometry manipulation. It was also found that the blade design parameters used currently can be represented in terms of the Bezier parameters.

The effect of sweep on blade row performance was investigated. The sweep was implemented in a manner that kept the blade parameters unchanged (maximum thickness, maximum thickness location, section profile, etc.). This was in contrast to previously reported sweep attempts that had to accept other changes to the design to meet steady and unsteady stress constraints. The geometry represented by the Bezier format was imported into IDEAS with no approximation, and a purely centrifugal stress analysis was conducted.

The results of the test cases were that the swept-back rotor efficiency was better than the swept-forward, and the rotor pumped higher mass flow rate at the same speed and pressure ratio. The effects of sweep were qualitatively similar when changes were made to the leading edge within the grid generation software..

The geometry package still needs further development and the tools supporting it also need to be developed to be compatible (grid generation in particular). The obtained results are viewed as a proof of concept and not as a definitive study of the effects of sweep.



## II. PROBLEM REVIEW

Aircraft compressor design is a very complicated process; one that involves aerodynamic, structural, manufacturing and maintenance disciplines. Each of these introduces very tight constraints that limit the design space. In addition, the tools that are used in each discipline dictate what information is needed from the others. The ease of interfacing and data sharing is very critical. Usually, to go from one engineering or manufacturing group to another, a conversion and approximation process takes place.

The aerodynamic design is necessarily limited to what analytical tools are available. Typically, the designer arrives at a geometry using analytical methods based on simplified models. He then verifies that geometry by analysis using available computational tools. Design methods over the past decades have evolved from the use of very simple one-dimensional mean line models, to the incorporation of "simple radial equilibrium", to quasi-three dimensional (Q3D) methods for arbitrary flow paths. The quasi three-dimensional methods became practical when methods such as stream line-curvature for calculating the axi-symmetric through flow became available.

Similarly, the computational analysis tools have evolved from two-dimensional potential plus integral boundary layer, to three-dimensional Euler plus differential boundary layer, to fully three-dimensional Navier-Stokes methods. The proven capability of computational fluid dynamics (CFD) to reproduce complex three dimensional flow fields has recently led to the use of expressions such as "CFD design methods" and, even more recently, to the idea of trying to rationally optimize blade design to include "sweep" and "lean" as well as profile shape. In order to put the present work in perspective, a review is given of the classical Q3D and recent CFD design methods, and of published attempts to introduce sweep.

## A. DESIGN METHODS

### 1. Quasi Three Dimensional Method

In 1952, Wu [Ref. 1] developed a general theory of three-dimensional flow in subsonic and supersonic turbomachines. It was for steady nonviscous rotational and irrotational flows. There was no limitation on whether the machine should be axial, radial or even of mixed flow type. The solutions of the direct and inverse problems were possible through the definition of a specific combination of relative stream surfaces. Referring to Wu's illustration shown in Fig. 1, solving for the two-dimensional flow on two stream surfaces identified as S1 and S2 equivalently solves the three-dimensional problem. S1 represents the 'tangential-axial' stream surface while S2 represents the 'radial-axial' plane. In general, these surfaces can be of arbitrary shape to satisfy the equation of motion. The flow channel can have as many S1 and S2 surfaces as the problem may require. An iterative procedure is used between the two surfaces to solve for the flow field. The solution on each surface updates the flow on the other surface.

Since it was introduced by Wu, the S1 and S2 method has been applied in different ways. Simplifications were introduced which varied from one method to another. Most of the methods used one S2 surface and several S1 surfaces. The most widely used simplification is the assumption that the S1 plane is axisymmetric. The assumption of linearly varying streamtube thickness and radial position allowed the omission of in-blade computing stations. On the other hand, an extension to the theory to handle rotational transonic flow has been reported [Ref. 2]. The use of a number of S1 and S2 surfaces was also reported [Ref. 3].

The quasi-3D design approach [Ref. 4, 5, 6] is based on the S1 and S2 formulation, using the assumption of axisymmetric S1 surfaces and axisymmetric conditions between blade rows. First, given a mass flow rate, rotational speed and work, the annulus height and mean-line flow angles are determined using a one-dimensional mean-line method. Then a through-flow analysis is used to determine the span-wise

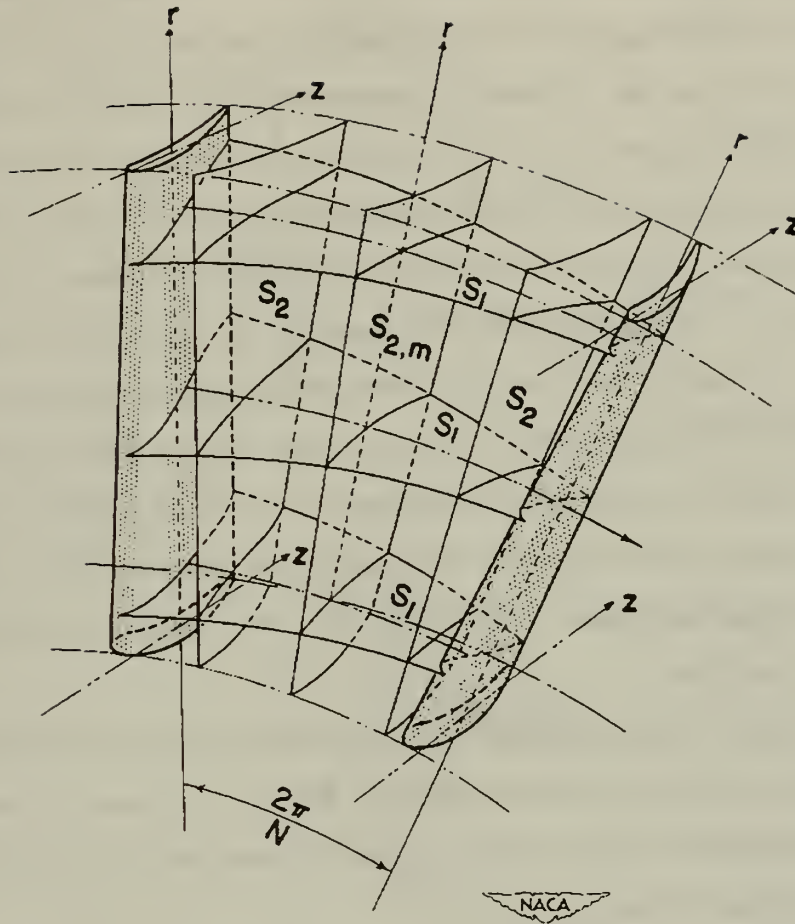


Figure 1. Intersecting  $S_1 S_2$  Surfaces in a Blade Row [Ref. 1]

variation of inlet and exit flow angles to the blading and the streamtube thickness variation. The blade section geometry, which is defined on the axisymmetric stream surfaces, is produced using blade-to-blade inverse or direct methods, or using empirical correlations. The design system is not fully analytic; it has to be complimented with experience and empiricism. The selection of loss coefficients, incidence angles and diffusion factors is normally based on correlations derived from experimental results. Such data are updated when test results for newly designed blading are available. Most design data are proprietary and not available in the open literature.

In 1985, Jennions [Ref. 6] presented a Q3D blade design method that relied

on a Rolls-Royce database. The system consists of a through-flow program, a blade-to-blade program and a stacking-line program. Illustrated in Fig 2, the through-flow program is based on the streamline curvature method. The flow channel is divided into computing stations from inlet to outlet including the blade region. The radial equilibrium equation is solved on each station to refine the streamline path. The radial pressure gradient calculated from radial equilibrium is affected by the streamline curvature in the meridional plane, centrifuging of the fluid, axial pressure gradient, blade force, dissipative body force and perturbation (non-axisymmetric) effects. The flow is treated as axisymmetric in the duct areas while in the blade area a passage averaging is used to avoid any indeterminacy in defining the S2 surface. At each computing station, initial mid-span static pressure is prescribed to calculate the mass flow rate through the station. Accordingly, the static pressure is adjusted to achieve the desired mass flow.

The blade-to-blade program uses the stream surface geometry from the through-flow analysis to determine the blade section shape. The design is made either in a direct or inverse mode. The program satisfies the aero and structural constraints for the designed blade section.

The stacking line program stacks the designed blade sections from hub to tip to form the three-dimensional blade geometry. It stacks the sections at any circumferential position in the annulus as long as it is structurally acceptable. The reason for this freedom is that the blade sections are viewed as isolated from each other.

While relatively easy and fast, the Q3D method has significant limitations. The particular approach described by Jennions [Ref. 6] is inviscid and does not account for blade lean or sweep. Also secondary flows are not predicted and the flow on each blade section does not communicate with the rest of the flow.

## 2. Three Dimensional Method

Fully three dimensional CFD methods have been incorporated into the design process recently due to the limitations in the Q3D approach. Whether the method



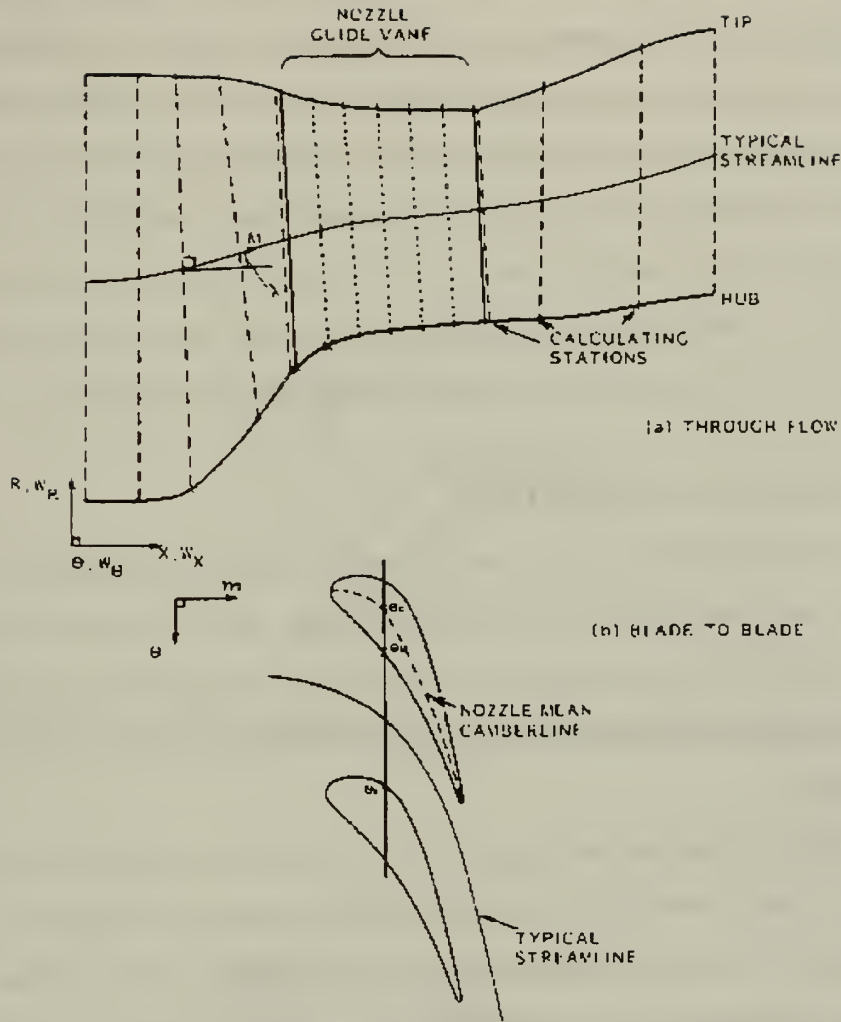


Figure 2. Streamline Curvature Computing Stations and Stream Surface [Ref. 5]

is based on Navier-Stokes equations or Euler equations with boundary layer corrections, the new approach starts with a geometry arrived at by stacking blade sections designed with Q3D methods. The sections may or may not have been 'optimized' for the assumed axisymmetric flow. Then the designer applies the three dimensional solver to the geometry and examines the flow field solution. The blade sections are then changed and restacked to give a new 3D geometry. The process is repeated until the desired performance, both on and off-design, is achieved.

Examples of using 3D CFD codes in the design process for transonic compres-

sor stages are seen in the work of Denton [Ref. 4] and Sanger [Ref. 7]. In both cases a 3D Euler code, incorporating a viscous boundary layer by modelling, was used to analyze the flow through a geometry that was the result of stacked blade-element sections. In the process of modifying the geometry, changes were made to parameters defining individual elements, and the code was then reapplied to analyze the new blade. The geometry packages were similar in that blade elements were defined by a camber line, a distribution of thickness, and leading and trailing edge shapes. The elements were then stacked into a blade by defining the stacking line.

## B. SWEEP ATTEMPTS

In external aerodynamics, swept wings are used very successfully to reduce the drag associated with shock waves. Extending the sweep concept to turbomachinery is not a simple extension however. Conditions are not uniform along the blade span and the internal shock structure is completely different from that found in external aerodynamics.

While the relations between free-stream velocity, wing sections and shock wave structure is easily determined in external aerodynamics; the opposite is true in turbomachinery. Each blade section operates at a different relative flow velocity and flow angle. Centripetal force, tip leakage, secondary flows and non-uniform inlet flow conditions contribute to the problem's complexity. What is commonly observed in transonic rotors is a contained "passage shock". Based on this observation a loss model was developed by Miller et al [Ref. 8], which was later modified by Wennerstrom [Ref. 9].

The initial model shown in Fig. 3, assumed a normal shock in the passage extending from point *A* to point *B*. The blade spacing affects the location of point *B* which is determined by a perpendicular to the mean passage camber line going through the following blade leading edge point *A*. The shock loss is found by averaging the free-stream Mach number and the Mach number resulting from expanding the flow

around the leading edge to point  $B$ . A more detailed model was presented in the same paper (see Fig. 4) that accounts for the varying losses across the passage due to the varying Mach number. The variation in Mach number is calculated by accounting for the bow shock and the expansion waves across the channel. The compressor loss is computed by adding the losses for small stream tubes along the blade span.

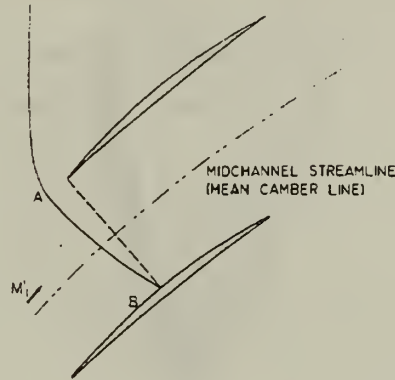


Figure 3. Passage Shock-Wave Configuration for Estimating Shock-Loss Levels [Ref. 8]

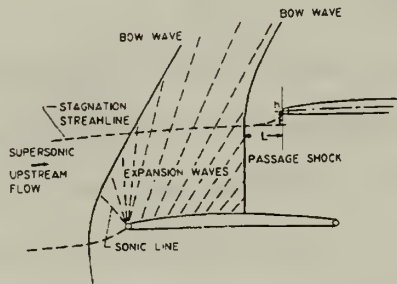


Figure 4. Flow at Inlet of Cascade of Airfoils Operated with Supersonic Relative Inlet Mach Number [Ref. 8]

Calculating the losses with the described model resulted in shock losses higher than the total losses obtained from experimental results. The consistent loss over-prediction was due to the two-dimensional treatment of the shock [Ref. 9]. The second model treated that limitation by considering the shock obliquity in the third dimension Fig. 5. The model follows the first model in the calculation of stream Mach

number and determining the shock location on the suction surface. The shock surface is then constructed and the relative angle between the surface and the free stream is calculated on each section.

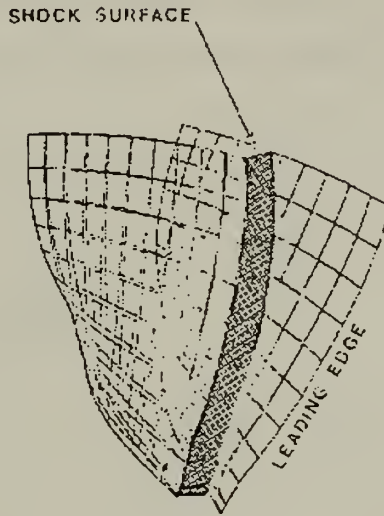


Figure 5. Three Dimensional Shock Surface Between Two Blades [Ref. 9]

## 1. NASA QF-12

In an effort to reduce acoustic noise through the reduction of shock wave-generated pure tones, NASA sponsored the design of a swept fan stage [Ref. 10] with relative inlet Mach number of 1.588. The compound sweep reduced the relative Mach number to an effective Mach number of 0.91 at the mean and tip with a hub Mach number of .83. The fan did not meet the aerodynamic design goals and the acoustic measurements, although below expectations, showed some improvements.

## 2. Neubert et al.

In 1986, two transonic fans were designed [Ref. 10], one was swept back and the other was conventional for the purpose of comparison. The swept design was designed to be shock free with a pressure ratio of 2.21, tip speed of 1558 *ft/s* corrected flow of 1.5 *lb/s*, relative Mach number of 1.6 and adiabatic efficiency of 88.1%. An estimated gain in efficiency of 1.5% was estimated. The loss reduction was due to the



elimination of the calculated shock wave loss and the loss due to the shock boundary layer interaction.

The rotor was designed using a 3D Euler solver with a two-dimensional integral boundary layer procedure to estimate the viscous effects. The design procedure is shown in Figure 6. The numerical solution showed that the Mach number contours on the swept suction surface was spaced out, suggesting that the shock disappeared over most of the blade span. The tip section had some concentration of Mach number contours, but less than the conventional rotor.

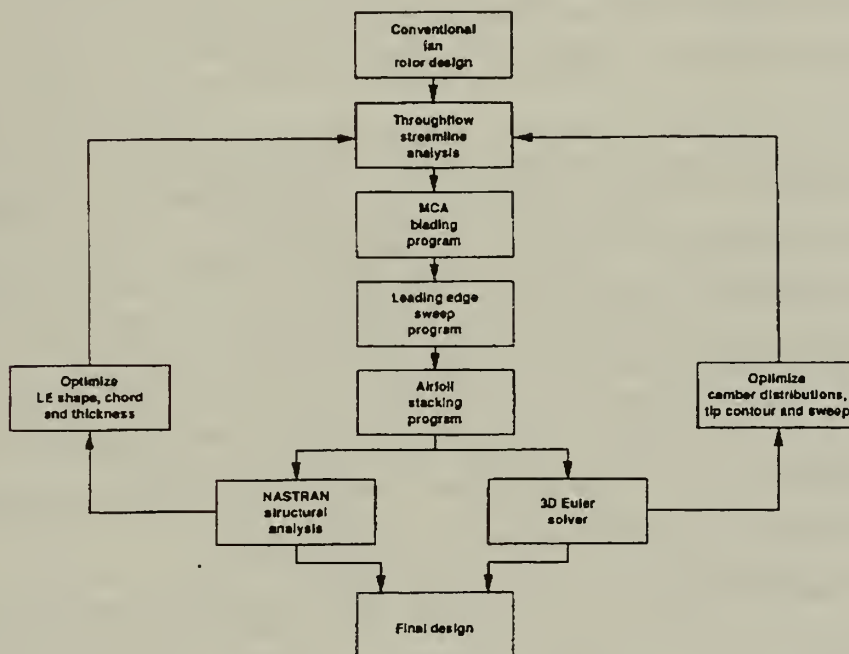


Figure 6. Swept Fan Design Procedure. [Ref. 10]

The test results for the two rotors showed that the swept rotor had poorer performance than the unswept rotor. The pressure ratio was 0.2 lower, the corrected mass flow was less by  $0.9/b/s$  and the stall margin was reduced substantially to  $(0 - 6)\%$  compared to  $13\%$ . There was an improvement of  $0.1\%$  in corrected polytropic efficiency (corrected to match relative Mach number). The difference in performance between the swept and unswept rotors was related to the differences

found in span-wise loading and mass fraction distribution. Detailed measurements showed the existence of a shock surface in the outer half of the swept rotor.

### 3. Puterbaugh et al.

Puterbaugh et al [Ref. 11] designed a swept back rotor derived from a base line geometry [Ref. 12]. The swept design was mainly to evaluate the use of the 3D-shock loss model in the design system, and the overall effect of blade sweep on compressor performance. The detailed design (started from the base line geometry) involved optimizing the blade sections to obtain a circumferentially-averaged static pressure distribution that rose linearly from the leading edge to about 3/4 chord and decreased smoothly to give zero slope at the trailing edge. Relative flow angles, incidence and deviation angles were used to derive the general airfoil shapes. The design parameter (incidence, deviation, loss, work distribution, blockage) selection was based on experience and previously-published designs. The total pressure loss was obtained from the diffusion factor correlation combined with the 3D-shock loss model. Then sweep was added to reduce the shock loss in the rotor. The amount of sweep was increased radially as the Mach number increased to obtain a leading edge profile optimized for minimum shock loss. The structural design was considered while deciding on sweep schedule to ensure structural integrity.

The rotor design goal was for specific flow rate  $214.7 \text{ kg/sec/m}^2$ , pressure ratio 2.04, efficiency 94.0%, tip speed  $457.2 \text{ m/sec}$ . The test results showed that the flow rate was achieved while the pressure ratio fell short by 0.07, efficiency was lower by 3% and the stall margin was 11%. The shock model was found to underestimate the shock sweep angle at mid span while overestimating the angle at the tip. This resulted in lower mid-span work addition.

### 4. Wadia et al.

In an effort to better understand sweep, Wadia et al [Ref. 13] carried out an investigation that included three swept rotors. They designed two swept backward and

one swept forward. The swept-forward rotor and one of the swept-back rotors were swept through tangential lean and required barreling the pitch chord (pitch chord is the midspan chord [Ref. 14]). The other swept-back rotor was swept through tangential lean only. The designs had the same tip speed, inlet-corrected flow, pressure ratio and passage area distribution. The chords and solidity were changed due to mechanical constraints. In addition, the maximum thickness and location of maximum thickness could not be held fixed and were viewed as a part of the sweep package. The forward sweep required added root thickness due to increased blade length, which affected the blade flexural frequency. The two barreled rotor weights were significantly increased. The forward-swept rotor required a change of material to one of superior mean stress capability.

The rotor experimental results were compared to each other and to the baseline rotor (the same as in Puterbaugh et al). The barreled, swept-back rotor showed the worst stall margin (of only 4% compared with 9% for the baseline) with a nearly unchanged (even slightly increased) peak efficiency. The unbarreled swept-back rotor stall margin was 7% and showed an increase in the peak efficiency of 0.9%. The forward-swept rotor had the highest stall margin at 13.5% with an unchanged efficiency. The experiment was supported with CFD analysis which showed that the boundary layer accumulated in the tip region for the swept-back rotors. This accumulation was identified as the main cause of stall margin reduction. The forward-swept rotor was found to have relatively high mass flow rate all the way down to lower speeds. This was interpreted to be due to the unique characteristic of the swept-forward blade sections to untwist (open) as the rotational speed was reduced.

### C. LIMITATION IN CURRENT DESIGN SYSTEM

There has been a major effort made in recent years by the turbomachinery community to improve compressor design. This is evidenced by the increasing number of designs derived using 3D solvers, including a number of swept rotors. Although the

effort is significant there have been no reports of designs using Navier-Stokes solvers. This may be attributed to the fact that they were not available until recently and require large execution times.

One of the main limitations in current design systems is the method for describing the blade geometry. The current methods were quite satisfactory for conventional Q3D designs, before the advent of capable 3D analytical tools. With the introduction of sweep and general blade shapes, designing the blade as independent two-dimensional sections and then stacking them can lead to several problems. Due to the absence of constraints in stacking the blade sections there can be waviness in the final blade surface which is costly to machine. In addition, satisfying geometrical conditions of continuity (of contour, slope and curvature) in each two-dimensional geometry does not necessarily guarantee that condition in the third dimension. In fact, current aerodynamic design blade geometry packages communicate neither well with the structural analysis programs nor with the CNC manufacturing machines. The aerodynamic shape is only approximated in the manufacturing process. Finally, with current geometry packages, the full 3D blade shape optimization problem is unthinkable. For a blade to have from 11 to 22 sections along the span and around twenty coefficients for each section, the optimizer would have from 220 to 440 parameters to perturb. In view of the time it takes the solver to complete one cycle, it is obvious that there is no hope for an optimized solution.

## **D. WHAT NEEDS TO BE DONE**

The geometry packages currently used to design turbomachinery blading are based on the stacking of 2D cascade blade elements. While this representation is required in the Q3D design process, it is not required in the 3D analysis process. Moreover the continued reliance on this representation is inhibiting the generation of designs which are truly optimized on the basis of aero, structural and manufacturing considerations. What is therefore required is a geometry representation that

1. is fully three dimensional in character,
2. involves fewer parameters than current representations,
3. is compatible with structural analysis and CNC machine control programs, without additional approximations,
4. can represent existing geometries to acceptable accuracy,
5. can be programmed to allow changes to the geometry to be made easily by the designer, and those changes to be related to Q3D blade parameters.

The development of such a package and its application to the introduction of sweep into a rotor design, was the goal of the present work.





### III. GEOMETRY REPRESENTATION

#### A. CHOICE OF GEOMETRY REPRESENTATION

Objects can be defined in many different ways. A general curved shape may be represented using a great number of small straight lines or with combinations of several arcs. Many years ago, parts were shaped by deforming a flexible strip of metal by hanging weights at specified points to form a smooth curve. That flexible strip was called a spline. Today, with major advances in manufacturing and in the accuracy that can be achieved in the machining of a part described with numerical data, parametric representation has been adopted for representing spline shapes.

##### 1. Different Geometrical Representations

Both parametric and functional (non-parametric) representation can be used to describe curves and surfaces. Usually the parametric representation is more convenient and more flexible. A circle for example can be represented in non-parametric form by the single equation

$$(x - a)^2 + (y - b)^2 = r^2 \quad (\text{III.1})$$

or in a parametric form, with a variable parameter  $\theta$ , by the two equations

$$x = r \cos(\theta) + a \quad (\text{III.2a})$$

$$y = r \sin(\theta) + b \quad (\text{III.2b})$$

The parametric representation can be of different forms. Some of the representations available are Hermite, Bezier, and uniform B-splines which are described respectively by

$$\begin{aligned} Q(t) = & (2t^3 - 3t^2 + 1)P_1 + (-2t^3 + 3t^2)P_4 + \\ & (t^3 - 2t^2 + t)R_1 + (t^3 - t^2)R_4 \end{aligned} \quad (\text{III.3})$$

$$Q(t) = (1-t)^3 P_1 + 3t(1-t)^2 P_2 + 3t^2(1-t) P_3 + t^3 P_4 \quad (\text{III.4})$$

$$Q(t) = \frac{(1-t)^3}{6} P_{i-3} + \frac{3t^3 - 6t^2 + 4}{6} P_{i-2} + \frac{-3t^3 + 3t^2 + 3t + 1}{6} P_{i-1} + \frac{t^3}{6} P_i \quad (\text{III.5})$$

$Q$  is a coordinate of a point on the curve. The  $P$ 's and  $R$ 's are the corresponding blending function weights.

Hermite curves are defined by two end control points and the tangents at the end points. Fig. 7 shows the blending functions used to generate Hermite curves (the polynomials which are coefficients of  $P_1, P_4, R_1$ , and  $R_4$  in Eq. III.3) and a Hermite curve.

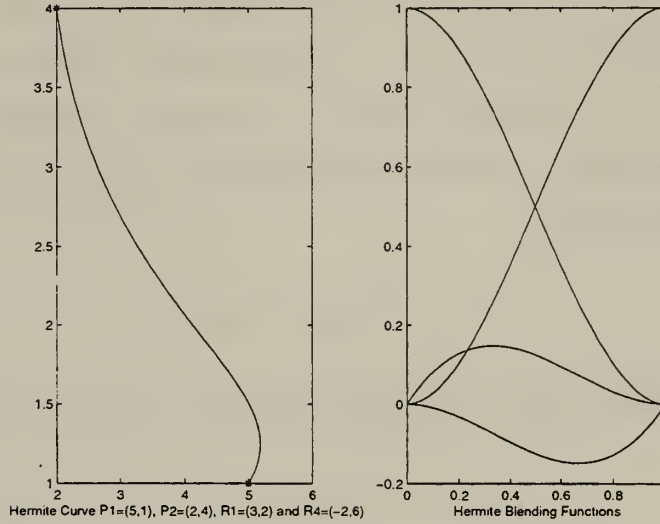


Figure 7. Hermite Representation

Bezier curves are defined by four control points, two of which are the end points. The other two are not on the curve but with the end points define the tangents at the end points. Fig. 8 shows the Bernstein polynomials (which are the polynomial coefficients of the  $P$ 's in Eq. III.4) and a Bezier curve with its four control points.



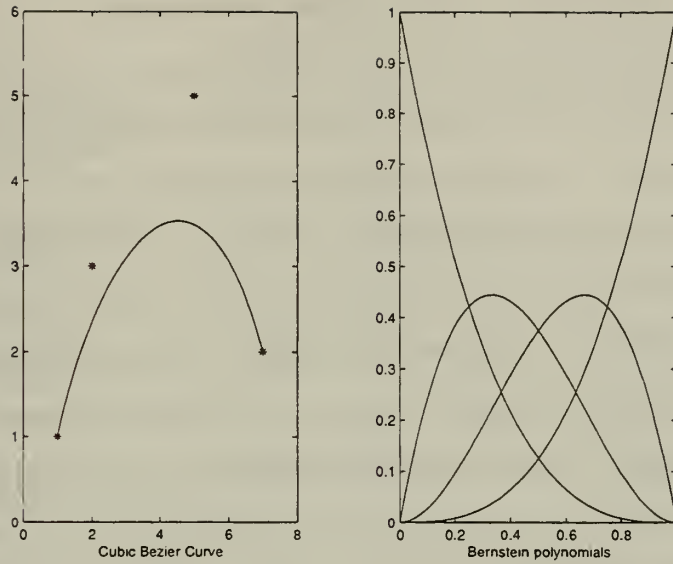


Figure 8. Bezier Curve Representation

The B-spline is a general representation, which does not intersect with any of its control points. It defines multiple segments of curves with a uniform parameter. Fig. 9 shows the basis functions and a one segment B-spline.

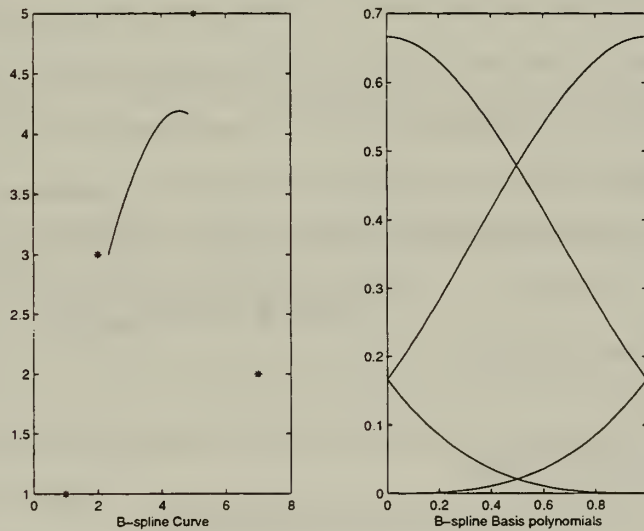


Figure 9. B-Spline Representation

## 2. Advantages and Disadvantages

Each of the above-mentioned representations has particular advantages and disadvantages. Parametric representation is advantageous to the functional representation in the ability to represent shapes easily, define a part of a standard geometry, and to represent a complex geometry. All have defined tangents. More complex geometries may be represented by higher-order functional representations which are hard to control between points, and can wiggle. The polynomial coefficients have no direct link to the geometry shape. The curve or surface functional representation has to be complemented with the range of definition. The advantage of the functional representation is the ease of determining if a given point lies on the curve or not.

Between the different parametric representations, there are advantages and disadvantages although there is a transformation matrix between the corresponding forms. Table I shows a comparison between the properties of the different forms. Items appearing in the table will be addressed in the following discussion.

## 3. Selected Representation

The representation selected here for blade geometry is the cubic Bezier representation. In addition to the properties that will be presented in the following sections, they hold the particular advantage that the control points are the end points (leading and trailing edge points) and points that control the slopes at those end points. They can be imported into any CAD/CAM program with no approximation as they are a special case of NURBS (Non Uniform B-Splines). They are widely used for representing curves and surfaces.

## B. BEZIER CURVES

### 1. Mathematical Representation

Bezier curves can be represented in many different forms. The forms are equivalent and give the same results. Each variable is defined by its own control points and the same blending functions. For curves of dimensions higher than one,

	Hermite	Bezier	Uniform B-Spline	Nonuniform B-Spline
Convex hull defined by control points	N/A	YES	YES	YES
Interpolates some control points	YES	YES	NO	NO
Interpolates all control points	YES	NO	NO	NO
Ease of subdivision	Good	Best	Avg	High
Continuities inherent in representation	$C^0 G^0$	$C^0 G^0$	$C^2 G^2$	$C^2 G^2$
Continuities easily achieved	$C^1 G^1$	$C^1 G^1$	$C^2 G^2$	$C^2 G^2$
Number of parameters controlling a curve segment	4	4	4	5

Table I. Comparison of Properties of Different Forms of Parametric Cubic Curves [Ref. 15].

the control points represent vectors in the corresponding space. All the following representations will be given for the cubic form.

**a. Polynomial Form**

This form of the Bezier representation is not commonly written but is included here because polynomial representations have been the most widely used in generating blade shapes:

$$Q(t) = (-p_0 + 3p_1 - 3p_2 + p_3)t^3 + (3p_0 - 6p_1 + 3p_2)t^2 + (-3p_0 + 3p_1)t + p_0 \quad (\text{III.6})$$

In the above equation, the constant term,  $p_0$ , is the first control point and the last control point,  $p_3$ , is sum of the polynomial coefficients.

### *b. Bernstein Form*

The Bernstein polynomials are recursive polynomials. The higher order polynomial is calculated from the next-lower degree polynomial, namely

$$B_i^n(t) = (1-t)B_i^{n-1}(t) + tB_{i-1}^{n-1}(t). \quad (\text{III.7})$$

The Bernstein polynomial is given in the binomial form as

$$B_i^n(t) = \binom{n}{i} t^i (1-t)^{n-i}. \quad (\text{III.8})$$

The Bezier formula is then .

$$Q(t) = \sum_{i=0}^n p_i B_i^n(t) \quad (\text{III.9})$$

### *c. Matrix Form*

The matrix form of the Bezier representation is

$$Q(t) = [p_0 \ p_1 \ p_2 \ p_3] \begin{bmatrix} 1 & -3 & 3 & -1 \\ 0 & 3 & -6 & 3 \\ 0 & 0 & 3 & -3 \\ 0 & 0 & 0 & 1 \end{bmatrix} \begin{bmatrix} t^0 \\ t^1 \\ t^2 \\ t^3 \end{bmatrix}. \quad (\text{III.10})$$

The matrix form is useful for computer implementation, especially if matrix multiplication is hard wired.

## **2. Cross Plots**

The Bezier curve in the  $xy$  plane or the  $xyz$  space is composed by cross plotting the coordinates in terms of each other for given values of the parameter  $t$ . This is illustrated in Fig. 10 for the two-dimensional case.

## **3. Effect of Moving Control Points**

Bezier curves are sensitive to control point movements. For example, moving the third control point of the Bezier curve shown in Fig. 11 by 20% of the tangent length in the positive and negative directions changes the shape of the solid curve to become the broken curves. Notice the curve is moved in the same direction as the control point.

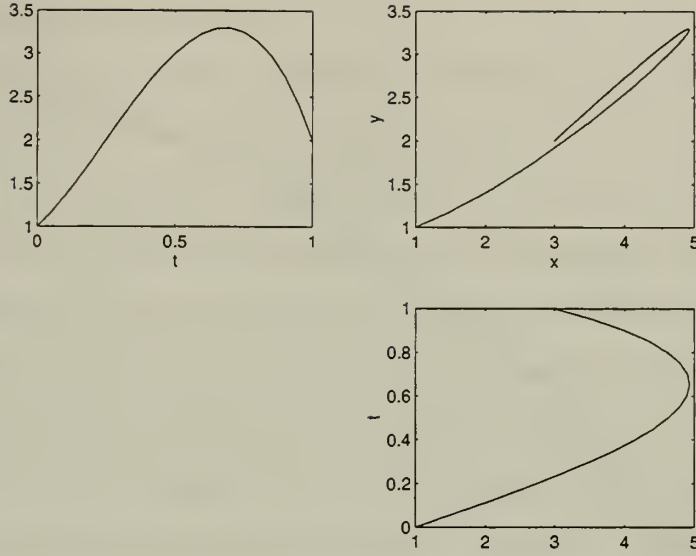


Figure 10. Cross Plot

#### 4. Properties of Bezier Curves

Bezier curves have properties that make them particularly attractive for design and graphics. They are invariant under translation, rotation and scaling but not under perspective projection. 'Convex hull', linear combination and end point interpolation are also interesting properties.

##### a. *Convex Hull*

The 'convex hull' property of the Bezier curve is that the curve is contained inside the polygon of the control points defining the curve, as shown in Fig. 12. This is helpful in knowing the extent of the curve without computing it.

##### b. *Invariance*

The Bernstein polynomials are affine map invariant, which is stated as  $\sum_{j=0}^n B_j^n(t) = 1$ . This makes the Bezier curves invariant under translation, rotation and scaling. That allows applying transformations to the four control points and then calculating the transformed curve. The equation

$$Q(t) = \sum_{j=0}^n p_j B_j^n(t) + a = \sum_{j=0}^n (p_j + a) B_j^n(t) \quad (\text{III.11})$$

shows that translation applied to the control points, or to the curve, is equivalent.

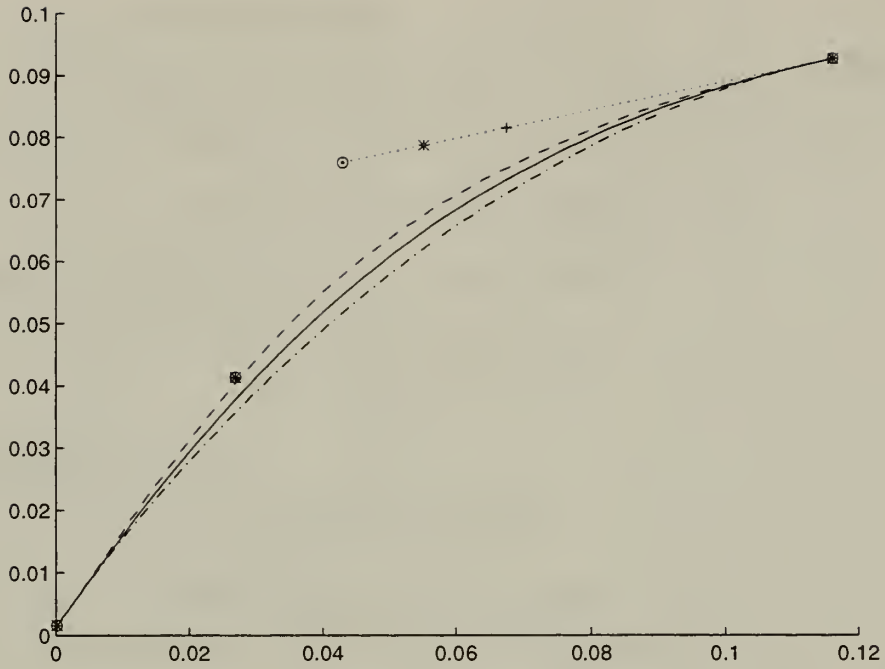


Figure 11. Control Point Movement Along The Tangent Direction

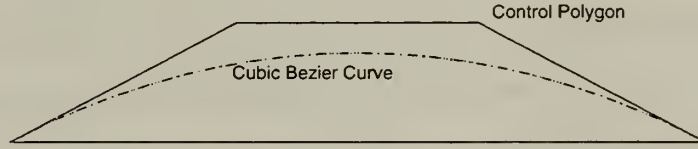


Figure 12. Convex Hull Property

The curves are also invariant under linear combination, since

$$\sum_{j=0}^n (\alpha b_j + \beta c_j) B_j^n(t) = \alpha \sum_{j=0}^n b_j B_j^n(t) + \beta \sum_{j=0}^n c_j B_j^n(t) \quad (\text{III.12})$$

### c. *Location of Maximum Effect*

Examining the Bernstein polynomials, each one is seen to have only one maximum. That maximum is at  $t = \frac{i}{n}$  [Ref. 16], where  $i$  is the number of the term in eqn. III.4 and  $n$  is the order. So to change the curve at one third of the parameter, the second control point movement would give the maximum effect.



## 5. Differentiation

The derivative for a Bezier curve can be obtained simply by differentiating any of the given forms. It is worth mentioning though that the derivatives have direct relationships to the control points. By looking at the polynomial form in Eq. III.7 it can be seen that the order of the polynomial for the derivative will be reduced by one and that the derivative at zero will be three times the difference between the first two control points. This is not only true at the end points. The polynomial for the derivative for the whole curve is a Bezier curve of order one degree less than the curve itself (second order in our example). The control points for that curve are simply the difference between the successive central points of the curve being differentiated, or

$$\frac{d}{dt}Q(t) = n \sum_{j=0}^{n-1} (p_{j+1} - p_j) B_j^{n-1}(t) \quad (\text{III.13})$$

## 6. Continuity Between Curves

CAD/CAM application requires more than one curve to be joined together. The requirement on connecting two curves may vary from one case to another. An application may require curves joining with first derivative being continuous or be both first and second-derivative continuous. For first-derivative continuity, the two curves have to have equal tangents, or one has to be a multiple of the other. That would be satisfied by forcing the three joining control points to be collinear as shown in Fig. 13.

Curvature continuity can be ensured by arranging the control points on each side to maintain a common ratio between the segment lengths shown in Fig. 14

## 7. Difference Between $C$ & $G$

A function with a continuous second derivative would be called  $C^2$  continuous. This notion is still valid for parametric representation, with reference to variation in the parameter. When cross plotting two parametric curves however, the resulting curve might not have the same degree of continuity that was inherent in the original curves. In this case we have another type of continuity which is called geometric

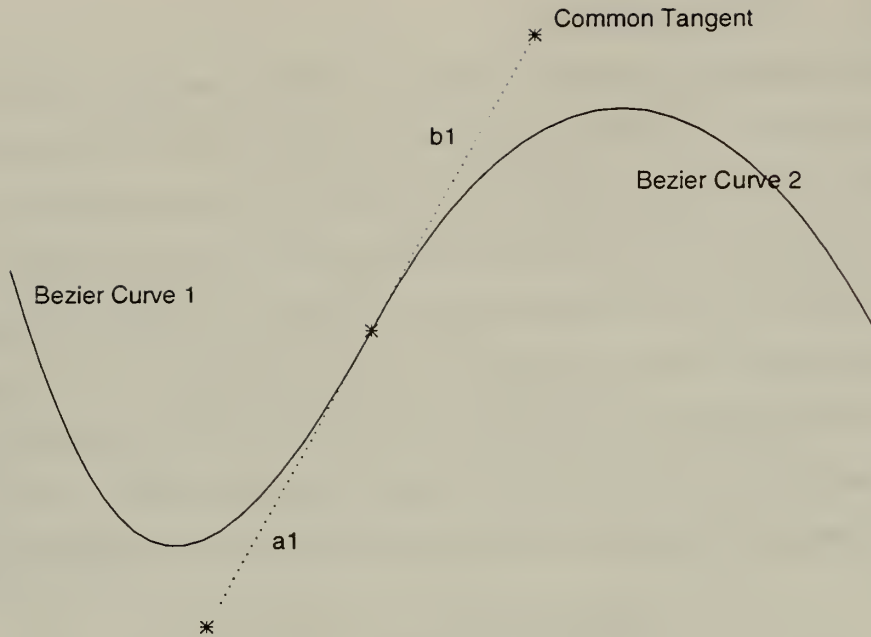


Figure 13. Two Bezier Curves with First-Derivative Continuity

continuity (e.g.  $G^2$  for geometric curvature continuity). Having one type of continuity does not guarantee the other type of continuity. The geometric continuity is less constraining and the more important to design applications.

## 8. Subdivision

One of the interesting properties of Bezier curves is subdivision. Given a Bezier curve with a set of control points, we can always find two sets or more of control points.

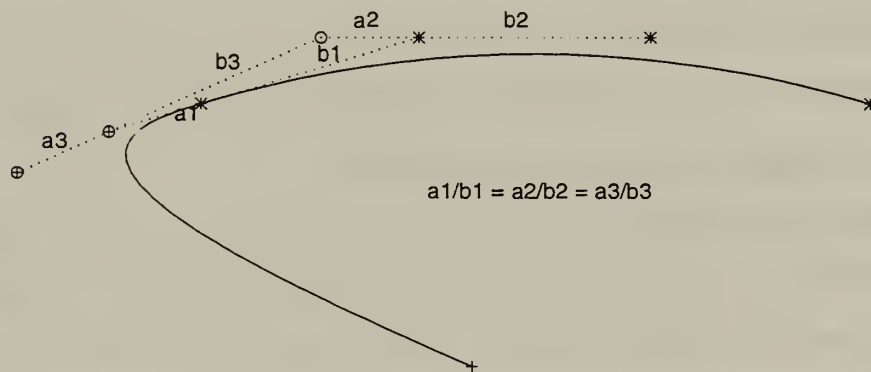


Figure 14. Condition for Second-Derivative Continuity for Bezier Curves

Each of these would represent the corresponding segment exactly while maintaining  $C^3$  continuity. The procedure is relatively easy and straightforward. Consider the control polygon defined by the control points starting from the first point to the last ( $P_0, P_1, P_2, P_3$ ) as shown in Fig. 15 and a parameter  $t_s$  where subdivision is to occur. The control points ( $a, d, f, e, c$ ) can be found using the equations

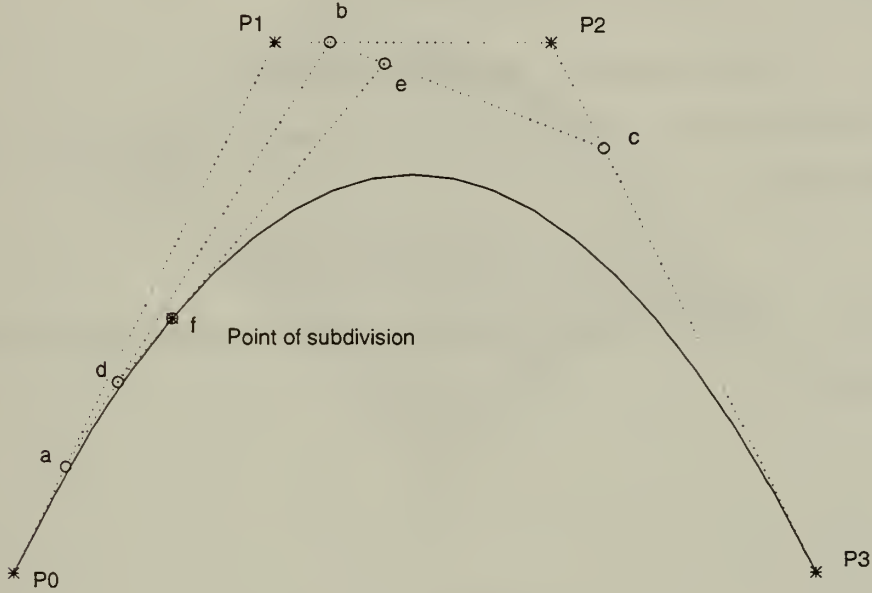


Figure 15. Bezier Curve Subdivision

$$a = t_s P_1 + (1 - t_s) P_0 \quad (\text{III.14})$$

$$b = t_s P_2 + (1 - t_s) P_1 \quad (\text{III.15})$$

$$c = t_s P_3 + (1 - t_s) P_2 \quad (\text{III.16})$$

$$d = t_s a + (1 - t_s) b \quad (\text{III.17})$$

$$e = t_s b + (1 - t_s) c \quad (\text{III.18})$$

$$f = t_s d + (1 - t_s) e \quad (\text{III.19})$$

We obtain two Bezier curves defined by ( $P_0, a, d, f$ ) and ( $f, e, c, P_3$ ).

## C. BEZIER SURFACES

Bezier surfaces are defined by sixteen control points. The edges by themselves are Bezier curves. The surfaces possess the same properties as the curves. An individual Bezier surface is called surface patch. Surfaces can be formed by joining surface patches together with the required degree of continuity. Usually surface continuity is more difficult to satisfy than continuity for curves.

### 1. Mathematical Representation

The Bezier surface is defined with two parametric variables  $u, v$ . The form of the Bezier patch is

$$Q(u, v) = \sum_{i=0}^n \sum_{j=0}^m p_{ij} N_i^n(u) M_j^m(v) \quad (\text{III.20})$$

where  $N, M \dots$  are Bernstein polynomials. A Bezier surface with its control net is shown in Fig. 16.

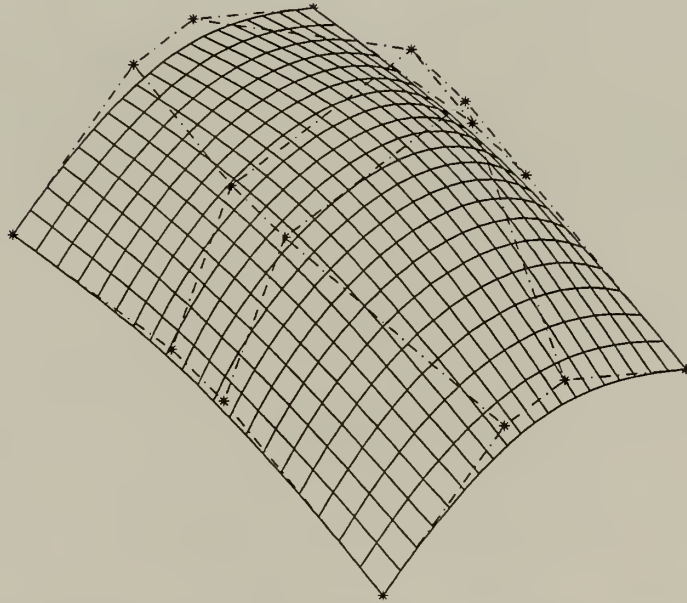


Figure 16. Bezier Surface with its Control Net

## 2. Effect of Moving Control Points

The effect of moving one of the inner control points for the surface shown in Fig. 16 is illustrated in Fig. 17. Only one coordinate of the control point was changed in this example.

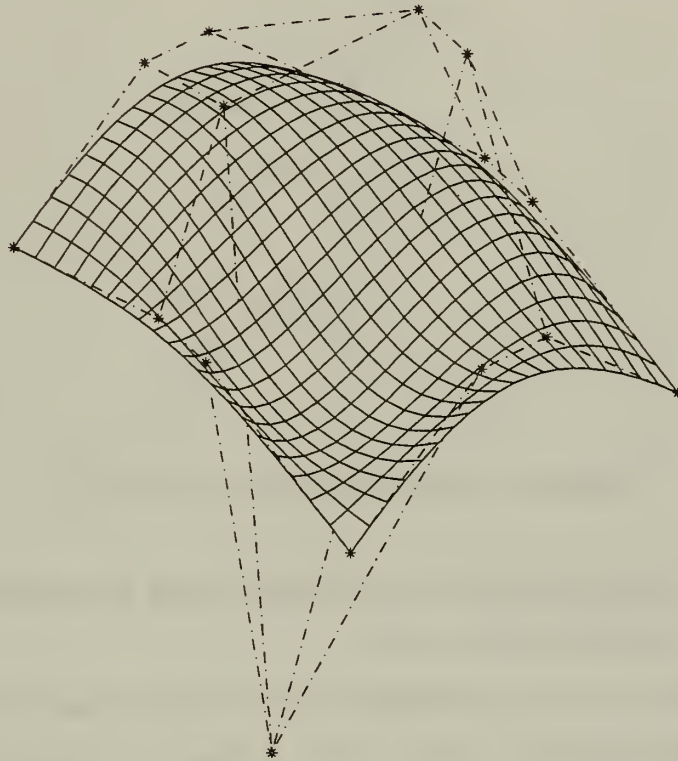


Figure 17. Effect of Surface Control Point Movement

## 3. Continuity Between Surfaces

The conditions for surface continuity are the same as for the curves with the extra condition that the four tangents along the connecting edge shown in Fig. 18 must be such that  $a_1/b_1 = a_2/b_2 = a_3/b_3 = a_4/b_4$ .

## D. PARAMETERIZATION

In the previous section we dealt with the problem of calculating a surface from a given set of control points. This is not always the case, if we already have the

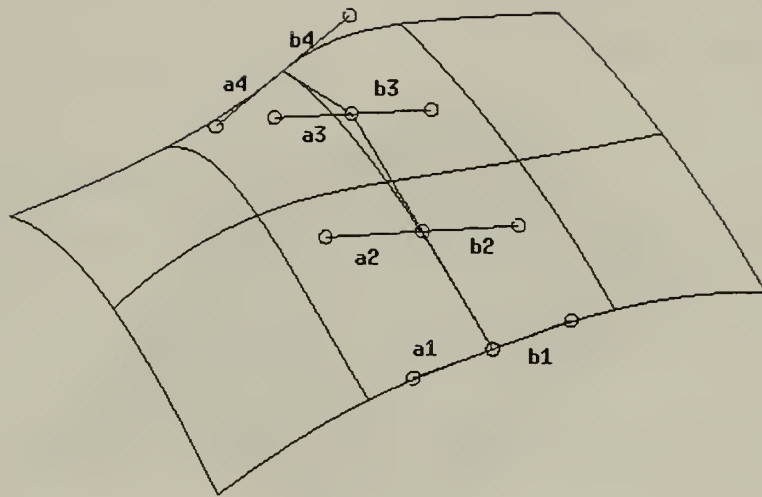


Figure 18. Tangency Condition for Surfaces

geometry as a set of data points we would like to obtain the set of control points that best represents the surface data points.

The problem is solved by finding the best parametrization for the given curve or surface. Hoschek [Ref. 17] solved the problem by splitting it into two least-squares problems. The first is the least-squares problem of finding the control points for the surface that best fits the given geometry data points assuming a given parameterization. The second is a nonlinear least-squares problem that solves for the best parameterization given the data points and a set of control points.

The solution procedure described by Hoschek [Ref. 17] is iterative and proceeds as follows:

1. Find an initial parameterization using a suitable method (arc length for example).
2. Apply least squares to find the approximating control points.
3. Calculate the error vector  $D_i$  at each point (see Fig. 19).



4. Find the parameter correction at each point by calculating the dot product of the error vector and the tangent vector at the corresponding point. Then scale with the ratio of the parameter length to the total arc length.
5. Repeat until the solution converges.

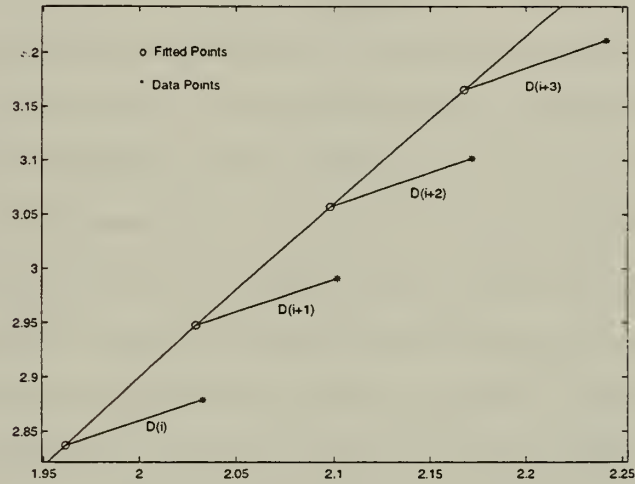


Figure 19. Error Vector  $D_i$  for Parametrized Data



## IV. INITIAL GEOMETRY PACKAGE

As a first step, the suitability of the Bezier representation for describing typical 2D compressor blade section profiles was examined. It was found that Bezier curves were suitable and the blade shape was well represented. Second, a complete blade was treated as two separate surfaces, pressure and suction surfaces, and the representation was again found to be suitable. After representing the pressure and suction surfaces with Bezier patches, leading and trailing (Bezier) surfaces were added. This resulted in a complete blade represented in a form that was compact (32 control points and 2 parameter values) and also easy to handle, and easy to import into different programs without approximation. Most importantly, the coordinates at any position on the blade surfaces could be retrieved with no loss in accuracy (other than that due to machine precision), because the shape was analytically described.

The package was implemented with current compressor design systems in mind. The initial package can read an existing geometry specified in merid12, merid13 and general format [Ref. 18]. The package can also read the control points that represent the six surfaces or only the ones that represent the pressure and suction surfaces, and then add leading and trailing edge surfaces. Also, to facilitate further development and the addition of a graphical user interface, the package was implemented using object-oriented programming.

The blade surfaces are numbered from 1 to 6 as shown in Fig. 20. The control points for each surface are numbered from 0 to 15 as shown in Fig. 21. Where surfaces are joined, the surface edge with the lower numbered control points is always on the left (when moving clockwise around the blade). For example, surface No. 2 (pressure side) control points (3, 7, 11, 15) will match (are the same as) control points (0, 4, 8, 12) of surface No. 3.

The blade geometry is manipulated by moving control points individually or in-groups defined in the program. The groups are defined such that one row of control

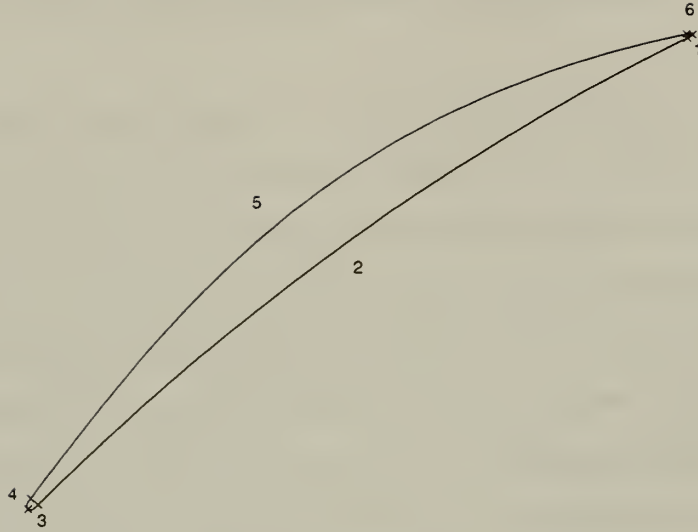


Figure 20. Blade Surface Numbering

points for the six surfaces can be moved simultaneously. The movements allowed give the freedom to shape the geometry with great flexibility.

The use of the present representation is new to axial turbomachinery and by no means is the present work considered to be complete as an exploration of the potential of the representation. The present work only demonstrates proof-of-concept. The intent was to find a rational approach to design with sweep. In that context, basic blade geometry manipulation routines and prescribed parameter variations were implemented. Specifically, two blade sweep schedules, blade lean, and individual control point manipulations were programmed to be computed relative to a reference geometry.

## A. APPROXIMATING BLADE GEOMETRY

The blade geometry is read in as  $r, z, \theta_1, \theta_2$  as defined by either meridl3 or meridl2. Meridl3 reads in the blade section with  $\theta_1$  being the mean camber line tangential coordinate and  $\theta_2$  the tangential thickness angle. Meridl2 reads in the pressure surface and suction surface tangential coordinates as  $\theta_1$  and  $\theta_2$  respectively.



Figure 21. Control Point Numbering

In either case, the coordinates are transformed to  $x, y, z$  coordinates and the surfaces are treated as two separate surfaces by the program. The surfaces are assumed to start and end at their defined leading and trailing edge tangency points respectively. Each surface is fitted by a Bezier surface separately using the method presented by Hoschek [Ref. 17]. The fitting routine starts with initial parameterization that uses the cubic root of the arc length. The linear least-squares fitting uses  $QR$  factorization, while the parameter correction uses the method given by Hoschek [Ref. 17].

The equation for the initial parameterization is

$$dt_i = \left( \frac{ds}{\sum_i ds_i} \right)^{\frac{1}{3}} \quad (\text{IV.1})$$

where  $s$  is the distance along the curve. The parameter interval is then normalized

$x$	$y$	$t$	$t_a$	$t_s$	$t_c$	$e_a$	$e_s$	$e_c$
1.0000	1.0000	0	0	0	0	0	0	0
1.8990	2.0320	0.1000	0.1226	0.1059	0.1007	-0.0226	-0.0059	-0.0007
2.3466	2.4355	0.1500	0.2347	0.2072	0.1985	-0.0847	-0.0572	-0.0485
3.6730	3.3040	0.3000	0.3379	0.3044	0.2936	-0.0379	-0.0044	0.0064
4.1071	3.5095	0.3500	0.4340	0.3982	0.3865	-0.0840	-0.0482	-0.0365
4.5360	3.6880	0.4000	0.5243	0.4891	0.4775	-0.1243	-0.0891	-0.0775
5.3750	4.0000	0.5000	0.6101	0.5777	0.5669	-0.1101	-0.0777	-0.0669
6.5754	4.4905	0.6500	0.6924	0.6645	0.6551	-0.0424	-0.0145	-0.0051
7.3281	4.9375	0.7500	0.7720	0.7498	0.7423	-0.0220	0.0002	0.0077
7.6880	5.2240	0.8000	0.8495	0.8340	0.8288	-0.0495	-0.0340	-0.0288
8.0359	5.5645	0.8500	0.9253	0.9173	0.9146	-0.0753	-0.0673	-0.0646
9.0000	7.0000	1.0000	1.0000	1.0000	1.0000	0.0000	0	0

Table II. Different Parameterization ( $t$  = parameter,  $e$  = error; subscripts a,s,c are arclength, square root and cubic root).

by calculating

$$dt_i = \frac{dt_i}{\sum_i dt_i} \quad (\text{IV.2})$$

Table II shows the accuracy of predicting the initial parameter this way versus using the arc length or the square root of the arc length. The first three columns of the table were generated by calculating data points from Bezier control points with an unevenly spaced parameter  $t$ . The next six columns compare the various approximations.

Since Bezier surface corner points are control points, the values for the corner points are substituted into the equations to fix the corners. The number of equations is then reduced by four. The problem becomes a classical least-squares problem in 12 unknowns.

The nonlinear part is solved by calculating the error vector at each point and calculating its inner product with the surface tangent with respect to both  $u$ , and  $v$  parameters [Eq.III.20]. The result is scaled with respect to the corresponding arc length and added to the parameter value at each corresponding point.

Two-dimensional blade sections were tested to determine the suitability of the representation. Two test cases are shown in the Fig 22 and Fig. 23.



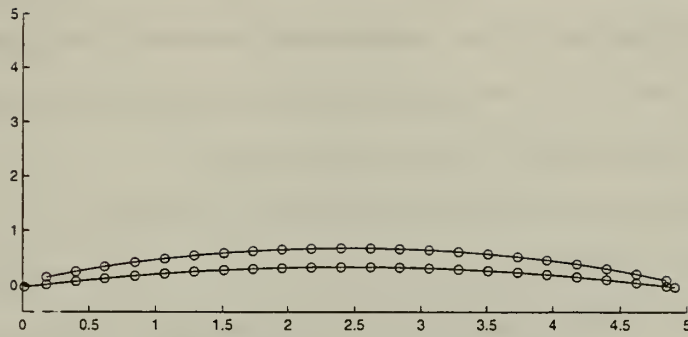


Figure 22. Double Circular Arc Blade Section [Bezier Approximation]

## B. ADDING LEADING AND TRAILING EDGE SURFACES

The two Bezier surfaces that represent the blade pressure surface and suction surface need to be closed to form the blade geometry. In defining the leading and trailing surfaces there are two considerations. First, the connecting edges have to maintain the appropriate continuity requirement. Second, a certain amount of flexi-

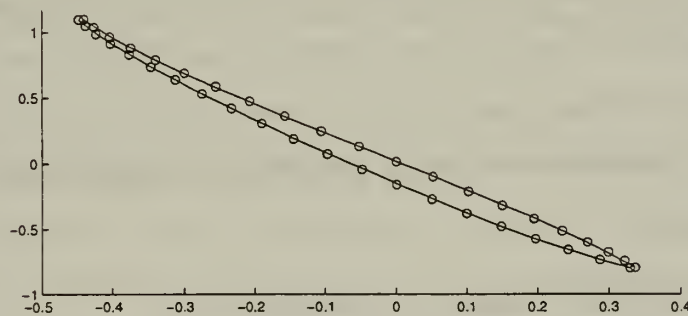


Figure 23. Transonic Fan Blade Section [Bezier Approximation]

bility should be provided so that the leading edge bluntness can be changed. Joining the two surfaces by one surface, with even the least amount of continuity, would not satisfy these requirements. Two surfaces were judged able to satisfy curvature continuity at the pressure and suction sides while having at least tangent continuity at the edge connecting the two added surfaces together.

The leading surfaces are defined by the constraints on the ratio of the tangents to the blade surfaces, and their common edge. This determines the chord-wise extension added by the leading (and trailing) surfaces. Since the requirement is to have constant ratio of tangents along the surface edge [Fig. 17], and the arc length is larger at the tip than at the hub, the tip extension will be larger than the hub extension. The chord length is therefore adjusted by applying subdivision to bring the chord length back to the desired length.

After adding the leading and trailing surfaces the blade is fully defined, with the six surfaces numbered as shown in Fig 21 from 1 to 6 (clockwise starting from the edge connecting the two trailing edge surfaces).

## C. EXAMPLES OF GEOMETRY MANIPULATION

The manipulations implemented in the present package are of two types. One is a general point manipulation in which each individual control point can be moved in any of the three coordinate directions  $(r, z, \theta)$ . Second is a programmed manipulation in which a defined set of control points is moved in any of the three directions  $(r, z, \theta)$ . This second type includes a manipulation in which the blade is swept along the blade chord. This is applied either to the top row of control points (sweep\_1) or to the top two rows (sweep\_2).

### 1. General (Point) Manipulation

The general manipulation of the control points allows the designer to move the individual control points in any of the three coordinate directions  $(r, z, \theta)$ . Each point can be moved in one direction at a time. The axial direction  $(z)$  and radial

direction ( $r$ ) are in the same units as are used for the data read by the program. The tangential coordinate is in radians. The following Fig.24 shows the effect on the blade geometry of moving one (surface edge) control point in the tangential direction.

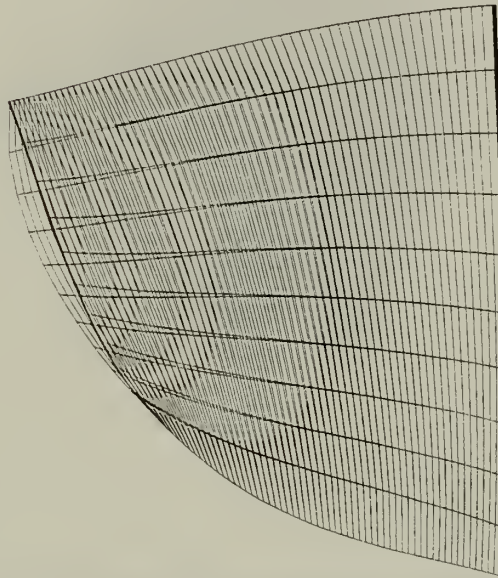


Figure 24. The Effect of Moving Control Point 11 in the Tangential Direction .05 Radians

## 2. Programmed (Shape) Manipulation

The programmed (shape) manipulations, as currently implemented, move all the control points for the six surfaces that share the same row number, simultaneously. The tangential movement of the top row or top two rows give different types of blade lean. By moving each row individually, different lean schedules can be obtained. Figures 25 and 26 show examples of the effect of tangential perturbations.

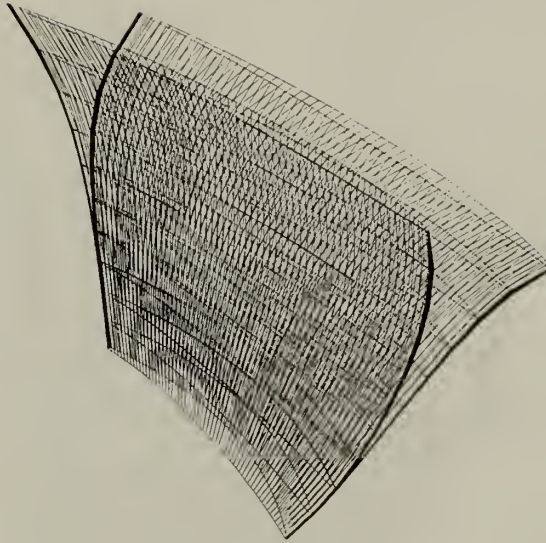


Figure 25. Blade Lean Created by Moving the Top Row of Control Points (0.05 Radians in Each Direction).

Two special manipulations were implemented for sweep. Both sweep the blade tip along the chord direction either forward or backward. The first (sweep\_1) moves only the top row of control points a prescribed percentage of the rotor chord in the required direction (see Fig. 27). The second (sweep\_2) moves the top two rows of control points simultaneously, the same fraction of chord, in the same way as in sweep\_1 (see Fig. 28). Moving one row of control points will affect the whole blade span, but with gradually decreasing effect the further the distance from the row being moved.

The chord slide or 'sweep in the chord direction' implemented in sweep\_1 and sweep\_2 is achieved by a composed  $(z, \theta)$  manipulation. The movement of the

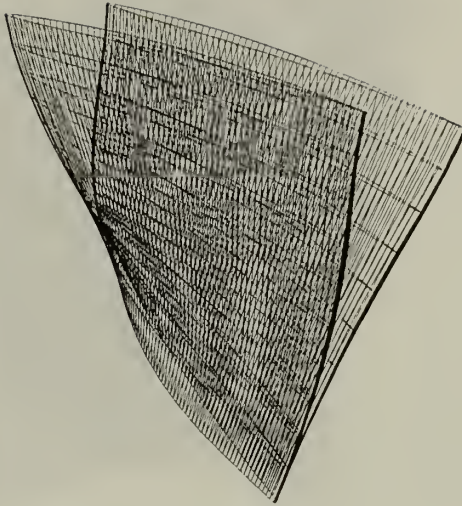


Figure 26. Blade Lean Created by Moving the Top Two Rows of Control Points (0.05 Radians in Each Direction).

tip section is shown in Fig. 29. The axial displacement required is calculated as a percentage of the axial chord. That percentage is the parameter passed to the function. The tangential displacement is calculated from the rate of change of the tangential coordinate along the chord. Sweep\_2 preserves the original blade slope at the wall, whereas sweep\_1 does not.

## D. PROGRAM LANGUAGE AND STRUCTURE

A listing of the initial version of the code is given in [Ref. 19]. The package was implemented using C++ object-oriented programming. The program consists of six classes. Some of the classes are used as tools by the main classes. The class is



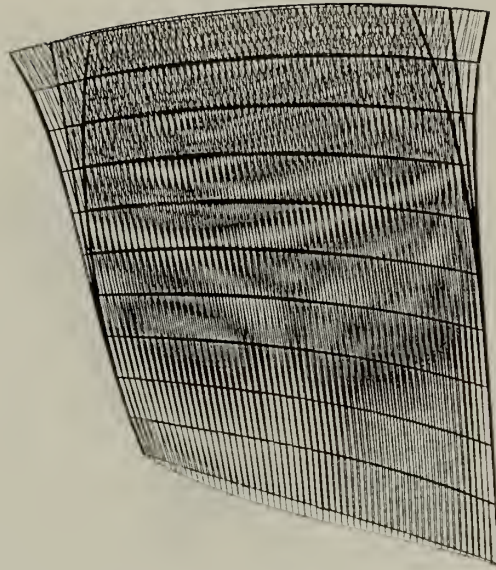


Figure 27. Forward and Aft Sweep (10% of Chord) Using Sweep\_1.

considered an entity with defined functions. The user is allowed only access to class members through the class interface (class member functions). This facilitates the development because once the class is developed it is not affected by the following development in the program. The application that uses the class works through the interface and is not affected by the internal implementation. For example, one of the member functions in the blade class is the "read\_surf" function that reads the pressure and suction surfaces, transforms the data to  $(x, y, z)$  coordinates, fits the two Bezier surfaces, and then adds the leading and trailing edge surfaces.

The classes used in the program are named point, vector, matrix, surface, bsurface and blade. A brief explanation of each of the classes will follow.



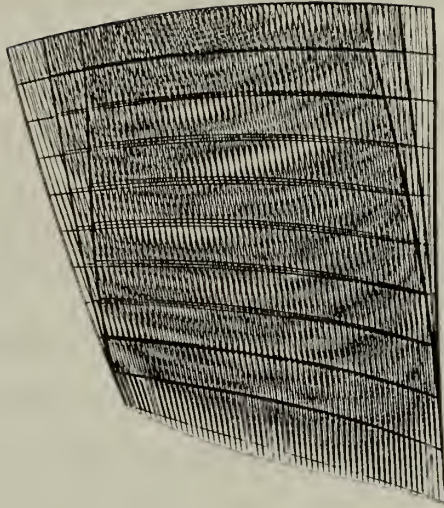


Figure 28. Forward and Aft Sweep (10% of Chord Using Sweep\_2).

## 1. 'point'

The point class represents a point in space. The class members are three variables of type double  $(x, y, z)$ . Since a point in space is considered a vector from the origin to that point, the point class will have some of the vector operations implemented. The functions defined for the class are

1. scalar multiplication and division;
2. addition, subtraction, inner product and vector norm;
3. print, single coordinate retrieval (e.g. value of  $x$  only).



Figure 29. Sweep with Both Forward and Aft-Sweep of 10% of Chord

## 2. 'vector'

The vector class represents an array of points of type double. The class was constructed to facilitate the matrix vector operations. The class members are the vector dimension of type integer and the vector starting address. The functions defined for the vector are

1. vector - constant addition, multiplication, division and subtraction;
2. vector - vector addition, subtraction, multiplication (cross product);
3. vector - matrix multiplication;
4. dimension retrieval, vector norm, vector norm squared, index of maximum value, assign value to an element of the vector, element retrieval and range of element retrieval.

### 3. 'matrix'

Matrix class members are double array of type double, row dimension of type integer and column dimension of type integer. The functions defined for the class are

1. matrix - matrix multiplication, addition, subtraction;
2. matrix - vector multiplication;
3. retrieval of element, submatrix, row dimension, column dimension;
4. QR factorization;
5. set the value of an element and resize the matrix dimension.

### 4. 'surface'

Surface class members are a double array of type point, row dimension and column dimension. It is equivalent to a three dimensional array of size  $row \times col \times 3$ . The functions defined for the class are

1. retrieval of row dimension, column dimension, element and component of an element;
2. surface - matrix multiplication;
3. surface - surface subtraction;
4. set value of surface elements, value of individual element with a point, value of an individual element with three values of type double.

### 5. 'bsurface'

The bsurface class represents the Bezier control points for a surface. The class members are surface of dimension  $4 \times 4$ , matrix  $u$  for the parameter  $u$ , matrix  $v$  for the parameter  $v$ , column dimension and row dimension for the two matrices (both have the same dimension). The functions defined for the class are

1. retrieval of an element, print, surface calculation, one point calculation for either an index of the parameters the value of the parameters, resize the parameter matrices;

2. fit a Bezier surface to given surface, first derivative *w.r.t* to  $u$  or  $v$  at each point or specific point;
3. find the parameter  $u$  for a given  $v, z$ , the parameter  $v$  for a given  $u, x$  and both the parameters  $u, v$  for a given  $x, z$ ;
4. calculate conical sections on the surface.

## 6. 'blade'

The blade class represents the blade geometry with its six bsurfaces, number of blade sections, number of points on each of the pressure and suction surfaces, number of points on trailing edge and number of points on the leading edge. The functions defined for the blade are

1. read surface data in either data points format or control point format;
2. print output in PLOT3D format, control points or general format in the  $(r, z, \theta)$  coordinates for grid generation;
3. control point manipulation and subdivision.

## V. APPLICATION TO THE INCORPORATION OF SWEEP

The geometry package was used to investigate swept geometries. Sweep perturbations were implemented using the package predefined routines. After creating a geometry, the blade coordinates were calculated on conical sections for the grid generator. The grid generator used was TCGRID supplied to the Naval Postgraduate School by the NASA Lewis Research Center [Ref. 20]. The generated grid was checked before the CFD solver was applied. The viscous code used here was RVC3D "Rotor Viscous Code 3-D", also supplied by NASA Lewis [Ref. 18]. The code outputs the solution in PLOT3D format. However, the solution was examined using FAST, "Flow Analysis Software Toolkit", also from NASA. The geometry was also imported into IDEAS through the IGES file written by the package. A solid blade was created and the levels of stress were checked for the purpose of comparing the effect of the specific geometry manipulations on the stress levels.

The geometry perturbations included swept forward and swept backward, with different values of sweep using `sweep_1` and `sweep_2`. The base geometry used was the transonic rotor designed by Sanger [Ref. 7].

### A. SOFTWARE TOOLS

#### 1. TCGRID

The grids were generated using TCGRID (Turbomachinery C-GRID) [Ref. 20]. The code reads the different formats used by NASA (MERIDL, Crouse-Tweedt, or user supplied). The program adds leading- and trailing-edge circles to supplied formats except the general format (user supplied). A meridional grid is generated between hub and tip, onto which the blade geometry is interpolated. The three-dimensional grid is generated from 2-D blade-to-blade grids stacked radially. The grid geometry is written to a file in PLOT3D format.



## 2. RVC3D

RVC3D is a thin-layer Navier-Stokes code with implicit residual smoothing [Ref. 20, 18, 21, 22]. The code can be applied as an Euler solver or with either Baldwin-Lomax or Cebeci-Smith turbulence models. The equations are formulated in cartesian coordinates with rotation then transformed to body-fitted coordinates. The viscous terms are neglected streamwise, but retained in the other directions. The equations are discretized using a Runge-Kutta scheme. The flow field condition is set by specifying the inlet stagnation temperature and pressure, exit hub static pressure and the rotational speed. All other parameters will adjust to satisfy the equations (inlet axial Mach, exit flow angle etc.). The convergence history is printed out and the solution is considered converged when the residuals are reduced three orders of magnitude and the exit total pressure and total temperature remain nearly constant. The solution is written to a PLOT3D-compatible file.

## 3. FAST

FAST was used to examine the solution by displaying different flow field parameters calculated from the "q" vector [Ref. 21]. The program reads in the grid file and the solution file associated with it. The program has various capabilities that include the generation of contour plots of a function, isosurfaces, grid handling and checking, etc.

## 4. IDEAS

IDEAS MASTER SERIES was used to examine the importability of the geometry into a CAD/CAM program and to examine the levels of maximum stress with the different geometry configurations. The program can read the geometry in different formats, manipulate the geometry, and create solids. The stress analysis is carried out within the program using the simulation module in which the mesh is generated. The blade was clamped at the root section and only the stresses due to rotation were examined.



## B. REFERENCE AND SWEEP GEOMETRIES

The selected reference geometry was the Sanger rotor which was designed by Nelson Sanger [Ref. 7] for the Naval Postgraduate School Turbopropulsion Laboratory (TPL). The Sanger stage was a replacement to the transonic compressor designed by Vavra for the TPL research test rig [Ref. 23]. The overall rotor dimensions and maximum rpm were dictated by the test rig. The rotor design parameters are shown in Table III.

Rotor Pressure Ratio	1.61
Tip Speed	$396.2m/sec$ ( $1300ft/sec$ )
Design Weight Flow	$7.75\text{ kg/sec}$ ( $17.09\text{ lb-m/sec}$ )
Tip Inlet Relative Mach Number	1.28
Aspect Ratio	1.2
Hub/Tip Radius Ratio	.51
Number of Blades	22
Tip Solidity	1.3
Tip Diameter	27.94 cm (11.0 in)

Table III. Rotor Design Parameters.

The Sanger rotor was selected as a basis for the implementation of sweep for the following reasons:

1. The rotor was designed using CFD.
2. The rotor was aggressively designed, with high loading.
3. The geometry is accessible and the design process is documented.
4. Test results would be available in the near future for validation purposes.
5. If a successful swept design was obtained, it would be possible to build and test it in the same rig.

The Sanger rotor coordinates were read by the geometry package in MERIDL3 format and fitted with Bezier surfaces. The control points for the Bezier representation are given in Table IV. The leading and trailing edge surface definitions are different from the original blade due to the use of the Bezier representation. While trying to keep the blade chord as close to the original geometry as possible, with minimum changes in the blade surfaces (i.e. subdivision), the leading surface at the hub was found to be blunter than the original blade. While not intended, this did provide an opportunity to examine the effect of leading edge variation on the flow field and performance. To isolate the effect of sweep, the fitted geometry ('base' geometry) will be used as a reference from which to determine the effect of sweep, rather than the original geometry (Sanger geometry). Figures 30 and 31 show the grids for both the Sanger and Base geometries.

The examination of sweep involved several steps, each yielding insight as the geometry package was interfaced with the software tools. First, sweep of 5% in both forward and backward directions was applied to the geometry using sweep\_2. The grids for the two swept geometries and the base geometry were generated using the same parameters used for generating the Sanger rotor grid. The grid generator (TCGRID) was used as supplied without any modification. After examining the overall performance computed using RVC3D at near stall conditions, it was seen that the base geometry suffered a 0.4% drop in energy-averaged efficiency compared to the Sanger geometry. The opposite was expected due to the smoothness conditions imposed on the base geometry by the Bezier package. It was found that the handling of the leading edge in TCGRID was the reason. An example of the grid at the leading edge at mid span is shown in Fig. 32 (The data obtained with this grid are referred to as Data Set 1). The use of TCGRID as supplied was clearly not suitable because the program recomputes the leading edge points according to a user-supplied parameter that controls the spacing of the grid points at the leading edge. That spacing is also varied along the blade span linearly relative to the spacing at

cp	surface 1			surface 2			surface 3		
	x	y	z	x	y	z	x	y	z
0	0.1170	0.0922	0.2700	0.1163	0.0915	0.2699	0.0014	0.0003	0.2236
1	0.1169	0.0918	0.2701	0.0739	0.0693	0.2537	0.0011	3.7e-5	0.2235
2	0.1166	0.0917	0.2700	0.0315	0.0338	0.2398	0.0008	-.0003	0.2233
3	0.1163	0.0915	0.2699	0.0014	0.0003	0.2236	0.0002	0.0002	0.2230
4	0.1073	0.1261	0.3139	0.1075	0.1240	0.3128	0.0055	0.0057	0.3801
5	0.1079	0.1248	0.3129	0.0809	0.0737	0.3054	0.0053	0.0055	0.3815
6	0.1077	0.1244	0.3129	0.0214	0.0300	0.2455	0.0051	0.0052	0.3828
7	0.1075	0.1240	0.3128	0.0055	0.0057	0.3801	0.0043	0.0046	0.3689
8	0.0891	0.1477	0.3888	0.0898	0.1453	0.3831	0.0155	0.0067	0.4038
9	0.0901	0.1461	0.3834	0.0694	0.0963	0.3591	0.0152	0.0061	0.4035
10	0.0900	0.1457	0.3832	0.0463	0.0668	0.4362	0.0148	0.0055	0.4032
11	0.0898	0.1453	0.3831	0.0155	0.0067	0.4038	0.0144	0.0058	0.4062
12	0.0886	0.1593	0.4274	0.0885	0.1583	0.4278	0.0157	0.0114	0.4555
13	0.0889	0.1591	0.4275	0.0641	0.1063	0.4468	0.0155	0.0110	0.4555
14	0.0887	0.1587	0.4276	0.0369	0.0574	0.4544	0.0152	0.0105	0.4555
15	0.0885	0.1583	0.4278	0.0157	0.0114	0.4555	0.0149	0.0106	0.4555
	surface 4			surface 5			surface 6		
	x	y	z	x	y	z	x	y	z
0	0.0002	0.0002	0.2230	0.0001	0.0016	0.2229	0.1162	0.0923	0.2695
1	-.0003	0.0008	0.2226	0.0269	0.0413	0.2371	0.1166	0.0924	0.2697
2	-.0001	0.0012	0.2228	0.0551	0.0786	0.2398	0.1171	0.0925	0.2700
3	0.0001	0.0016	0.2229	0.1162	0.0923	0.2695	0.1170	0.0922	0.2700
4	0.0043	0.0046	0.3689	0.0038	0.0046	0.352	0.10613	0.1266	0.3150
5	0.0034	0.0039	0.3549	0.0228	0.0363	0.2075	0.1064	0.1270	0.3150
6	0.0036	0.0042	0.3534	0.0612	0.0783	0.3170	0.1068	0.1273	0.3150
7	0.0038	0.0046	0.352	0.1061	0.1266	0.3150	0.1073	0.1261	0.3139
8	0.0144	0.0058	0.4062	0.0146	0.0075	0.4105	0.0877	0.1486	0.3935
9	0.0140	0.0062	0.4093	0.0441	0.0688	0.4690	0.0879	0.1490	0.3939
10	0.0143	0.0068	0.4099	0.0555	0.0949	0.345	0.0882	0.1494	0.3942
11	0.0146	0.0075	0.4105	0.0877	0.1486	0.3935	0.0891	0.1477	0.3888
12	0.0149	0.0106	0.4555	0.0152	0.0120	0.4555	0.0879	0.1592	0.4274
13	0.0146	0.0107	0.4555	0.0435	0.0787	0.4544	0.0881	0.1594	0.4274
14	0.0149	0.0114	0.4555	0.0676	0.1373	0.4358	0.0882	0.1596	0.4273
15	0.0152	0.0120	0.4555	0.0879	0.1592	0.4274	0.0886	0.1593	0.4274

Table IV. Bezier Representation of Sanger Rotor [Base Geometry].



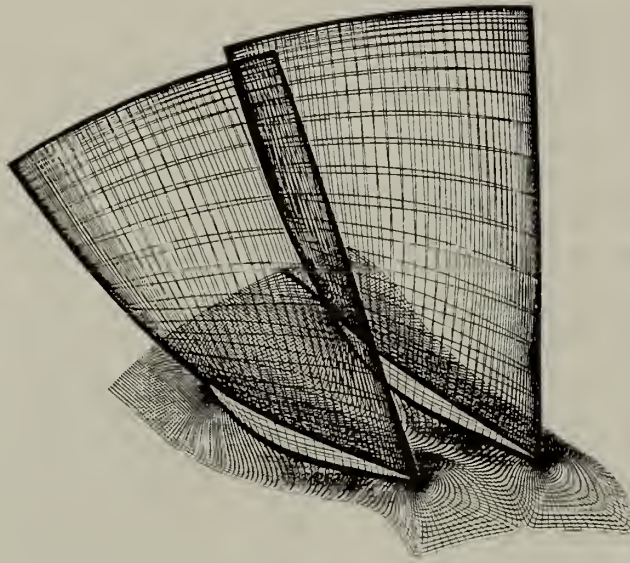


Figure 30. Grid for Sanger Blade Row

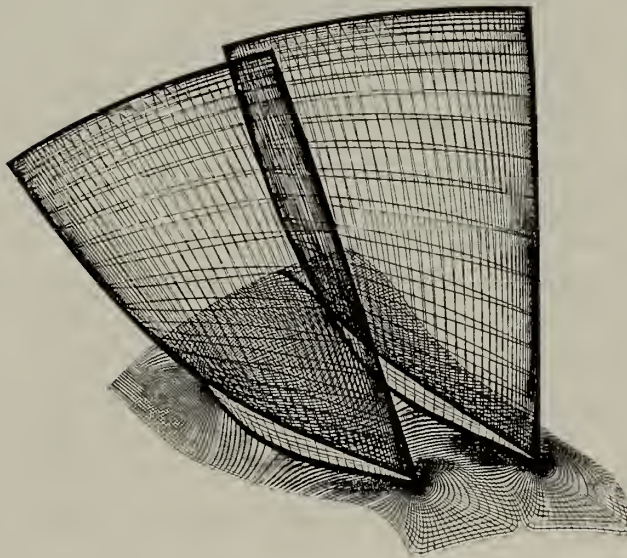


Figure 31. Grid for Fitted (Base) Blade Row

the hub by another specified parameter. While changing these parameters could have improved the leading edge grid spacing at some locations radially, it was an undesirable approach due to the shape change that accompanies the gridding process, and the lack of control over the other radial stations. Therefore the program was changed to compute internally the grid spacing parameter at each station, while neglecting the user-supplied parameters.

The grid then obtained at the mid-span leading edge is shown in Fig. 33, and the results obtained with the grid are referred to as Data Set 2. Four cases of sweep were examined in addition to the base geometry and the Sanger geometry, all at near design conditions. The four cases were swept with 10% tip chord movement along the chord direction using sweep\_1 and sweep\_2 in both forward and backward directions. Figures 34, 35, 36 and 37 show the grids generated for the swept blade rows. After computing the flow field, the base geometry was still showing lower performance. It was not clear at first that the effect was again due to the grid, since it appeared that the leading edge bluntness was causing an over-expansion and creating a stronger shock. Being unable to explain the increase in relative Mach number with reduced mass flow rate, the grid at the leading edge was magnified and was found to be relatively coarse. This was due to the use of the same number of grid points over the leading edge while having a leading edge of longer arc length. The problem was overcome by increasing the number of 'leading edge' points supplied to TCGRID and decreasing the number of surface points by the same amount. That caused TCGRID to consider a portion of the leading edge as a part of the blade surface, giving better leading-edge resolution. The final grid is illustrated for the mid-span section in Fig. 38 and the data obtained with this grid are referred to as Data Set 3.

Data Set 3 is discussed in the most detail but Data Set 2 is also reported (Appendix C) because there are lessons to be learned from the results, and because they show that some of the trends determined for the effects of sweep were not grid dependent.

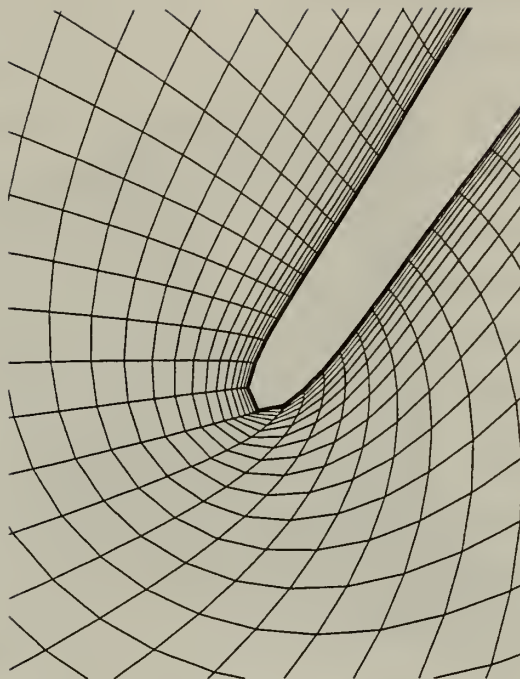


Figure 32. Grid for Data Set 1.

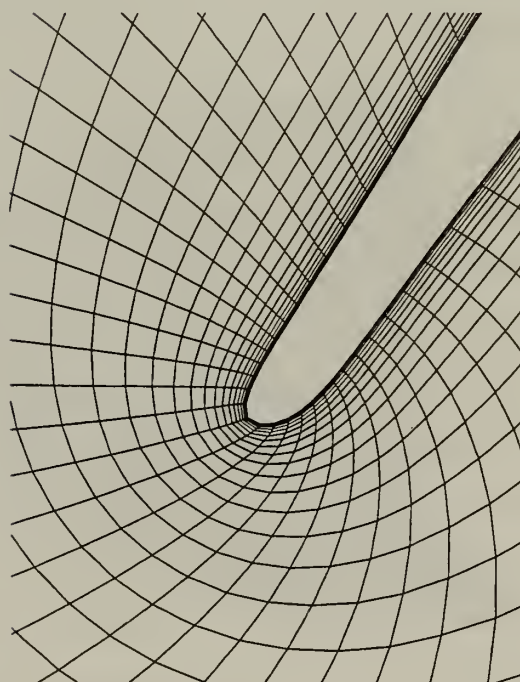


Figure 33. Grid for Date Set 2.



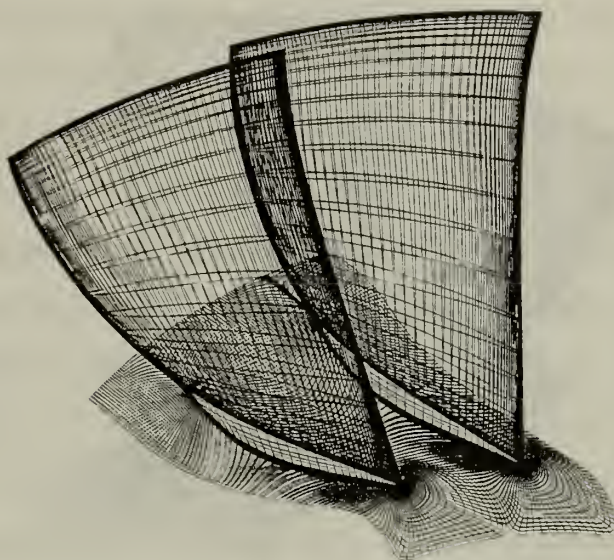


Figure 34. Swept Forward +10% Using Sweep\_1

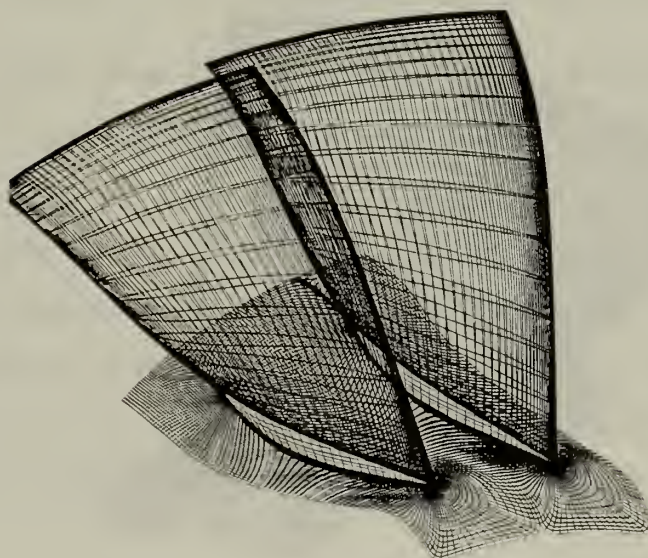


Figure 35. Swept Back -10% Using Sweep\_1

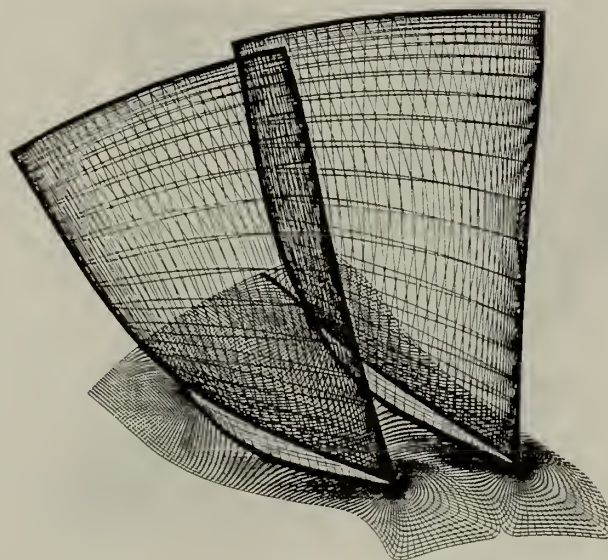


Figure 36. Swept Forward +10% Using Sweep\_2

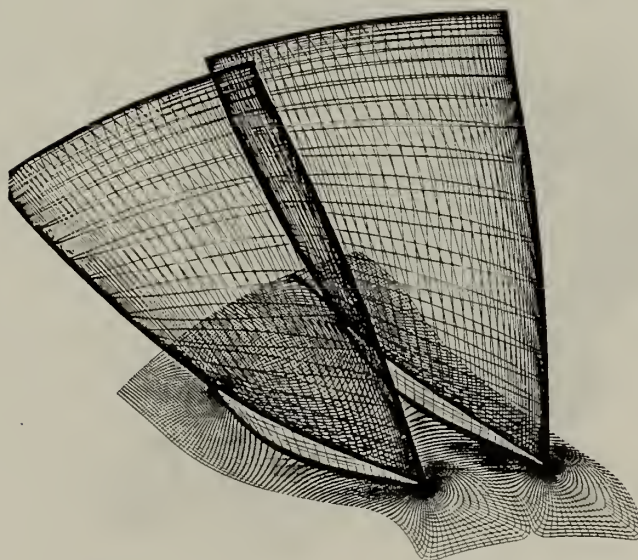


Figure 37. Swept Back -10% Using Sweep\_2

## C. RESULTS OF FLOW ANALYSIS

### 1. Overall Performance

The test cases were examined numerically using RVC3D. The overall 'energy-averaged' performance obtained for the different geometries and leading edge grids is summarized in Table V. The exit-static to inlet-total pressure ratio and rotational speed for Data Sets 2 and 3 were the same as the design point for the Sanger rotor. Data Set 1 was obtained with an exit-static pressure to inlet-total pressure ratio that is different from cases 2 and 3. All solutions were obtained at 3000 iterations. The RMS density residuals were down to the same level. All cases achieved a reduction of over three orders of magnitude. The convergence history is shown in Figure 39 for Data Set 3. The back-swept rotor was observed to have the highest efficiency in all cases, and to pump a higher mass flow rate. The forward-swept rotor had the lowest efficiency, and pumped the lowest flow rate. The Sanger geometry performed better than the fitted (base) geometry in Data Set 1 and 2, and the effect of backward sweep was to recover that performance. For Data Set 3 the opposite was true and the fitted geometry performed slightly better than the Sanger geometry. The effect of sweep on performance for Data Set 3 may be deduced from an examination of the flow field.

### 2. Exit Flow Field (Peripherally-Averaged)

The radial distribution of circumferentially energy-averaged efficiency is shown for Data Set 3 in Fig. 40. The forward-swept geometry is seen to have lower efficiency over the blade span than the base geometry, the Sanger geometry and the swept-back geometry. The swept-back geometry showed higher efficiency compared to the base geometry. The swept-back rotor efficiency was high from hub to 50% span, and near the tip. The efficiency for the base geometry was insignificantly lower than the Sanger geometry over a large portion of the blade span, but slightly higher over the outer 20%.

Figures 41 - 44 show the radial distributions of exit total pressure to reference pressure, exit static pressure to reference pressure, exit total temperature to reference

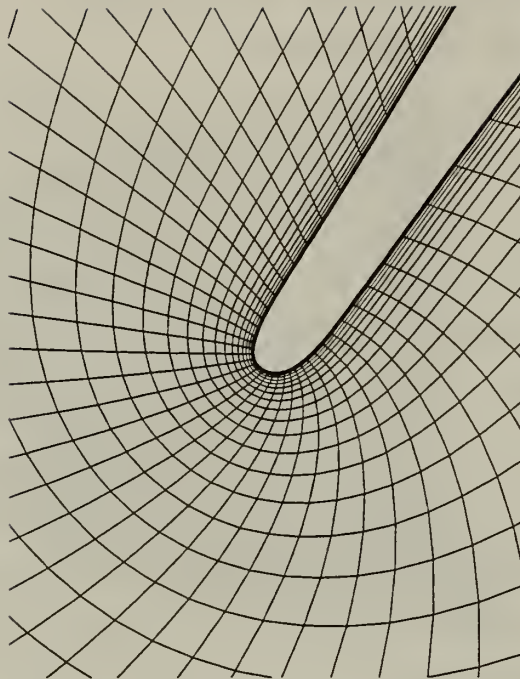


Figure 38. Grid for Data Set 3.

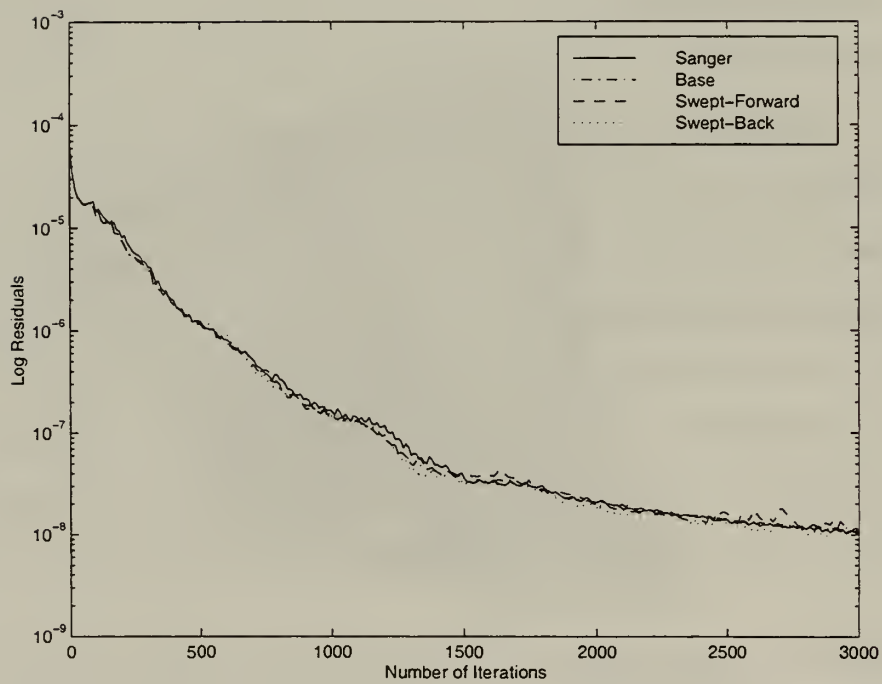


Figure 39. Convergence History for Data Set 3.



Case	Mass Flow kgsec	Efficiency	Total Pressure Ratio	Total Temperature Ratio
Data Set 1				
Sanger	7.381	.91182	1.64213	1.16697
Base	7.321	.90772	1.64262	1.16783
Swept-forward 5%	7.236	.90235	1.64289	1.16889
Swept-back 5%	7.372	.91166	1.64201	1.16697
Data Set 2				
Sanger	7.704	.92211	1.60087	1.15605
Base	7.669	.92047	1.60017	1.15618
Swept-Forward 1	7.601	.91714	1.59990	1.15668
Swept-Forward 2	7.593	.91473	1.60000	1.15712
Swept-Back 1	7.695	.92104	1.59961	1.15596
Swept-Back 2	7.695	.92247	1.59911	1.15560
Data Set 3				
Sanger	7.704	.92211	1.60087	1.15605
Base	7.695	.92332	1.60011	1.1557
Swept-forward	7.619	.91785	1.59994	1.15657
Swept-back	7.721	.9254	1.59853	1.15498

Table V. Overall Performance Results.

temperature and exit static temperature to reference temperature, respectively. The total pressure for the swept-forward rotor at the hub is seen to be higher than the swept-back rotor. That difference is reduced gradually to zero at about 25% of span, staying small to nearly 80% of span, and then reversing in direction. The static pressure is higher for the swept-forward and lower for the swept-back compared to the base. The total temperature for the swept-forward rotor is higher at the hub than for the swept-back rotor. At the tip there is no significant difference between the energy added by the different rotors.

Figures 45 - 48 show exit Mach number, meridional flow angle  $\phi(\arctan(\frac{v_r}{u}))$ , total velocity to reference (sonic speed) and swirl angle  $\alpha(\arctan(\frac{v_\theta}{u}))$  where  $u$  is the axial velocity. The velocity was nearly identical for the four rotors. There is seen to be a slight change in the exit flow angles between the rotors near the tip.

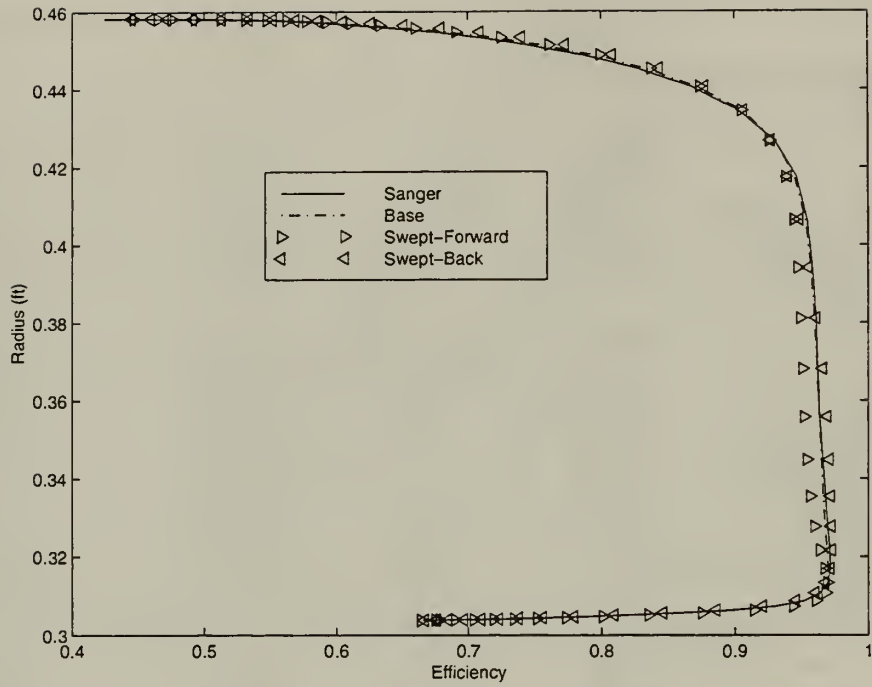


Figure 40. Radial Distribution of the Circumferentially Energy-Averaged Efficiency.

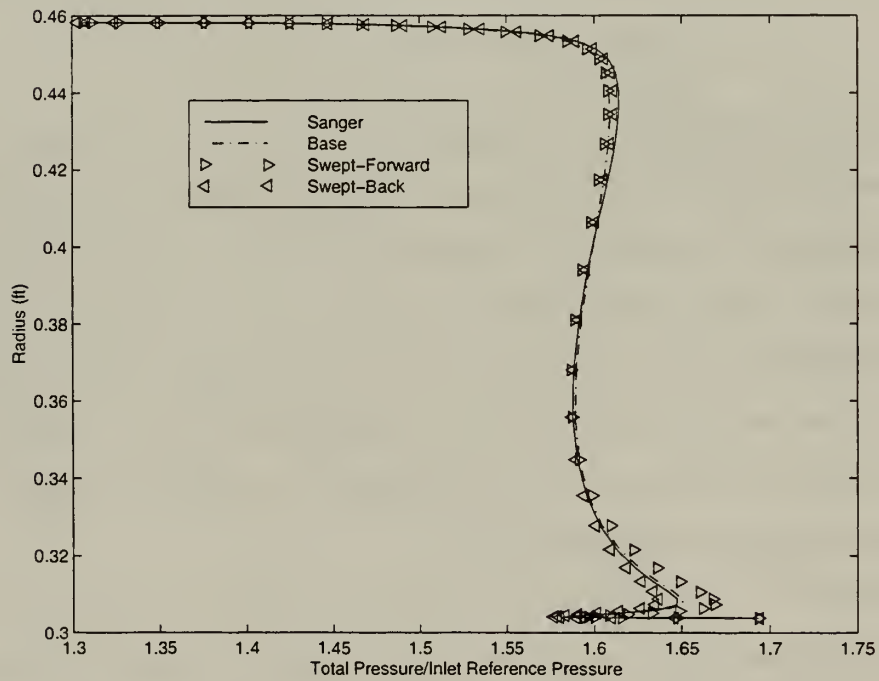


Figure 41. Radial Distribution of the Circumferentially Energy-Averaged Total-to-Reference Pressure.



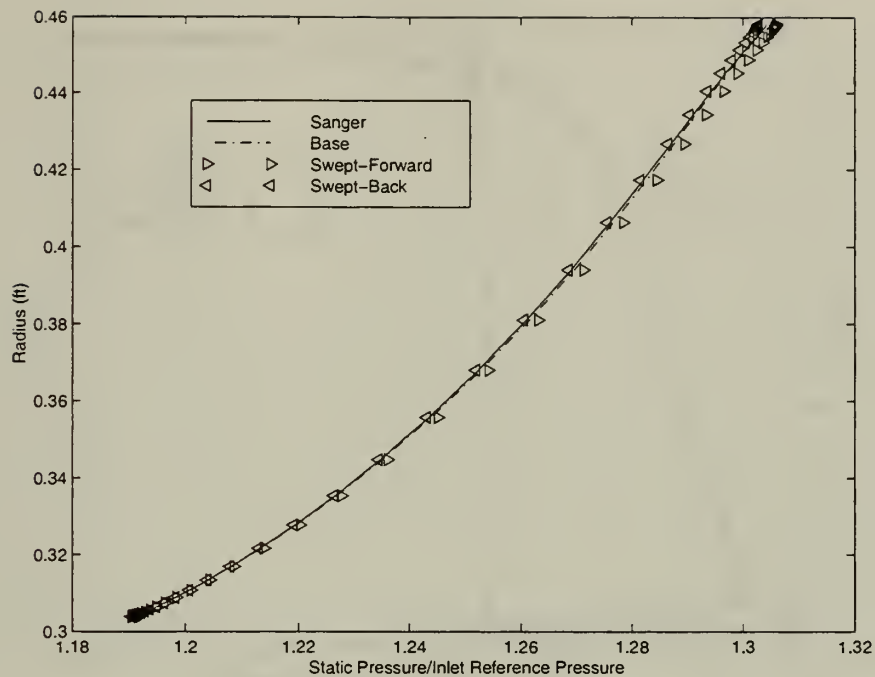


Figure 42. Radial Distribution of the Circumferentially Energy-Averaged Static-to-Reference Pressure.

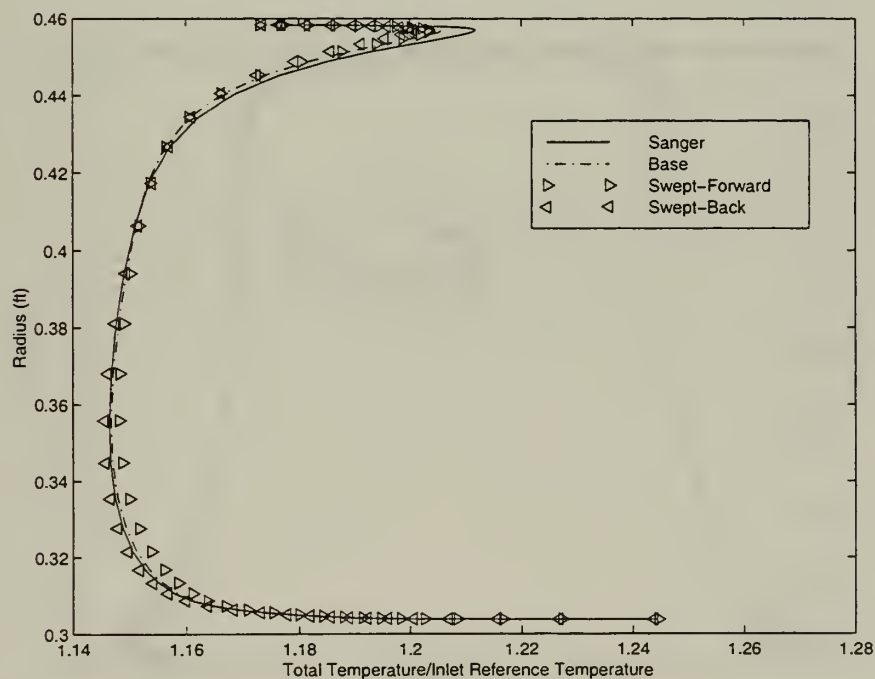


Figure 43. Radial Distribution of the Circumferentially Energy-Averaged Total-to-Reference Temperature.

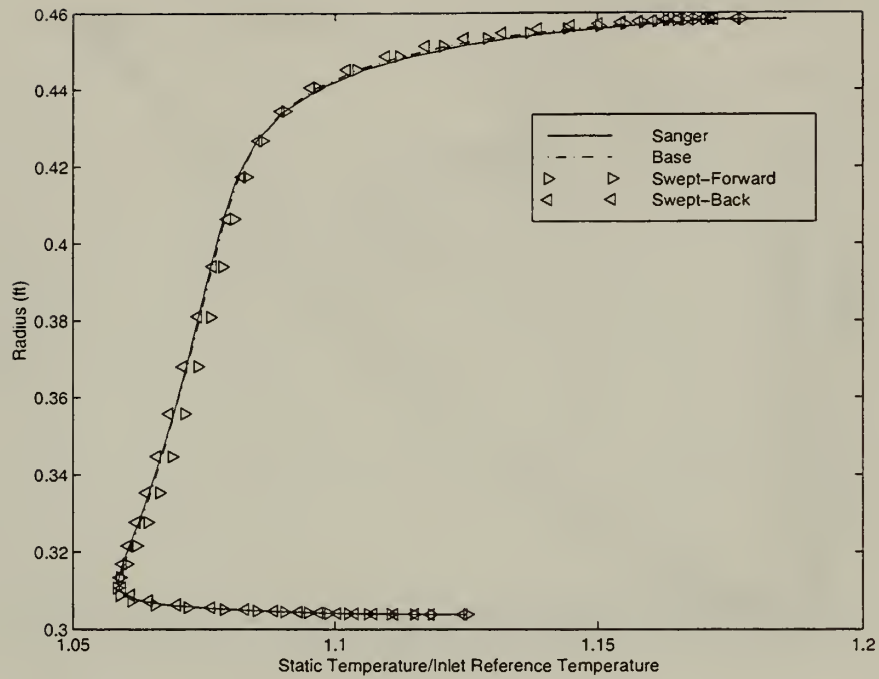


Figure 44. Radial Distribution of the Circumferentially Energy-Averaged Static-to-Reference Temperature.

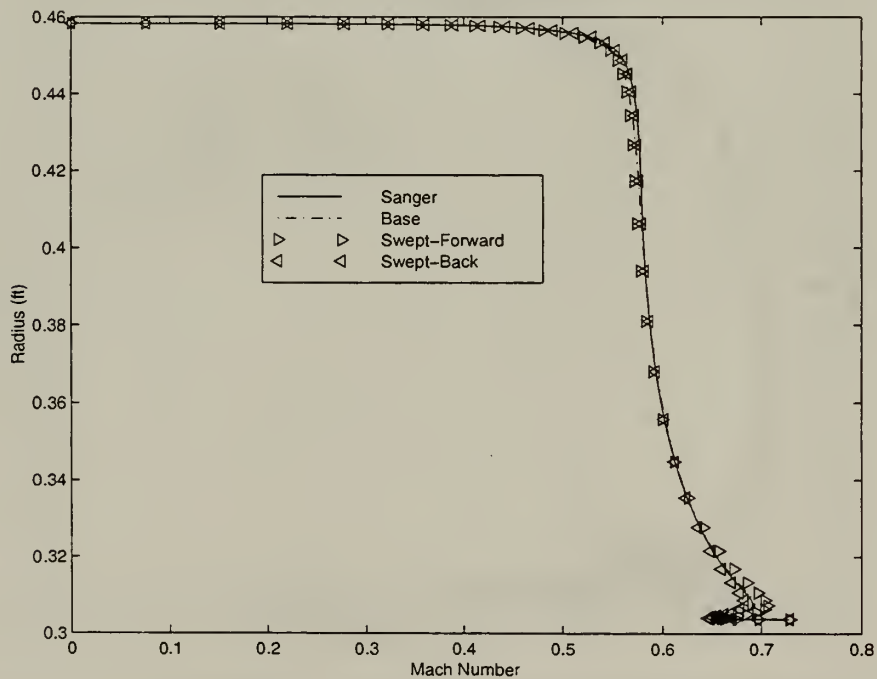


Figure 45. Radial Distribution of the Mach Number.

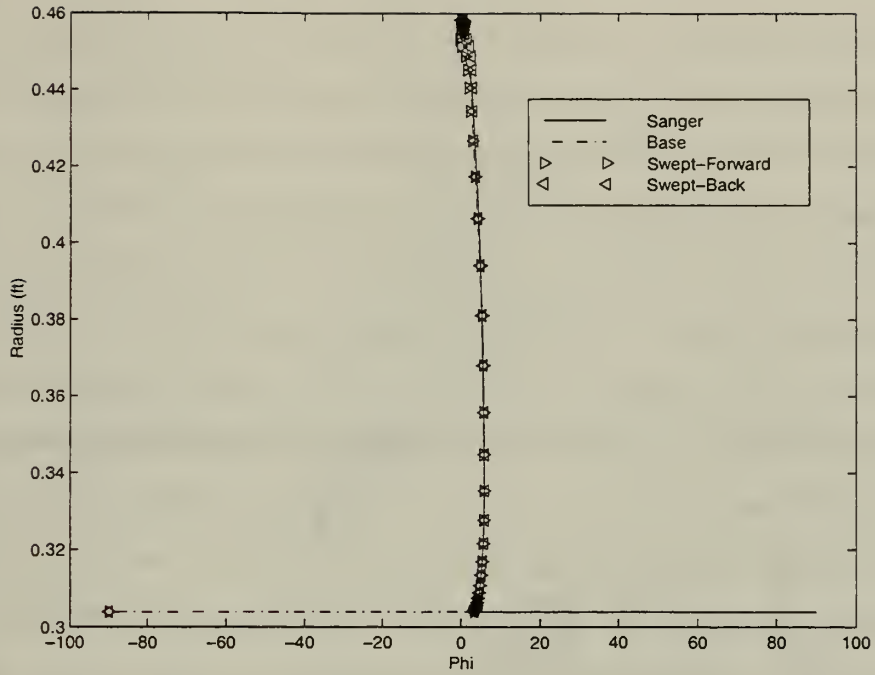


Figure 46. Radial Distribution of the Flow Angle ( $\phi$ ) in the Meridional Plane.

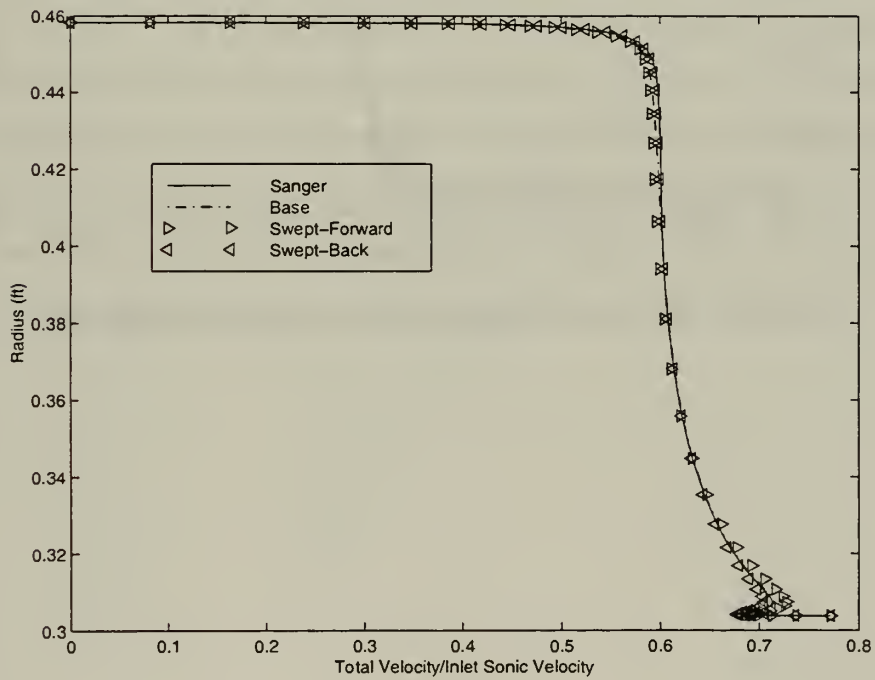


Figure 47. Radial Distribution of the Total Velocity to Reference Sonic Velocity.

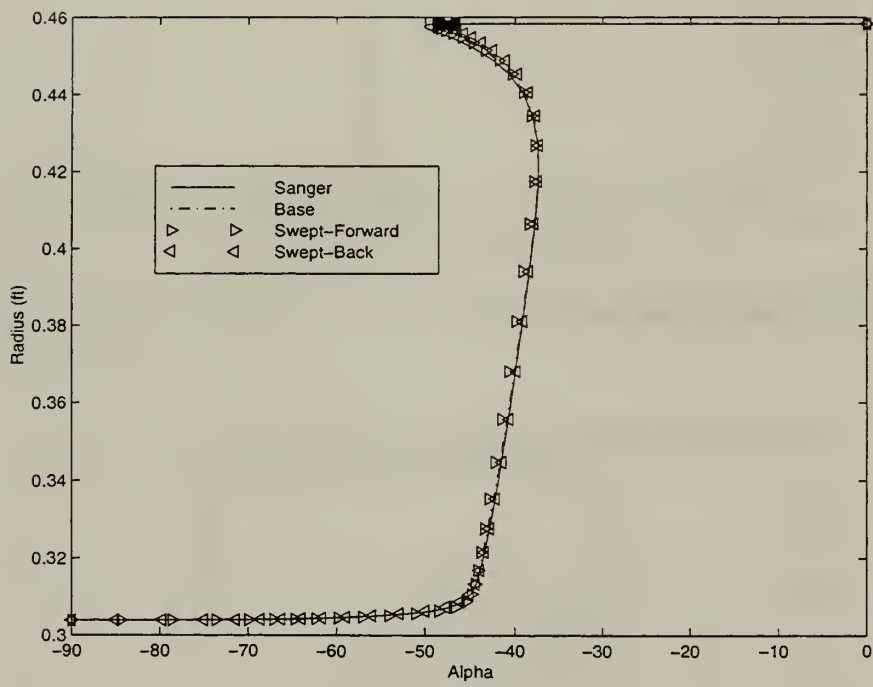


Figure 48. Radial Distribution of the Swirl Angle ( $\alpha$ ).

### 3. Blade Passage Flow Field

In the following discussion, only the results from Data Set 3 are included. Results from Data Set 2 are given in Appendix C however, and based on the overall performance and the peripherally-averaged rotor exit profiles, there was consistency observed in the effect of sweeping the base geometry either forward or backward.

The flow field computed for the Sanger rotor at design point (Data Set 3) is shown in Fig. 49 - 54. The Sanger rotor Mach number contour plots show that there is a mild shock wave at about  $M = 1.2$  at the tip section. The lower half of the blade from hub to 50% span has subsonic flow, except for the small region around the leading edge. The boundary layer over the suction surface remains relatively thin in the flow direction over most of the blade span. Over the outer 10% of the span the boundary layer thickens progressively toward the tip. That boundary layer growth is affected by the occurrence of the passage shock which started at 75% of span. Also, the blade wake at the trailing edge is thicker toward the tip.

The flow field for the base geometry is compared with the flow field for the Sanger rotor in Fig. 55 - 60 (Data Set 3). The plots are composite, showing the Mach number variation across the blade channels for the two blades side-by-side, with the base geometry blade above the Sanger blade. The flow field for the base geometry was slightly affected by the leading edge shape. A slight over-expansion over the leading edge occurred due to the leading edge geometry. The boundary layer thickness was relatively thinner than the Sanger rotor and the wake width was smaller.





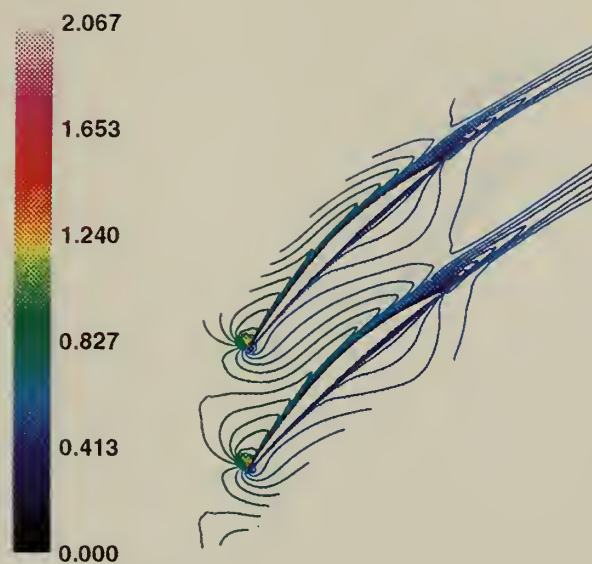


Figure 49. Mach Number in the Blade Passage of the Sanger Rotor at 10% Span.

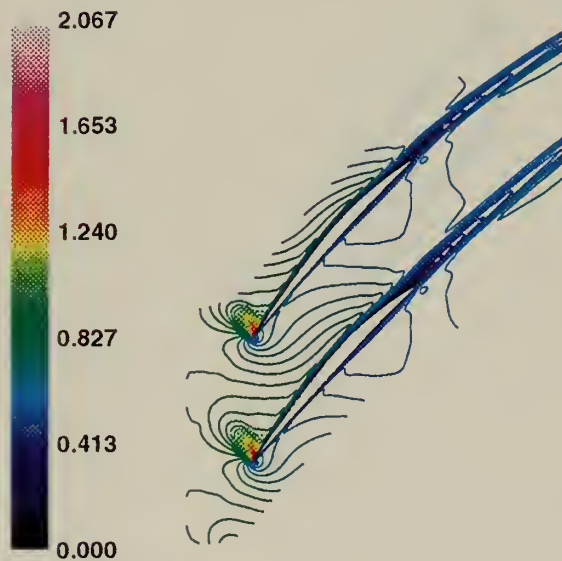


Figure 50. Mach Number in the Blade Passage of the Sanger Rotor at 25% Span.



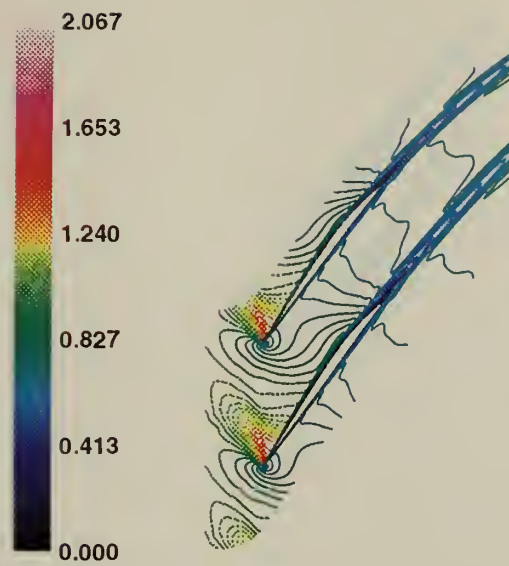


Figure 51. Mach Number in the Blade Passage of the Sanger Rotor at 50% Span.

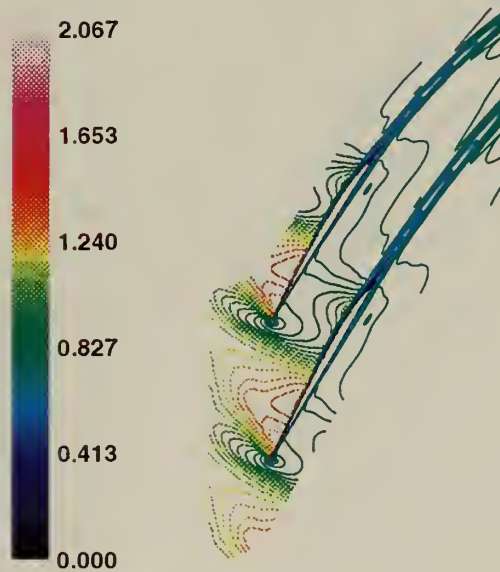


Figure 52. Mach Number in the Blade Passage of the Sanger Rotor at 75% Span.



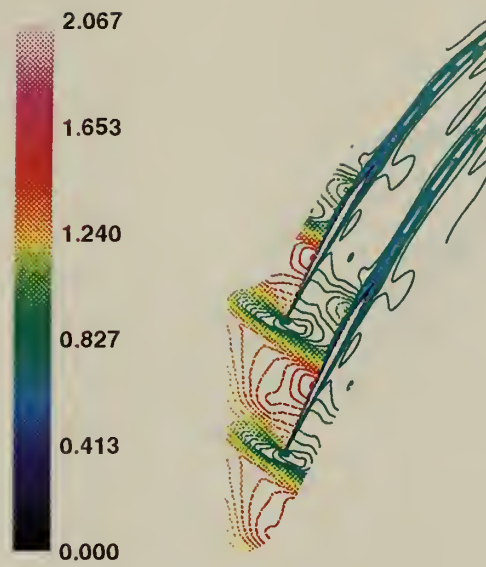


Figure 53. Mach Number in the Blade Passage of the Sanger Rotor at 90% Span.

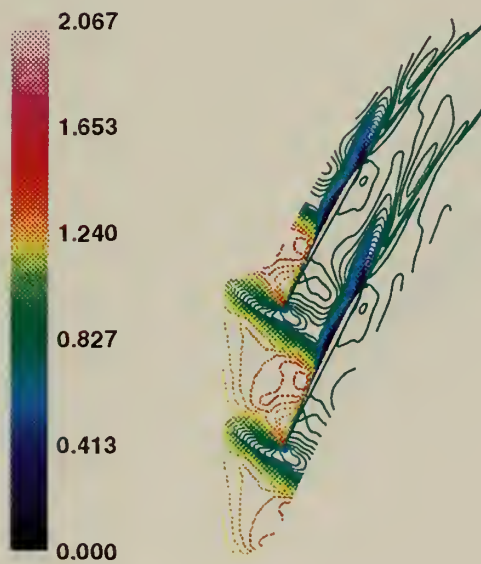


Figure 54. Mach Number in the Blade Passage of the Sanger Rotor in the Case Wall Boundary Layer.





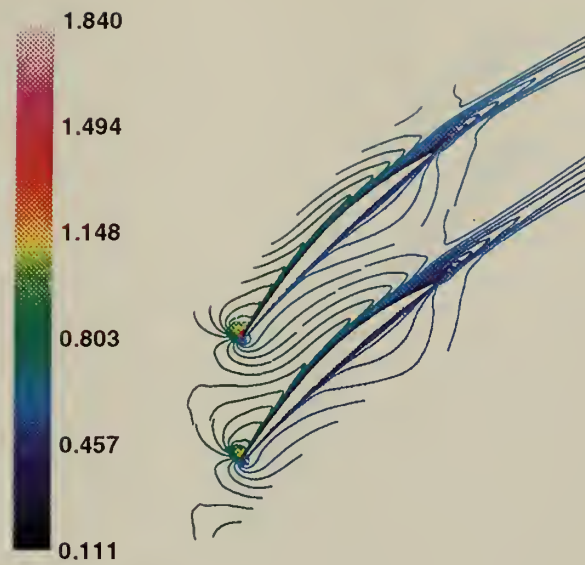


Figure 55. Mach Number in the Blade Passage of the Sanger Rotor (Lower Blade) and Base Rotor (Upper Blade) at 10% Span.

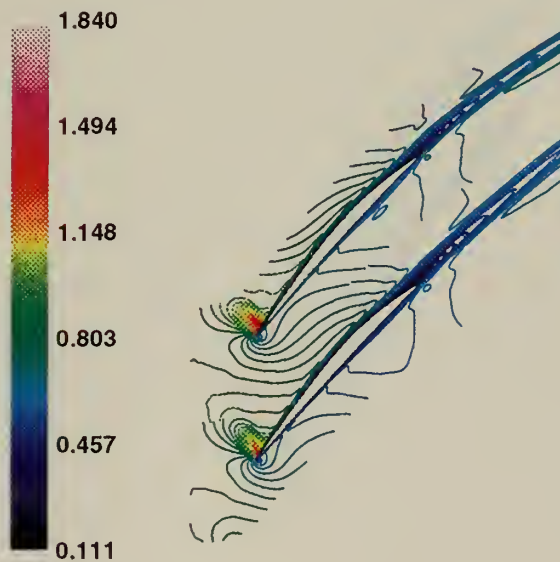


Figure 56. Mach Number in the Blade Passage of the Sanger Rotor (Lower Blade) and Base Rotor (Upper Blade) at 25% Span.



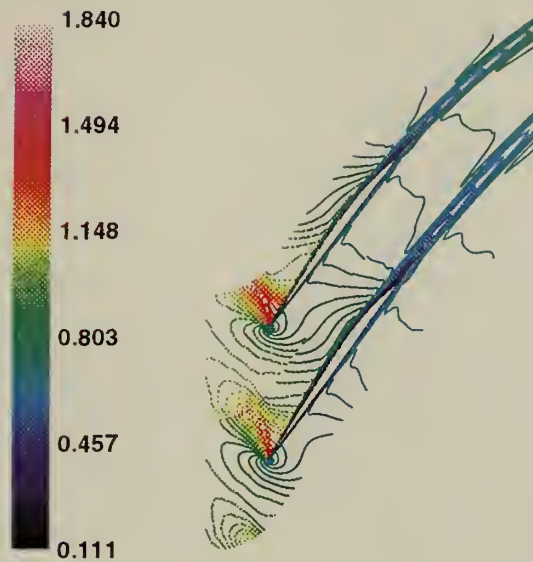


Figure 57. Mach Number in the Blade Passage of the Sanger Rotor (Lower Blade) and Base Rotor (Upper Blade) at 50% Span.

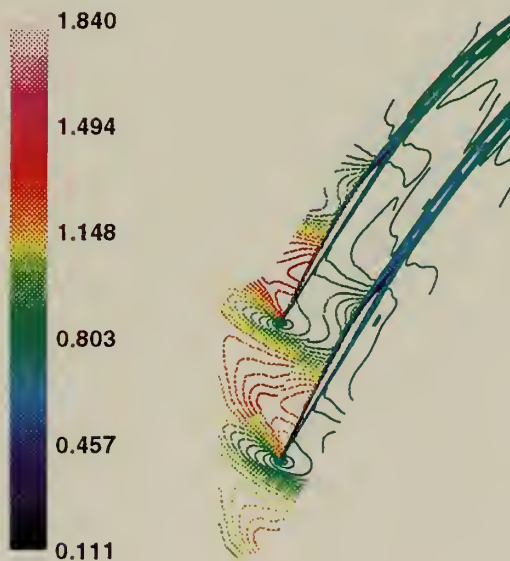


Figure 58. Mach Number in the Blade Passage of the Sanger Rotor (Lower Blade) and Base Rotor (Upper Blade) at 75% Span.



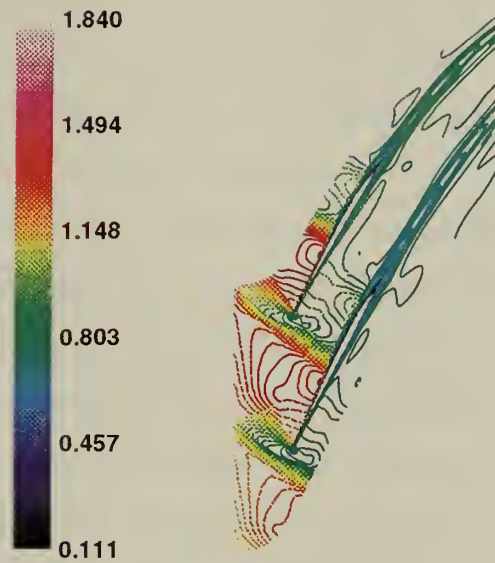


Figure 59. Mach Number in the Blade Passage of the Sanger Rotor (Lower Blade) and Base Rotor (Upper Blade) at 90% Span.

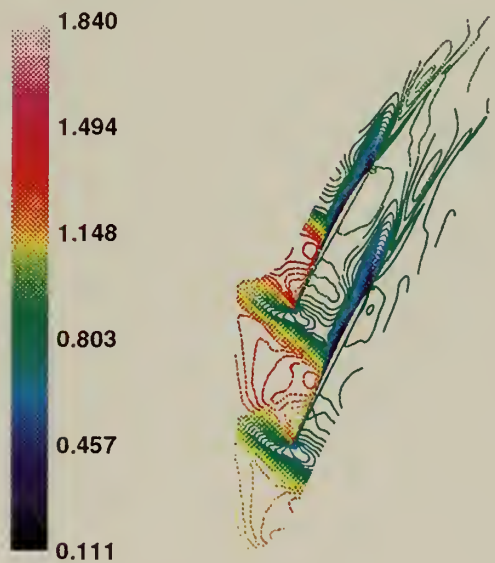


Figure 60. Mach Number in the Blade Passage of the Sanger Rotor (Lower Blade) and Base Rotor (Upper Blade) in the Case Wall Boundary Layer.





Similar composite contour plots of Mach number are shown for the base geometry and swept-forward rotor in Fig. 61 - 66, and for the base geometry and swept-back rotor in Fig. 67 - 72. In general, the shock location appears to move forward with respect to the leading edge in the swept-forward rotor, and backward with respect to the leading edge in the swept-back rotor.

Figure 73 shows the suction surface pressure and Fig. 78 shows the velocity vectors at the third grid point away from the suction surface for the swept-back blade. Corresponding plots are given in Figs. 75 and 74 for the base geometry, and in Figs. 77 and 76 for the swept-forward blade. Examination shows that the location of the shock with respect to the blade leading edge at the tip section is moved very little. However, the structure of the shock over the blade surface is clearly changed. The forward sweep results in a single, continuous shock wave. The backward sweep results in two separate shocks.

The secondary flow created by the shock structure can be seen in the velocity vector plots. The radial motion is seen to be largest in the swept-forward rotor and least in the swept-back rotor.



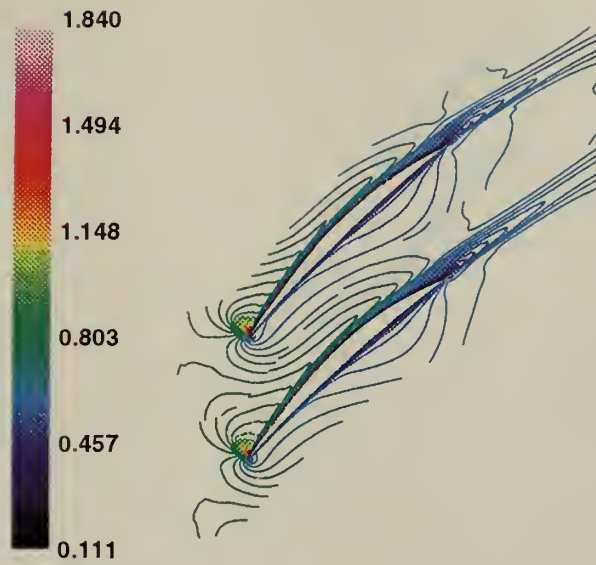


Figure 61. Mach Number in the Blade Passage of the Base Rotor (Lower Blade) and Swept-Forward Rotor (Upper Blade) at 10% Span.

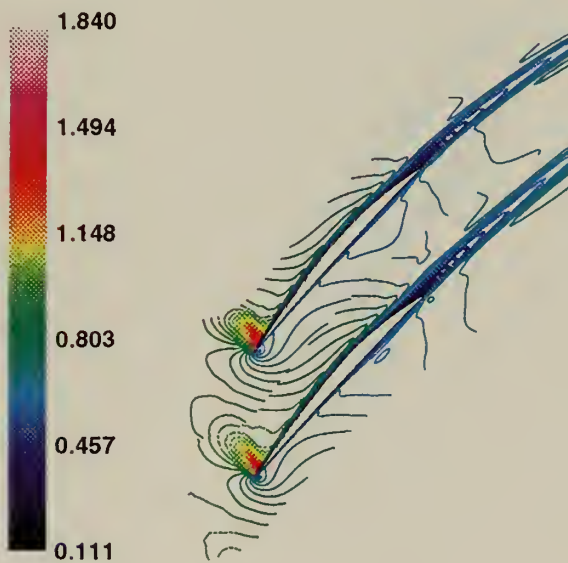


Figure 62. Mach Number in the Blade Passage of the Base Rotor (Lower Blade) and Swept-Forward Rotor (Upper Blade) at 25% Span.



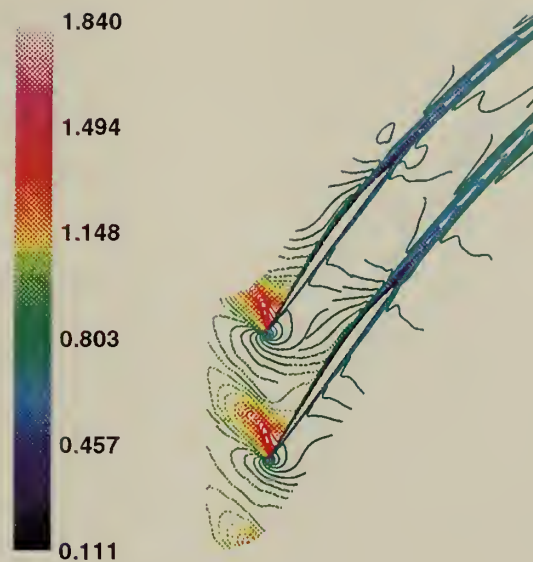


Figure 63. Mach Number in the Blade Passage of the Base Rotor (Lower Blade) and Swept-Forward Rotor (Upper Blade) at 50% Span.

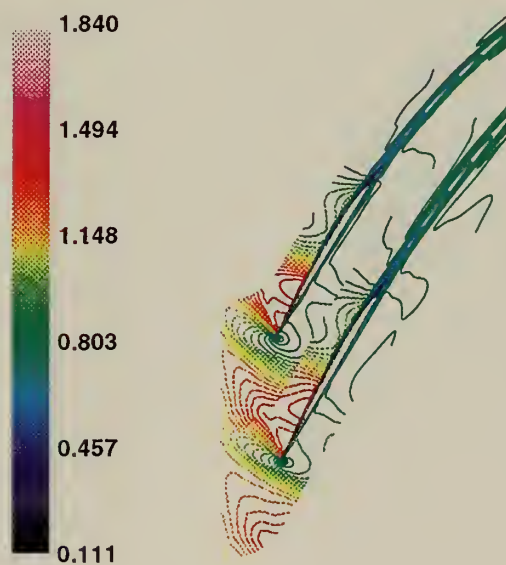


Figure 64. Mach Number in the Blade Passage of the Base Rotor (Lower Blade) and Swept-Forward Rotor (Upper Blade) at 75% Span.





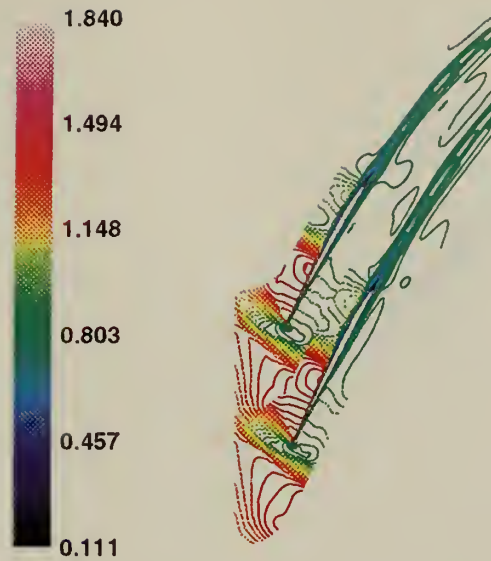


Figure 65. Mach Number in the Blade Passage of the Base Rotor (Lower Blade) and Swept-Forward Rotor (Upper Blade) at 90% Span.

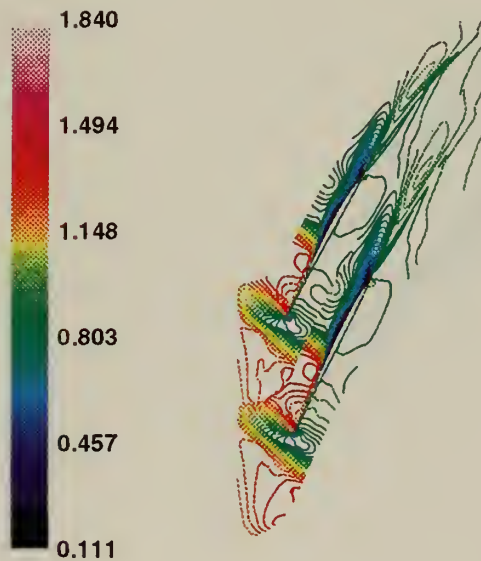


Figure 66. Mach Number in the Blade Passage of the Base Rotor (Lower Blade) and Swept-Forward Rotor (Upper Blade) in the Case Wall Boundary Layer.



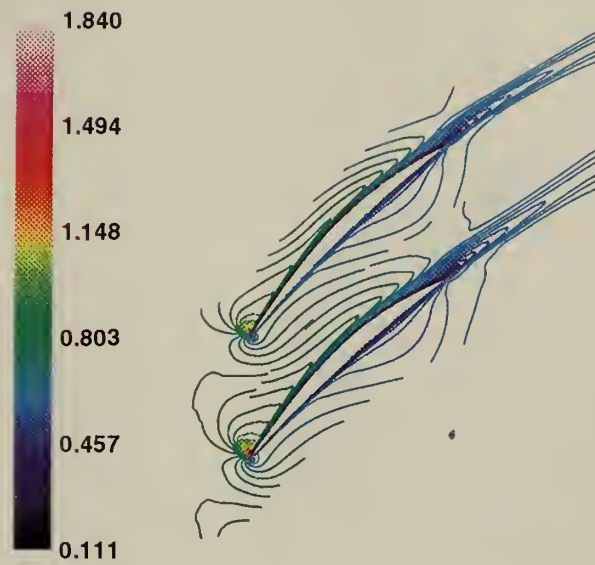


Figure 67. Mach Number in the Blade Passage of the Base Rotor (Lower Blade) and Swept-Back Rotor (Upper Blade) at 10% Span.

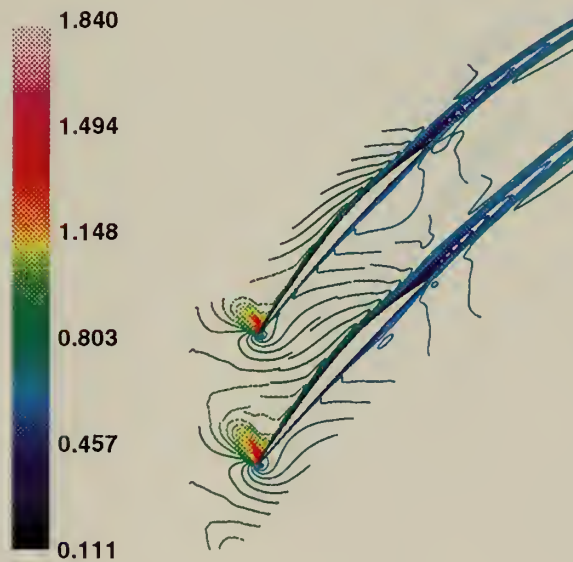


Figure 68. Mach Number in the Blade Passage of the Base Rotor (Lower Blade) and Swept-Back Rotor (Upper Blade) at 25% Span.



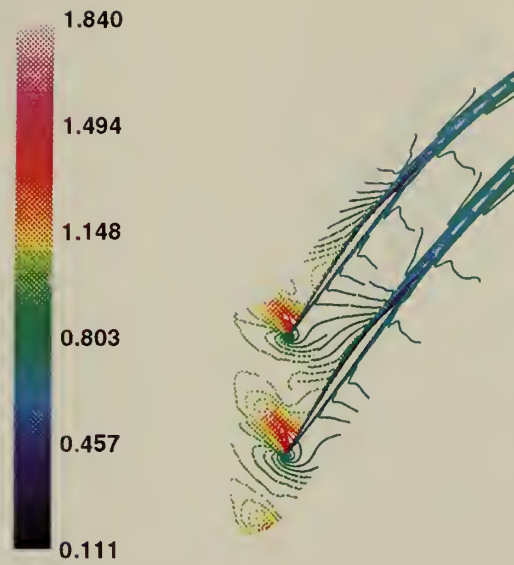


Figure 69. Mach Number in the Blade Passage of the Base Rotor (Lower Blade) and Swept-Back Rotor (Upper Blade) at 50% Span.

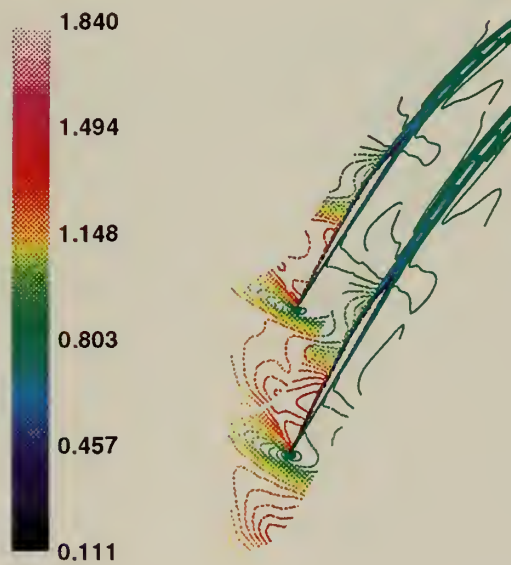


Figure 70. Mach Number in the Blade Passage of the Base Rotor (Lower Blade) and Swept-Back Rotor (Upper Blade) at 75% Span.





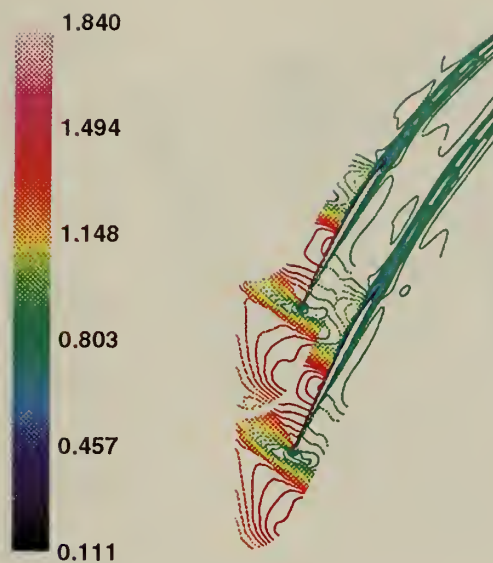


Figure 71. Mach Number in the Blade Passage of the Base Rotor (Lower Blade) and Swept-Back Rotor (Upper Blade) at 90% Span.

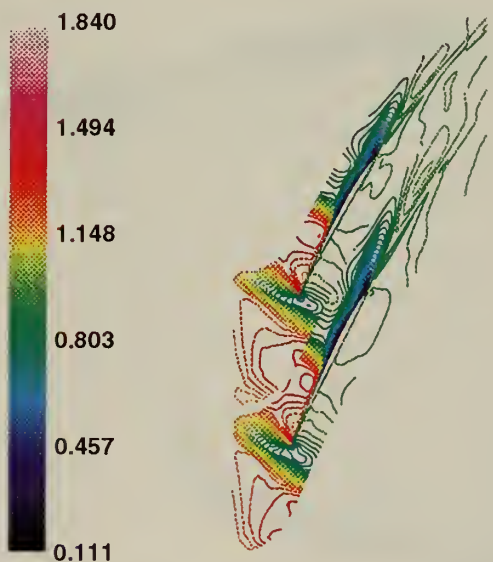


Figure 72. Mach Number in the Blade Passage of the Base Rotor (Lower Blade) and Swept-Back Rotor (Upper Blade) in the Case Wall Boundary Layer.



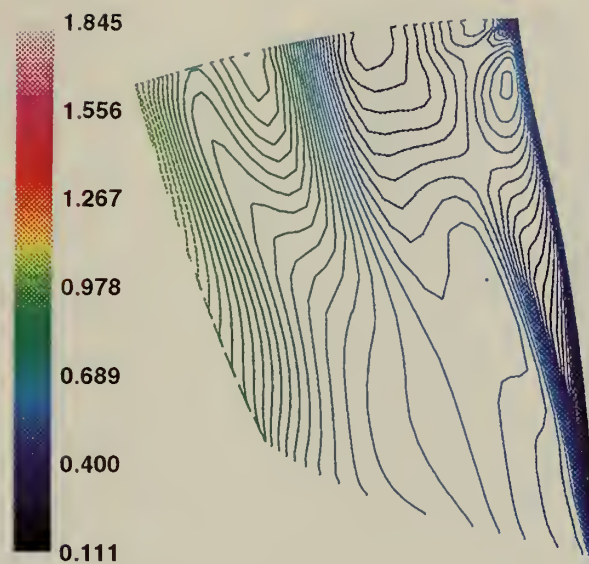


Figure 73. Pressure on the Suction Surface of the Swept-Back Rotor Blade.

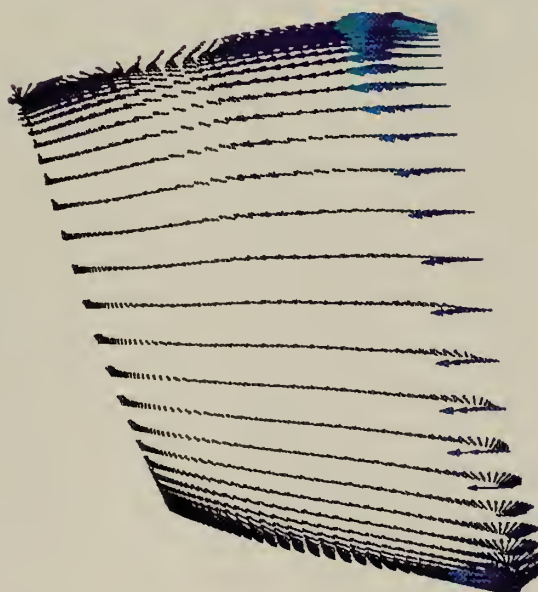


Figure 74. Velocity Vector Near Suction Surface (3<sup>rd</sup> Grid Point) of the Swept-Back Rotor Blade.



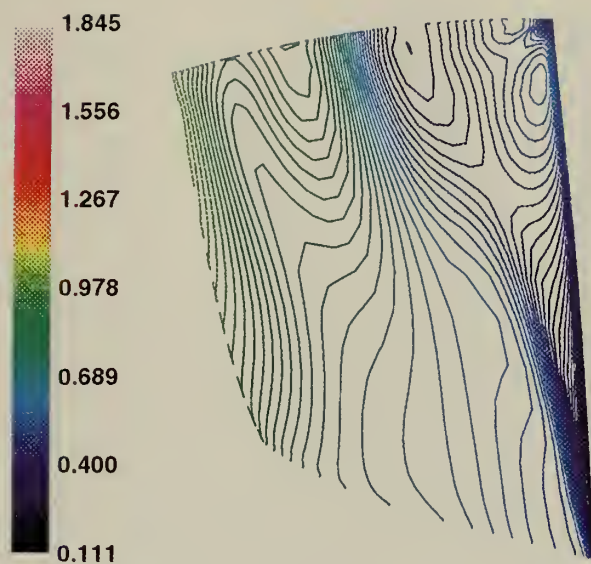


Figure 75. Pressure on the Suction Surface of the Base Rotor Blade.

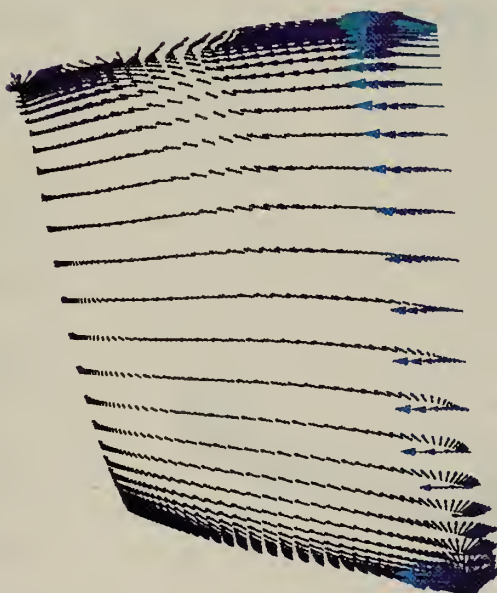


Figure 76. Velocity Vector Near Suction Surface (3<sup>rd</sup> Grid Point) of the Base Rotor Blade.





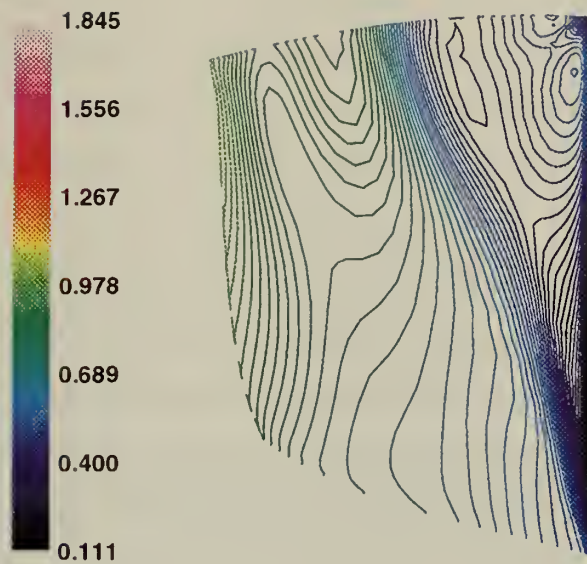


Figure 77. Pressure on the Suction Surface of the Swept-Forward Rotor Blade.

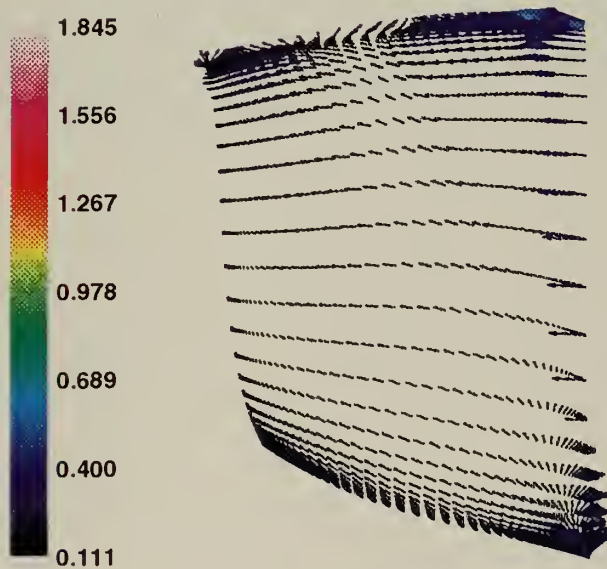


Figure 78. Velocity Vector Near Suction Surface ( $3^{rd}$  Grid Point) of the Swept-Forward Blade.



## D. RESULTS OF STRESS ANALYSIS

The stress analysis for the three geometries in Data Set 3 were carried out using IDEAS. The geometry surfaces were transformed to a solid for the the creation of the finite element model. The stresses were calculated due to centrifugal loads at a rotational speed of 30,000 rpm. The design speed is 27,000 rpm. The swept-forward rotor showed an increase in the stress levels on the pressure side to 47,400 psi from a stress level of 34,400 psi for the base rotor. The swept-backward rotor showed a stress level of 41,700 psi on the suction side. The stress level should be increased for the base rotor and swept-forward rotor when the aerodynamic loads are added. For the swept-back rotor the stress levels will be reduced due to the aerodynamic load. The following figures show the calculated stress levels for the three rotors.



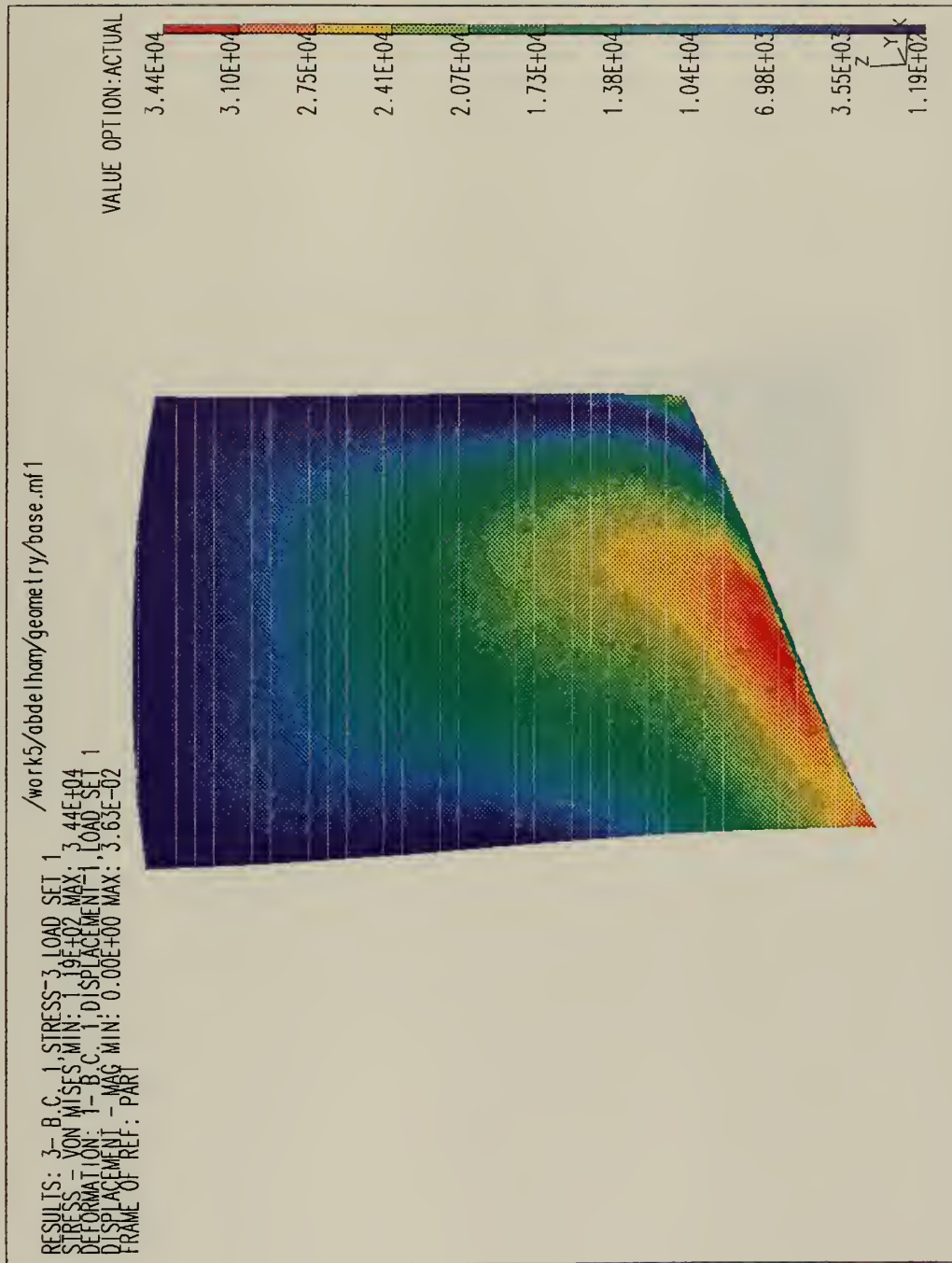


Figure 79. Stress Levels for the Base Rotor.





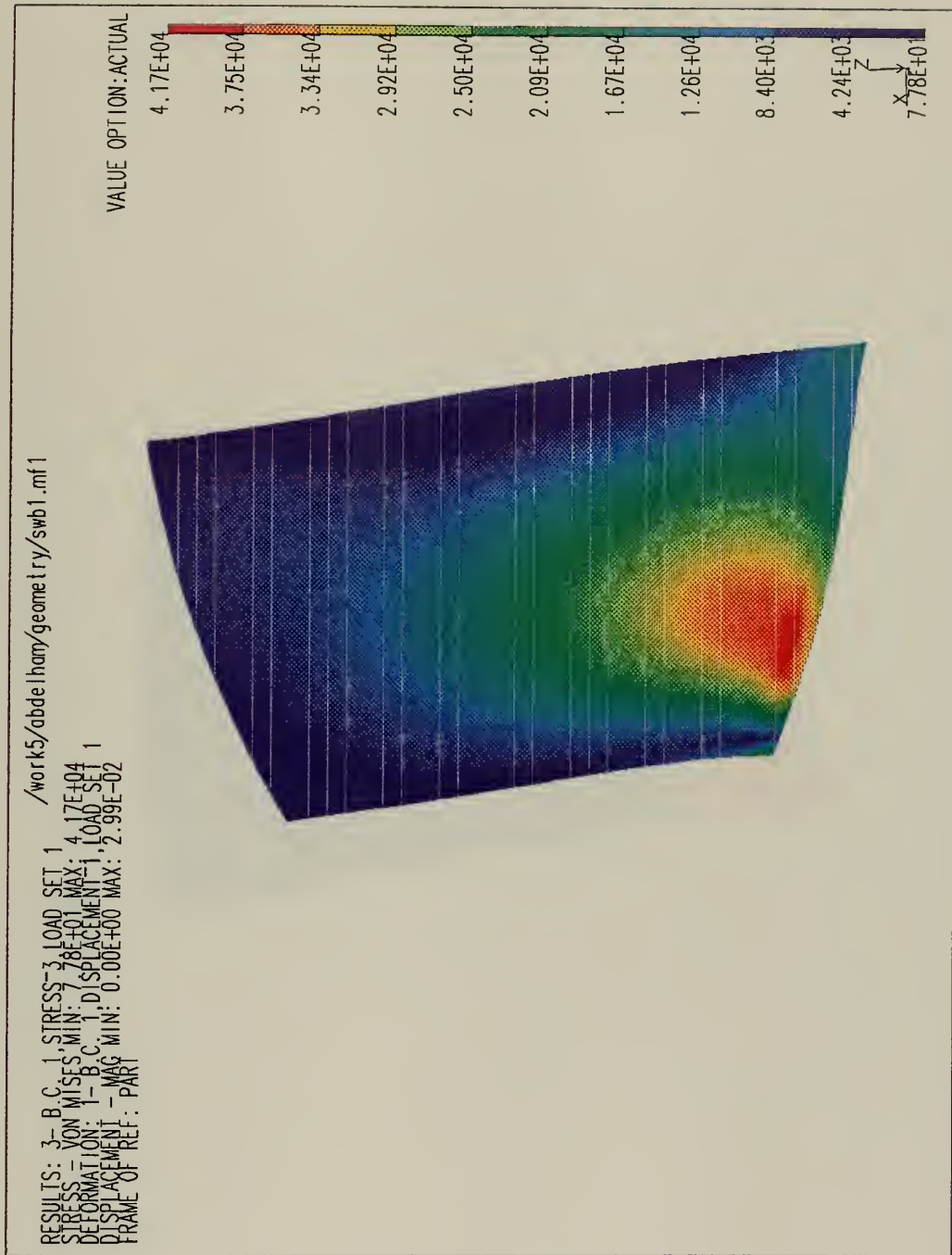


Figure 80. Stress Levels for the Swept-Backward Rotor.



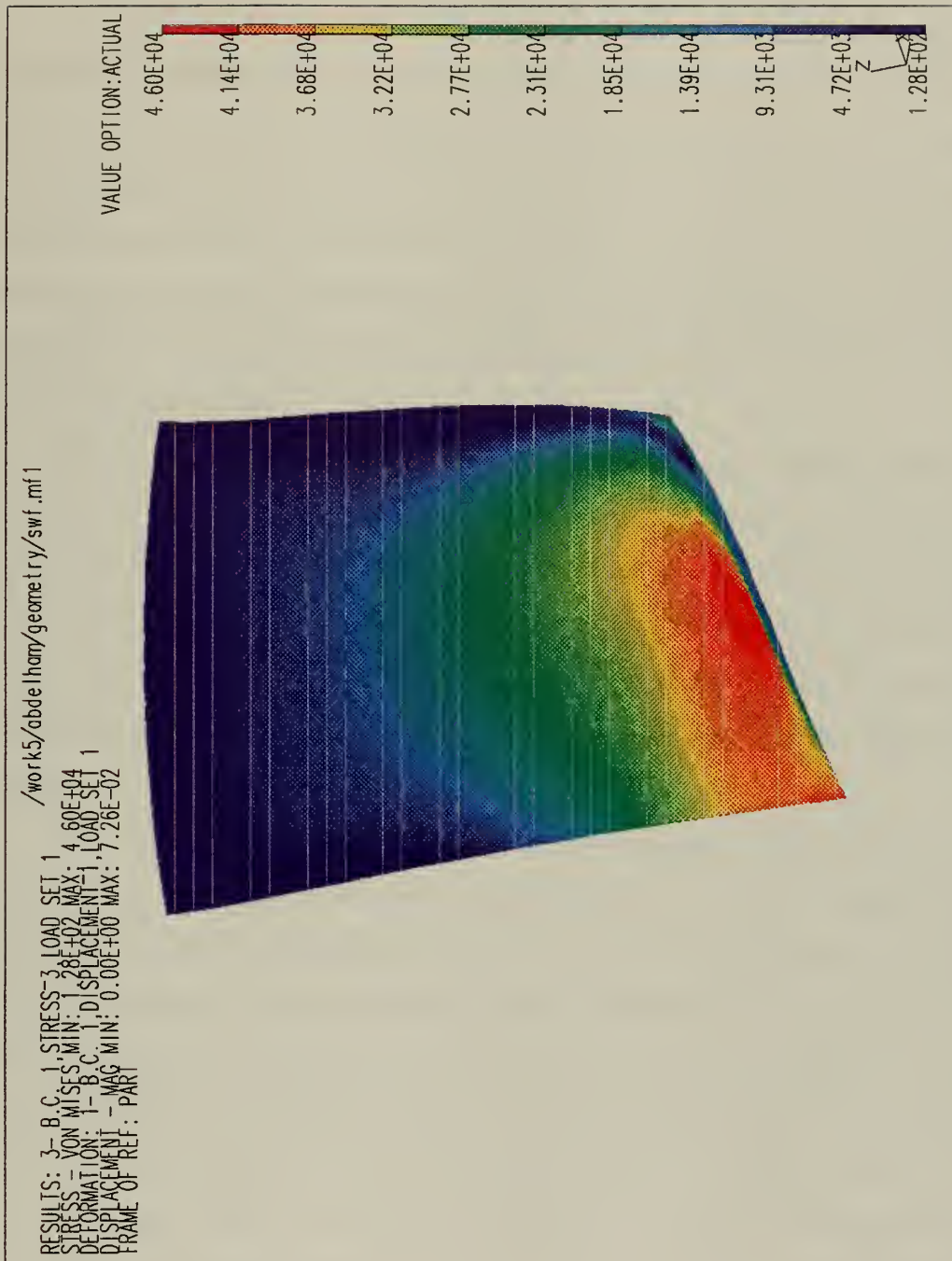


Figure 81. Stress Levels for the Swept-Forward Rotor.

THE UNIVERSITY OF CHICAGO



## VI. DISCUSSION

The 3D Bezier-surface geometry representation was successfully implemented to represent and manipulate an axial compressor blade geometry. The representation, since it depends on fewer parameters than traditional blade-element representations, limits the design space. However, it limits the space to acceptable geometries by not allowing manipulations that would result in radial waviness and to shapes that are inherently machinable. The fewer number of points required for blade representation simplifies the process of interfacing aerodynamic and structural analyses, and offers promise of optimization.

The application of the geometry representation to an existing geometry (the Sanger rotor) resulted in an improvement in performance. Although the improvement was small it was viewed in a positive way since one would expect a poorer performance with a blunter leading edge. The improvement might be due to several reasons, all of which are equally possible. It could be the minor change in shape introduced in the fitting process, or it could be the improved blade surface quality enforced by the package.

The swept cases revealed several important results related to sweep. It was shown that the swept-back rotor efficiency and mass flow rate were higher than the swept-forward rotor. The shock structure was seen to be weaker for the swept-back rotor while stronger for the swept-forward rotor. The results obtained were in agreement with the reported results in the open literature except for the effect of sweep on radial flow reported by Wadia et al [Ref. 13]. They reported that, in the back-swept rotor, there was significant radial flow in the boundary layer which weakens the flow at the tip section. In the present study the opposite was found. One thing to bear in mind is that the sweep schedules are very different and there could be effects other than sweep in Wadia et al's design to cause the difference. They also reported that the back sweep reduced the stall margin significantly and reasoned that this was due

to the boundary layer being centrifuged toward the tip section. In the work reported here an examination of stall margin was not conducted; but if the conclusion drawn by Wadia concerning the negative effect of centrifuged boundary layer flow is correct, we can cautiously expect an improvement in the stall margin using swept-back design because a reduction in that effect with backward sweep was observed here.

In spite of the trouble experienced with the leading edge grid generation it was very useful to show that the leading edge could have a dramatic effect on the blade row performance and flow structure. Figures 55 - 60 for Data Set 3 can be compared with the corresponding composite figures given in Appendix C for Data Set 2 to see the strong effect that the grid generation at the leading edge had on the predicted flow field. However, it is also interesting to note that the performance trends predicted to result from forward or backward sweep were the same for both data sets, and therefore are grid independent.

The difficulty with the grid generation arose because the Bezier representation was new, and the leading edge was a larger fraction of the blade chord. It is noted that the grid generation that was used was one that was developed for the Q3D design and analysis approach. It is possible that a grid generation process could be developed that would make use of the analytic properties of the Bezier representation to more optimally distribute and orient grid points.

A final comment concerns the enormous simplicity provided by the Bezier representation when going from aerodynamic analysis to stress analysis. The complete blade geometry (for the base rotor) is contained in the data in Table IV. (Compare this to the MERIDL format in Appendix A). Within IDEAS, the geometry can be manipulated and returned (through the geometry package program) to begin a new flow analysis cycle. There is a direct and exact interface between the aerodynamic and the structural analysis processes, which again points to the need to improve the coupling of the geometry package with grid generation for CFD.



## VII. CONCLUSIONS AND RECOMMENDATIONS

### A. CONCLUSIONS

From the presented study the following was concluded:

1. A 3D axial blade row geometry package was implemented successfully using a 3D Bezier surface representation.
2. The representation is highly flexible and allows manipulation easily and quickly.
3. When the package is fully-developed, MDDO (Multi-Disciplinary Design Optimization) is thought to be feasible due to the fewer number of control parameters, compatability with structural analysis and CAD/CAM programs, and the expected increase in computer speeds.
4. Sweep has a significant effect on aerodynamic performance, and the new geometry package will enable a more complete study to be conducted. The present results are not sufficient to draw general conclusions concerning the relative benefit of forward and backward sweep.
5. Leading-edge gridding has a significant effect on the computed performance and flow structure.
6. The package allows different leading-edge configurations to be examined more easily than is possible with current design systems.

### B. RECOMMENDATIONS

The following recommendations are made:

1. Calculations are required within the geometry package to derive parameters that are traditionally used by designers in current quasi-3D-based design processes.
2. A 3D grid generator which is fully compatible with the Bezier representation is required.
3. A technique to start a new design using the package should be developed.
4. A graphical user interface should be developed.

5. The process of optimization, involving aerodynamic performance, structural weight and manufacturing cost, should be examined.

# APPENDIX A. SANGER ROTOR GEOMETRY IN MERIDL3 FORMAT

MERIDL3 format is read into TCGRID as the number of points defining the hub and tip followed by the hub and tip coordinate points. Then the blade surface coordinates are read into TCGRID after reading in the number of radial sections on the blade, the number of points for each section and the number of blades. The sequence in which the points are read is,  $x$  coordinate for all data points followed by  $y$  coordinate then the  $z$  coordinate. The following is a listing of the Sanger-rotor blade definition in MERIDL3 format supplied to TCGRID.

32	14						
-.833	-.667	-.5833	-.50	-.4583	-.425	-.40833	-.3917
-.3333	-.25	-.16666	-.0833	0.0	.0833	.1	.1167
.125	.133	.14167	.15	.1583	.16666	.175	.183
.19166	.208	.25	.3333	.41666	.5	.667	.8333
.00083	.00083	.00083	.00083	.001667	.00625	.01083	.01667
.04467	.08937	.13405	.17873	.2234	.2681	.277	.286
.2904	.29333	.295583	.297667	.29933	.30033	.30166	.3025
.303333	.304166	.306083	.306083	.306083	.306083	.306083	.306083
-.8333	-.7637	-.666666	-.5	-.33333	-.2083	-.1239	-.04167
.0529	.2167	.3083	.5	.66666	.83333		
.4583	.4583	.4583	.4583	.4583	.4583	.4583	.4583
.4583	.4583	.4583	.4583	.4583	.4583		
11	23	22					
0.000000	0.000514	0.002301	0.005027	0.008746	0.013525	0.019448	
0.025568	0.031878	0.038395	0.045135	0.052088	0.059237	0.066568	
0.074067	0.081719	0.089506	0.097415	0.104086	0.109470	0.113531	
0.116248	0.116636						
0.001360	0.001751	0.003532	0.006238	0.009908	0.014595	0.020362	
0.026281	0.032350	0.038563	0.044956	0.051567	0.058387	0.065405	
0.072609	0.079987	0.087529	0.095222	0.101740	0.107019	0.111013	

0.113692	0.114041					
0.002013	0.002353	0.004135	0.006837	0.010492	0.015144	0.020848
0.026682	0.032644	0.038731	0.044945	0.051351	0.057968	0.064787
0.071798	0.078992	0.086358	0.093887	0.100278	0.105463	0.109392
0.112029	0.112356					
0.002617	0.002913	0.004692	0.007384	0.011017	0.015627	0.021259
0.027000	0.032848	0.038800	0.044857	0.051036	0.057417	0.064001
0.070780	0.077748	0.084894	0.092212	0.098434	0.103490	0.107325
0.109902	0.110207					
0.003875	0.004123	0.005878	0.008529	0.012096	0.016608	0.022099
0.027672	0.033327	0.039064	0.044881	0.050778	0.056765	0.062939
0.069314	0.075885	0.082643	0.089584	0.095503	0.100323	0.103986
0.106450	0.106724					
0.007383	0.007577	0.009239	0.011743	0.015099	0.019322	0.024430
0.029584	0.034782	0.040025	0.045312	0.050643	0.056018	0.061437
0.066995	0.072754	0.078711	0.084862	0.090132	0.094442	0.097727
0.099942	0.100171					
0.010925	0.011094	0.012640	0.014965	0.018075	0.021980	0.026692
0.031430	0.036196	0.040990	0.045811	0.050659	0.055534	0.060436
0.065366	0.070365	0.075575	0.081001	0.085687	0.089541	0.092492
0.094488	0.094690					
0.012591	0.012749	0.014226	0.016447	0.019417	0.023145	0.027641
0.032161	0.036707	0.041277	0.045871	0.050490	0.055133	0.059800
0.064492	0.069210	0.074074	0.079161	0.083566	0.087197	0.089983
0.091869	0.092059					
0.014092	0.014243	0.015665	0.017803	0.020663	0.024255	0.028587
0.032945	0.037327	0.041734	0.046166	0.050623	0.055105	0.059611
0.064143	0.068699	0.073344	0.078207	0.082428	0.085913	0.088589
0.090402	0.090584					
0.014068	0.014213	0.015624	0.017747	0.020588	0.024157	0.028465
0.032800	0.037163	0.041553	0.045971	0.050417	0.054890	0.059390
0.063918	0.068472	0.073071	0.077861	0.082024	0.085465	0.088111
0.089904	0.090081					
0.014718	0.014854	0.016226	0.018291	0.021057	0.024535	0.028737
0.032972	0.037239	0.041537	0.045868	0.050230	0.054624	0.059050
0.063508	0.067997	0.072518	0.077153	0.081192	0.084538	0.087114
0.088863	0.089032					
0.222890	0.223164	0.224119	0.225574	0.227560	0.230111	0.233273
0.236541	0.239910	0.243389	0.246988	0.250699	0.254516	0.258430
0.262434	0.266519	0.270677	0.274899	0.278461	0.281335	0.283503
0.284954	0.285162					



0.251549	0.251717	0.252483	0.253645	0.255222	0.257236	0.259714
0.262257	0.264864	0.267534	0.270281	0.273121	0.276052	0.279067
0.282162	0.285332	0.288573	0.291878	0.294678	0.296946	0.298663
0.299814	0.299964					
0.267527	0.267655	0.268328	0.269348	0.270728	0.272485	0.274639
0.276842	0.279093	0.281391	0.283738	0.286156	0.288655	0.291230
0.293877	0.296593	0.299375	0.302218	0.304631	0.306589	0.308072
0.309068	0.309192					
0.284586	0.284683	0.285263	0.286140	0.287324	0.288826	0.290661
0.292532	0.294438	0.296378	0.298351	0.300365	0.302444	0.304590
0.306799	0.309070	0.311399	0.313784	0.315811	0.317459	0.318709
0.319549	0.319648					
0.309498	0.309561	0.310012	0.310694	0.311611	0.312770	0.314181
0.315614	0.317067	0.318542	0.320037	0.321552	0.323091	0.324678
0.326317	0.328005	0.329743	0.331527	0.333048	0.334287	0.335228
0.335861	0.335932					
0.357485	0.357513	0.357749	0.358105	0.358582	0.359182	0.359909
0.360641	0.361380	0.362126	0.362877	0.363635	0.364399	0.365170
0.365960	0.366779	0.367626	0.368500	0.369249	0.369862	0.370329
0.370644	0.370677					
0.398682	0.398694	0.398800	0.398959	0.399173	0.399441	0.399764
0.400090	0.400417	0.400746	0.401077	0.401410	0.401744	0.402081
0.402419	0.402763	0.403120	0.403493	0.403815	0.404079	0.404282
0.404419	0.404433					
0.418757	0.418763	0.418826	0.418920	0.419046	0.419204	0.419394
0.419585	0.419778	0.419971	0.420166	0.420362	0.420558	0.420756
0.420955	0.421154	0.421360	0.421576	0.421762	0.421916	0.422034
0.422114	0.422122					
0.428363	0.428368	0.428414	0.428484	0.428578	0.428696	0.428837
0.428980	0.429124	0.429268	0.429413	0.429559	0.429706	0.429853
0.430002	0.430151	0.430303	0.430462	0.430600	0.430714	0.430802
0.430861	0.430867					
0.441651	0.441654	0.441683	0.441726	0.441784	0.441857	0.441945
0.442033	0.442122	0.442211	0.442301	0.442392	0.442483	0.442575
0.442667	0.442760	0.442854	0.442951	0.443036	0.443106	0.443160
0.443197	0.443201					
0.455686	0.455687	0.455696	0.455711	0.455730	0.455754	0.455783
0.455812	0.455841	0.455871	0.455901	0.455931	0.455961	0.455992
0.456023	0.456054	0.456085	0.456117	0.456145	0.456168	0.456186
0.456198	0.456199					
0.000000	0.003130	0.013824	0.029582	0.050062	0.074802	0.103219

0.130240	0.155860	0.179937	0.202284	0.222896	0.241772	0.258919
0.274350	0.288078	0.300126	0.310517	0.317930	0.323057	0.326440
0.328478	0.328755					
0.003128	0.005248	0.014776	0.028894	0.047394	0.069991	0.096331
0.121816	0.146442	0.170204	0.192927	0.214376	0.234537	0.253398
0.270953	0.287196	0.302128	0.315751	0.326106	0.333741	0.339090
0.342478	0.342908					
0.006040	0.007780	0.016799	0.030195	0.047807	0.069419	0.094760
0.119448	0.143479	0.166850	0.189543	0.211273	0.231916	0.251457
0.269884	0.287186	0.303358	0.318393	0.330054	0.338813	0.345050
0.349050	0.349537					
0.007812	0.009253	0.017833	0.030604	0.047445	0.068195	0.092652
0.116621	0.140101	0.163087	0.185579	0.207502	0.228555	0.248690
0.267892	0.286148	0.303448	0.319781	0.332650	0.342455	0.349523
0.354099	0.354630					
0.009343	0.010493	0.018600	0.030696	0.046703	0.066514	0.089999
0.113166	0.136014	0.158540	0.180744	0.202624	0.224143	0.245014
0.265160	0.284567	0.303219	0.321104	0.335414	0.346469	0.354528
0.359790	0.360368					
0.012457	0.013335	0.020849	0.032095	0.047041	0.065645	0.087855
0.109937	0.131892	0.153720	0.175419	0.196989	0.218430	0.239739
0.260729	0.281254	0.301299	0.320851	0.336758	0.349226	0.358424
0.364482	0.365102					
0.015765	0.016553	0.023727	0.034476	0.048786	0.066639	0.088013
0.109331	0.130593	0.151800	0.172950	0.194043	0.215080	0.236060
0.256983	0.277785	0.298246	0.318337	0.334786	0.347746	0.357349
0.363693	0.364329					
0.017368	0.018125	0.025166	0.035718	0.049774	0.067318	0.088335
0.109313	0.130251	0.151148	0.172006	0.192823	0.213600	0.234336
0.255031	0.275683	0.296131	0.316262	0.332787	0.345836	0.355522
0.361930	0.362568					
0.017681	0.018424	0.025428	0.035926	0.049911	0.067370	0.088289
0.109172	0.130021	0.150833	0.171610	0.192351	0.213056	0.233725
0.254357	0.274953	0.295433	0.315629	0.332229	0.345354	0.355104
0.361559	0.362199					
0.020481	0.021191	0.028075	0.038395	0.052140	0.069302	0.089865
0.110394	0.130889	0.151350	0.171776	0.192168	0.212524	0.232846
0.253132	0.273383	0.293579	0.313542	0.329959	0.342944	0.352593
0.358983	0.359607					
0.022265	0.022938	0.029745	0.039948	0.053539	0.070507	0.090839
0.111137	0.131402	0.151632	0.171829	0.191991	0.212119	0.232212
0.252270	0.272292	0.292279	0.312138	0.328482	0.341417	0.351034



0.357405 0.358014

0.012140	0.013271	0.015723	0.020605	0.026613	0.033270	0.040423
0.046930	0.052625	0.056725	0.058821	0.058171	0.055174	0.050923
0.045640	0.039421	0.032344	0.024471	0.017334	0.011261	0.006500
0.003227	0.002754					
0.008415	0.009086	0.011001	0.015115	0.020300	0.026140	0.032514
0.038449	0.043927	0.048565	0.051401	0.052210	0.050709	0.047455
0.043005	0.037468	0.030935	0.023484	0.016620	0.010724	0.006074
0.002868	0.002444					
0.006996	0.007507	0.009179	0.012944	0.017738	0.023178	0.029159
0.034788	0.040080	0.044786	0.048184	0.049451	0.048574	0.045817
0.041758	0.036547	0.030278	0.023035	0.016306	0.010494	0.005897
0.002722	0.002323					
0.005881	0.006264	0.007690	0.011089	0.015470	0.020478	0.026017
0.031279	0.036310	0.040932	0.044751	0.046737	0.046556	0.044468
0.040876	0.036021	0.030002	0.022910	0.016238	0.010429	0.005811
0.002612	0.002229					
0.004812	0.005074	0.006210	0.009149	0.013000	0.017449	0.022407
0.027160	0.031787	0.036186	0.040080	0.043052	0.044156	0.043004
0.040114	0.035758	0.030056	0.023107	0.016429	0.010538	0.005816
0.002528	0.002158					
0.003883	0.004038	0.004859	0.007093	0.010122	0.013734	0.017867
0.021901	0.025897	0.029809	0.033485	0.036674	0.039040	0.039943
0.038515	0.035235	0.030241	0.023646	0.016996	0.010959	0.006030
0.002559	0.002193					
0.003711	0.003821	0.004584	0.006259	0.008616	0.011596	0.015185
0.018781	0.022355	0.025837	0.029117	0.032043	0.034427	0.036053
0.036581	0.034767	0.030549	0.024341	0.017731	0.011542	0.006395
0.002729	0.002349					
0.003711	0.003803	0.004605	0.006016	0.008040	0.010721	0.014083
0.017523	0.020946	0.024251	0.027322	0.030037	0.032265	0.033869
0.034707	0.033940	0.030501	0.024674	0.018166	0.011918	0.006638
0.002844	0.002453					
0.003764	0.003847	0.004695	0.006003	0.007894	0.010468	0.013774
0.017194	0.020602	0.023871	0.026880	0.029512	0.031656	0.033208
0.034068	0.033707	0.030752	0.025080	0.018572	0.012234	0.006836
0.002934	0.002534					
0.003647	0.003714	0.004599	0.005710	0.007335	0.009645	0.012724
0.015971	0.019214	0.022300	0.025098	0.027502	0.029426	0.030807
0.031601	0.031609	0.029519	0.024393	0.018209	0.012062	0.006763
0.002905	0.002513					

0.003567	0.003619	0.004576	0.005519	0.006910	0.009001	0.011916
0.015057	0.018207	0.021177	0.023823	0.026041	0.027763	0.028960
0.029632	0.029767	0.028414	0.024014	0.018085	0.012047	0.006772
0.002905	0.002519					

# APPENDIX B. GENERATING IGES FILES

Initial Graphics Exchange Specification (IGES) [Ref. 24] is the standard for defining geometric objects to ensure importability and system independence. The IGES files that are written according to the standard can be read by CAD programs, finite element programs, and CNC machines programs.

## 1. IGES FILE STRUCTURE

IGES files have a fixed 80-column ASCII file format. Columns 1-72 include the data while columns 73-80 represent the sequence field that numbers the lines contained in each of the different sections. The file consists of five sections to define the geometry. Each geometry element is considered as a separate entity that has to be assigned a pre-defined entity number. The five sections are start, global, directory entry, parameter data and terminate.

### a. Start Section

Start section may contain text in columns 1-72 and a letter 'S' in column 73. One at least is required even if empty, except for the sequence field.

### b. Global Section

This section contains information describing the program that generated the file, and information needed by the reading program. The records are identified with the letter 'G' in column 73 and sequenced in column 74-80. The parameters in the global section include system ID, precision magnitude, precision significance, scale, units, time stamp and version, among others.

### c. Directory Section

Each entity in the file should have one directory record in the directory entity section. Each record is 20 fields of fixed length. Each field is eight characters and the field is written on two lines. The records are identified by the letter 'D'.

#### **d. Parameter Data Section**

This section defines the entities to be drawn according to the definition given in the IGES standard. Each geometric object (line, circle, etc.) is assigned an "entity number" which is followed by a list of numbers separated by commas. The definition for the geometric entity can take as many lines as necessary to have a complete representation. The records are identified by the letter 'P'.

#### **e. Terminate Section**

Terminate section is the last line in the file and is always one line. It has 10 fields of fixed length of eight characters. The fields contain the total number of lines of each section. The total number of lines in each of the start section, global section, directory entry section and parameter data section are written in the first, second, third and fourth fields respectively. The record is identified by the letter 'T'.

### **2. GEOMETRY IN IGES FORMAT**

The natural B-spline surface entity (128) is used to represent the blade surfaces. Since the Bezier surfaces are a special case of the B-spline surfaces, the blade surfaces are fully represented by this entity. The full blade is represented by six B-Spline surface (128) entities [Ref. 24].

## APPENDIX C. RESULTS OF FLOW ANALYSIS WITH DIFFERENT GRIDS

The following results are from Data Set 2.

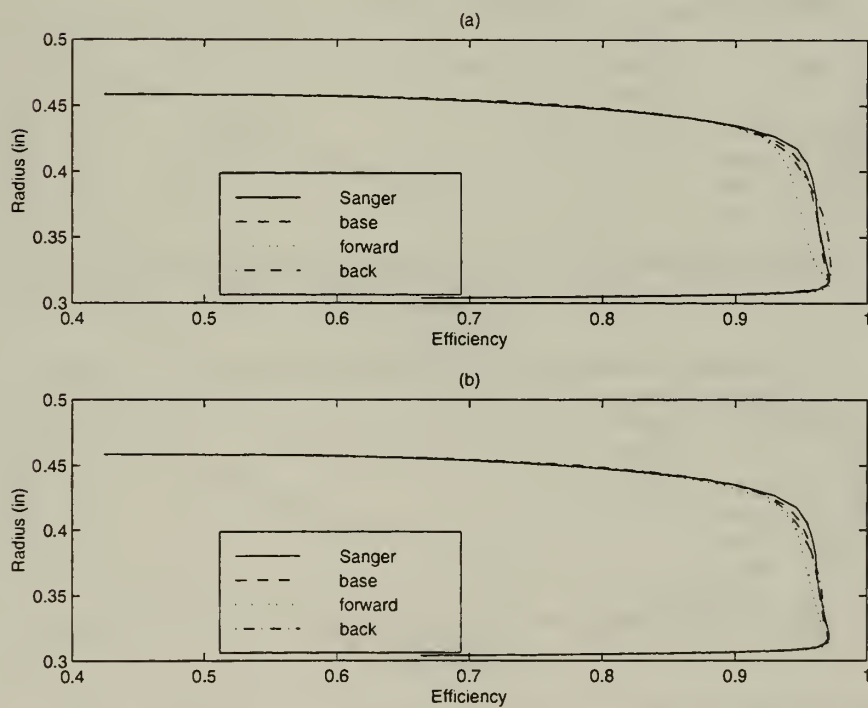


Figure 82. Radial Distribution of the Circumferentially Energy-Averaged Efficiency.

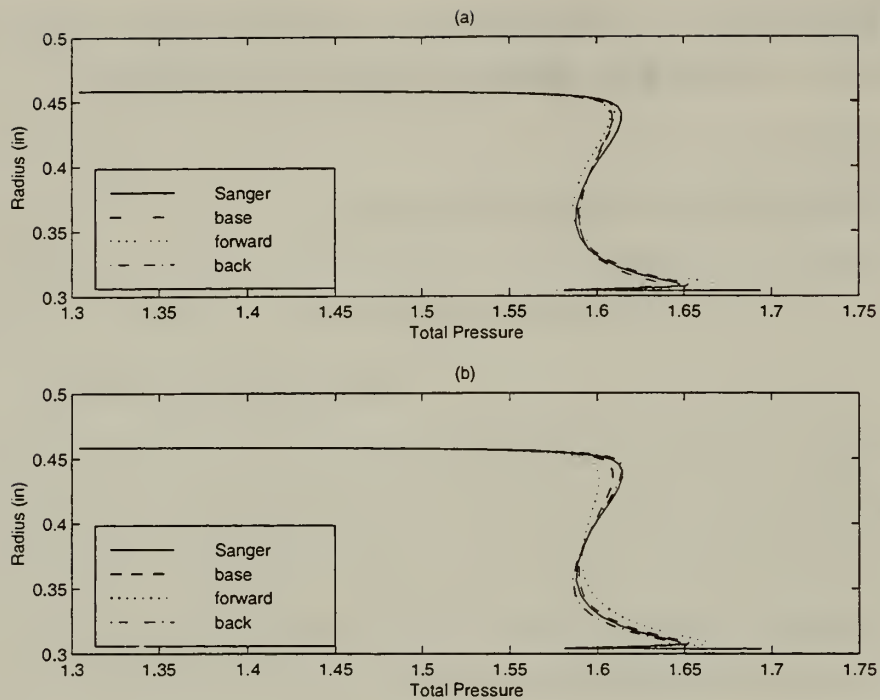


Figure 83. Radial Distribution of the Circumferentially Energy-Averaged Total-to-Reference Pressure.

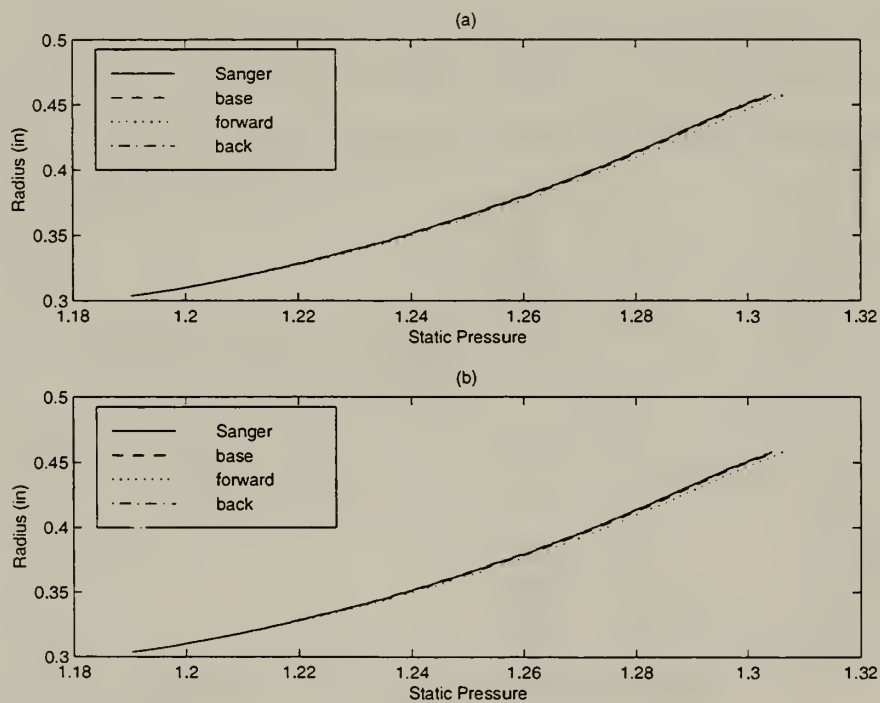


Figure 84. Radial Distribution of the Circumferentially Energy-Averaged Static-to-Reference Pressure.



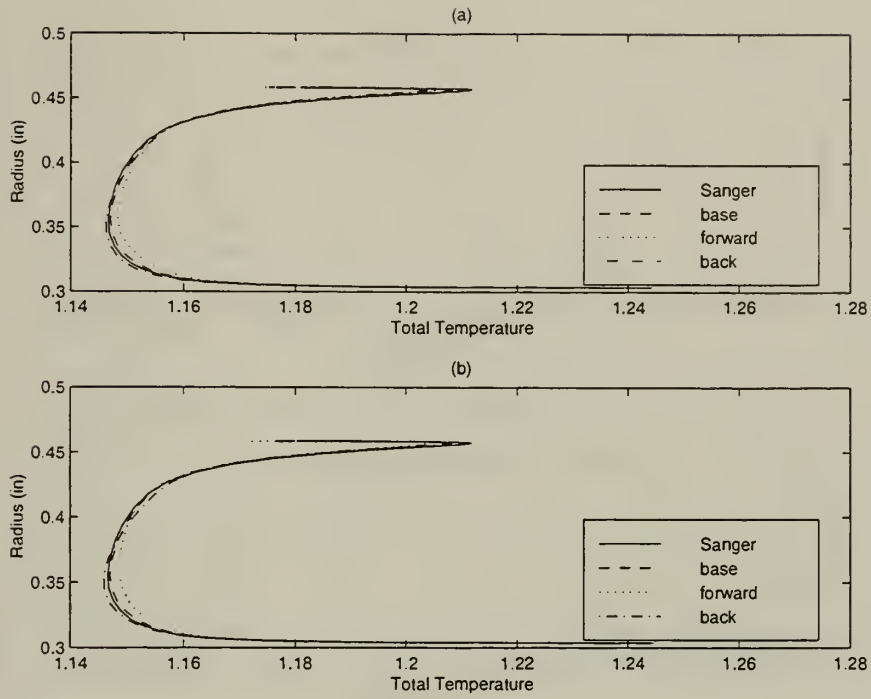


Figure 85. Radial Distribution of the Circumferentially Energy-Averaged Total-to-Reference Temperature.

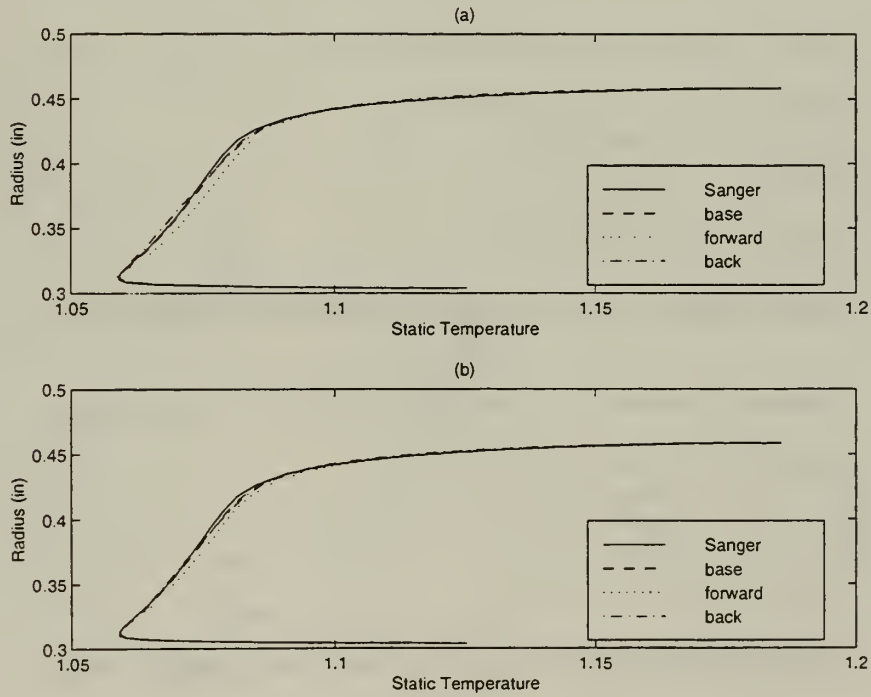


Figure 86. Radial Distribution of the Circumferentially Energy-Averaged Static-to-Reference Temperature.

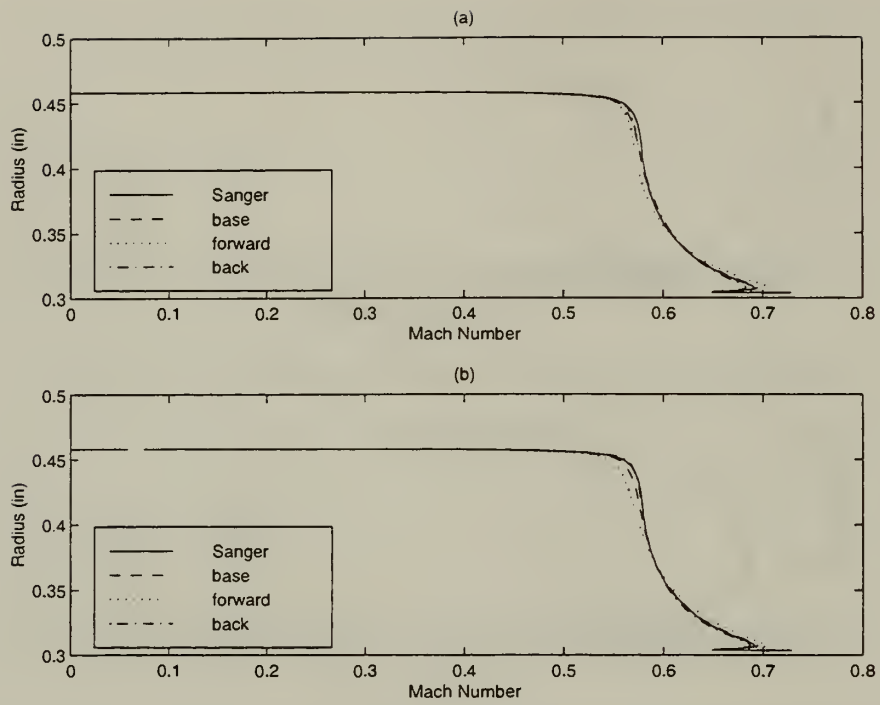


Figure 87. Radial Distribution of the Mach Number.

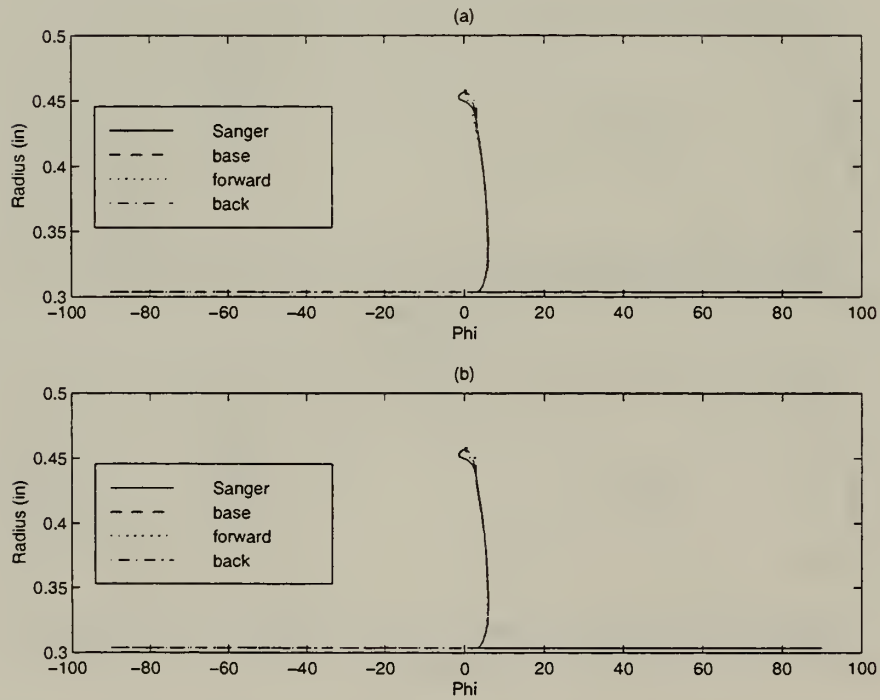


Figure 88. Radial Distribution of the Flow Angle ( $\phi$ ) in the Meridional Plane.

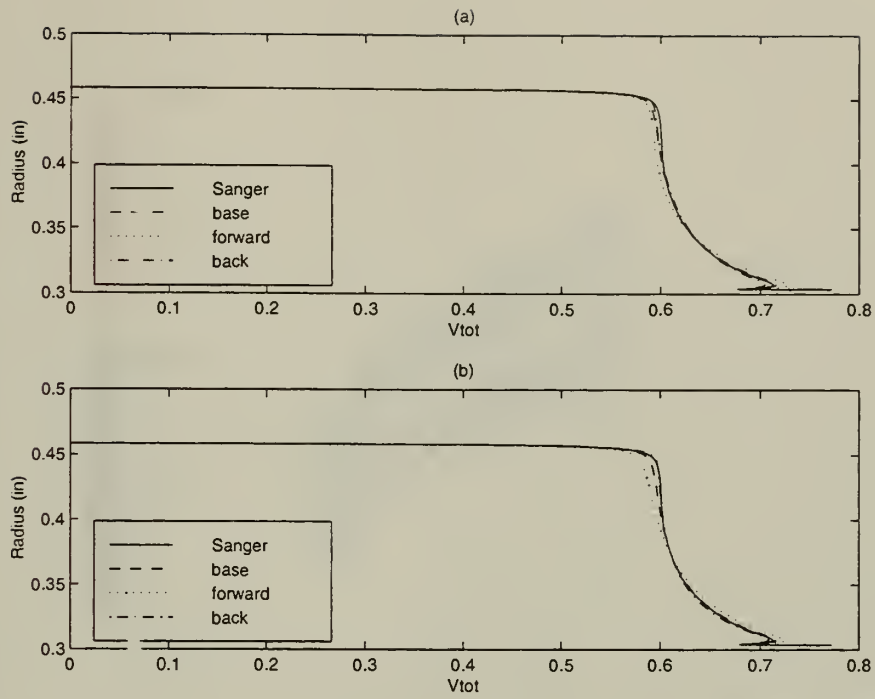


Figure 89. Radial Distribution of the Total Velocity to Reference Sonic Velocity.

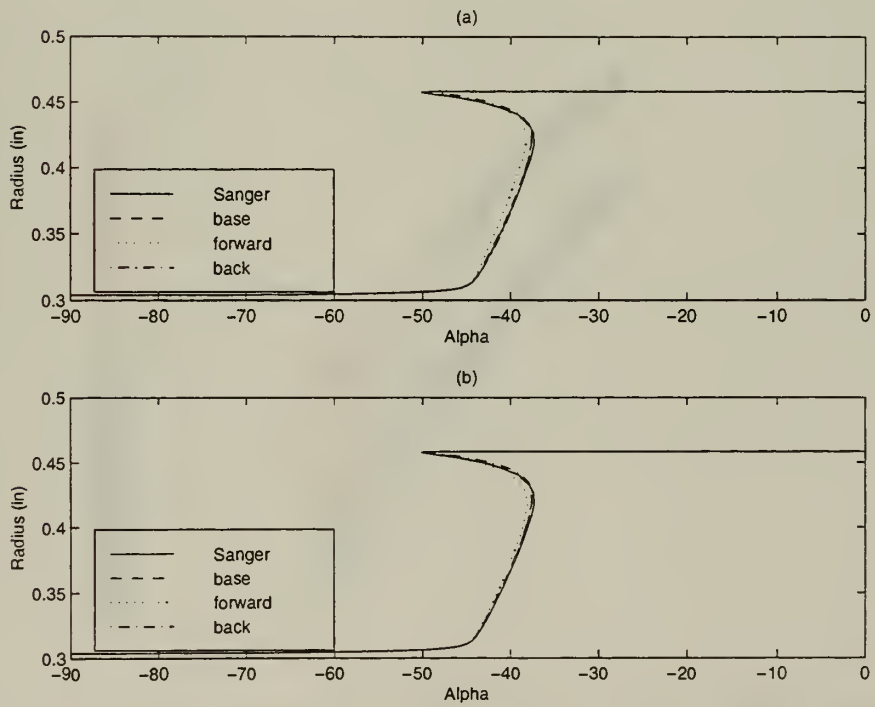


Figure 90. Radial Distribution of the Swirl Angle ( $\alpha$ ).



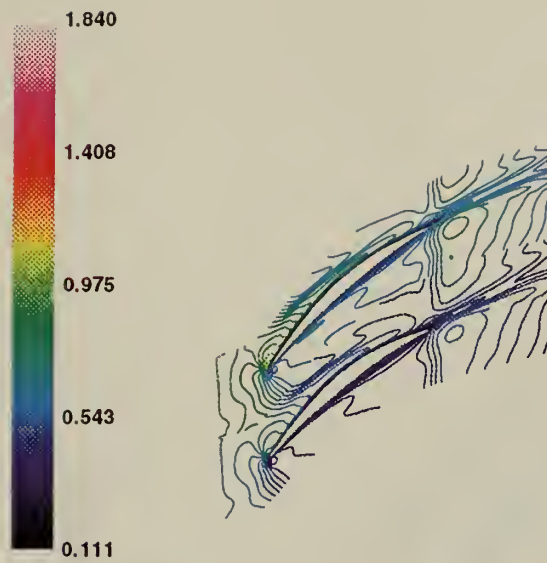


Figure 91. Mach Number in the Blade Passage of the Sanger Rotor (Lower Blade) and Base Rotor

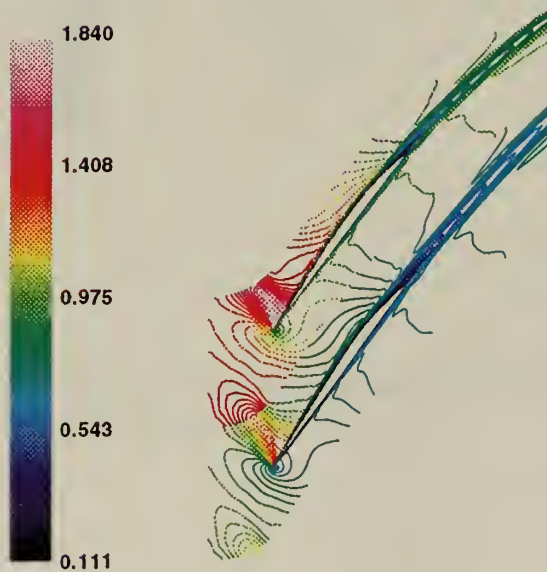


Figure 92. Mach Number in the Blade Passage of the Sanger Rotor (Lower Blade) and Base Rotor (Upper Blade) at 50% Span.





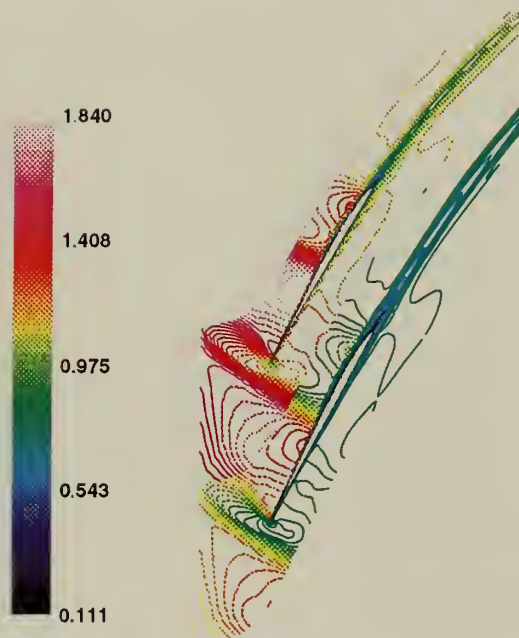


Figure 93. Mach Number in the Blade Passage of the Sanger Rotor (Lower Blade) and Base Rotor (Upper Blade) at 75% Span.



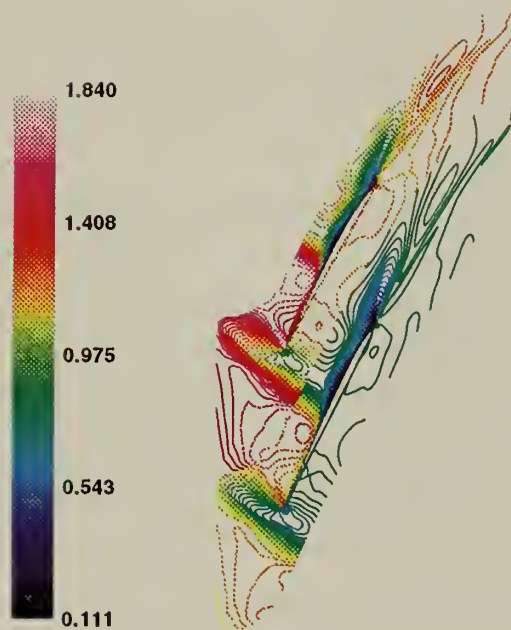


Figure 94. Mach Number in the Blade Passage of the Sanger Rotor (Lower Blade) and Base Rotor (Upper Blade) in the Case Wall Boundary Layer.



# LIST OF REFERENCES

- [1] C. H. Wu. *A General Theory of Three-Dimensional Flow In Subsonic and Supersonic Turbomachines of Axial-, Radial- and Mixed-Flow Types*. NACA TN 2604, 1952.
- [2] C. H. Wu, Z. Wang, and H. Chen. Three-dimensional rotational flow in transonic turbomachines: Part I - solution obtained using a number of  $S_1$  stream filaments of revolution and a central  $S_2$  stream filament. *Journal of Turbomachinery*, 14:38–49, 1992.
- [3] C. H. Wu, X. Zhao, and L. Qin. Three-dimensional rotational flow in transonic turbomachines: Part II - full three-dimensional flow in cas rotor obtained by using a number of  $S_1$  and  $S_2$  stream filaments. *Journal of Turbomachinery*, 14:50–60, 1992.
- [4] J. D. Denton. Designing in three dimensions. *AGARD Lecture Series 195*, pages 3.1 – 3.14, May 1994.
- [5] I. K. Jennions and P. Stow. A quasi-three-dimensional turbomachinery blade design system: Part I - throughflow analysis. *Journal of Engineering for Gas Turbines and Power*, 107:301–307, 1985.
- [6] I. K. Jennions and P. Stow. A quasi-three-dimensional turbomachinery blade design system: Part II - computerized system. *Journal of Engineering for Gas Turbine and Power*, 107:308–316, 1985.
- [7] N. L. Sanger. Design of a low aspect ratio transonic compressor stage using cfd techniques. *Journal of Turbomachinery*, pages 479–491, July 1996.
- [8] G. R. Miller, G. W. Lewis, and M. J. Hartmann. Shock losses in transonic compressor blade row. *Journal of Engineering for Power*, pages 235–242, 1962.
- [9] A. J. Wennerstrom and S.L. Puterbaugh. A three dimensional model for the prediction of shock losses in compressor blade rows. *Journal of Engineering for Gas Turbines and Power*, 106:552–560.
- [10] R.J. Neubert, D. E. Hobbs, and H. D. Weingold. Application of sweep to improve the efficiency of a transonic fan : Part I - design. *Journal of Propulsion and Power*, 11(1):49–576, 1995.
- [11] S. L. Puterbaugh, W. W. Copenhaver, C. Hah, and A. J. Wennerstrom. A three-dimensional shock loss model applied to an aft-swept, transonic compressor rotor.

- [12] C. H. Law and A. R. Wadia. Low aspect ratio transonic rotors: Part I - baseline design and performance. *Journal of Turbomachinery*, 115:218–225, 1993.
- [13] A. R. Wadia, P. N. Szucs, and D. W. Crall. Inner working of aerodynamic sweep. *ASME 97-GT-401, Presented at the International Gas Turbine and Aeroengine congress & Exhibition, Orlando, Florida, June 2 - 5, 1997.*
- [14] A. R. Wadia, P. N. Szucs, P. N. Niskode, and P. M. Battle. Forward swept rotor blade. *US Patent Number 5,167,489.*
- [15] J. D. Foley, A. Van Dam, S. K. Feiner, and J. F. Hughes. *Computer Graphics Principles and Practice Second Edition.* Addison-Wesley Publishing Company, 1990.
- [16] G. Farin. *Curves and Surfaces for Computer Aided Geometric Design A Practical Guide.* Academic Press, 1993.
- [17] J. Hoschek. Intrinsic parametrization for approximation. *Computer Aided Geometric Design*, pages 27–31, 1988.
- [18] R. V. Chima. Rvc3d - rotor viscous code 3-d. *User's Manual and Documentation Version 920318, NASA Lewis Research Center, Cleveland, Ohio, March, 1992.*
- [19] H. F. Abdelhamid. Three dimensial geometry package for axial compressor blading-initial code listing. *Technal Report NPS-AA-97-001, Naval Postgraduate School, Monterey California, September, 1997.*
- [20] R. V. Chima. Tcgrid. *User's Manual , NASA Lewis Research Center, Cleveland, Ohio, November, 1990.*
- [21] R.V. Chima. Viscous three-dimensional calculations of transonic fan performance. *Technical Memorandum, NASA TM-103800, 1991.*
- [22] R.V. Chima and J. W. Yokota. Numerical analysis of three- dimensional viscous flows in turbomachinery. 28(5):798 – 806, May 1990.
- [23] W. D. Reid. Transonic axial compressor design case study and preparation for testing. *Master Thesis, Naval Postgraduate School, Monterey California, September, 1995.*
- [24] *Initial Graphics Exchange Specification IGES 5.3.* 1996.



# INITIAL DISTRIBUTION LIST

1. Defense Technical Information Center ..... 2  
8725 John J. Kingman Road., Ste 0944  
Ft. Belvoir, VA 22060-6218
2. Dudley Knox Library ..... 2  
Naval Postgraduate School  
411 Dyer Rd.  
Monterey, CA 93943-5101
3. Chairman, Department of Aeronautics and Astronautics Code AA ..... 1  
Naval Postgraduate School  
699 Dyer RD - Room 137  
Monterey, California 93943-5106
4. Professor R. P. Shreeve Code AA/SF ..... 5  
Naval Postgraduate School  
699 Dyer RD - Room 137  
Monterey, California 93943-5106
5. Assoc. Professor G.V. Hobson, Code AA/HG ..... 1  
Naval Postgraduate School  
699 Dyer RD - Room 137  
Monterey, California 93943-5106
6. Dist. Professor Max. F. Platzler, Code AA/PL ..... 1  
Naval Postgraduate School  
699 Dyer RD - Room 137  
Monterey, California 93943-5106
7. Assoc. Professor David Canright, Code MA/CA ..... 1  
Naval Postgraduate School  
Monterey, California 93943-5106
8. Assoc. Professor Joshua Gordis, Code ME/GO ..... 1  
Naval Postgraduate School  
Monterey, California 93943-5106
9. Armament Authority, Training Dept. (Egypt) ..... 3  
c/o American Embassy (Cairo Egypt),  
Office of Military Cooperation,  
Box 29 (TNG)  
FPO, NY 09527-0051

10. ATTN:J. Zidzik. Code 4.4.7.1, BLDG 106 ..... 1  
 Naval Air Warfare Center - Aircraft Division  
 Propulsion and Power Engineering  
 22195 Elmer RD, Unit 4  
 Patuxent River, Maryland 20670-1534
  
11. ATTN:S. MacAdams, Code 4.4.7.1, BLDG 106 ..... 1  
 Naval Air Warfare Center - Aircraft Division  
 Propulsion and Power Engineering  
 22195 Elmer RD, Unit 4  
 Patuxent River, Maryland 20670-1534
  
12. ATTN:C. Gorton, Code 4.4T, BLDG 106 ..... 1  
 Naval Air Warfare Center - Aircraft Division  
 Propulsion and Power Engineering  
 22195 Elmer RD, Unit 4  
 Patuxent River, Maryland 20670-1534
  
13. Mr. Nelson Sanger.....1  
 752 Elmwood RD  
 Rocky River, Ohio 44116
  
14. ATTN:R. V. Chima, MS 77-61 .....1  
 NASA Lewis Research Center  
 21000 Brookpark RD  
 Cleveland, Ohio 44135
  
15. ATTN:Chunill Hah, MS 5-11.....1  
 NASA Lewis Research Center  
 21000 Brookpark RD  
 Cleveland, Ohio 44135
  
16. Hazem Fahmy Abdelhamid ..... 2  
 15B El Tebr St.  
 Hammamat El Koba  
 Ciaro, Egypt.



DUDLEY KNOX LIBRARY



3 2768 00341260 2